

University of Alberta

**Nanoscale Resonators Fabricated from
Metallic Alloys, and Modeling and Simulation
of Polycrystalline Thin Film Growth**

by

Colin Ophus

A thesis submitted to the Faculty of Graduate Studies and Research
in partial fulfillment of the requirements for the degree of

Doctor of Philosophy

Department of Chemical and Materials Engineering

© Colin Ophus
Spring 2010
Edmonton, Alberta

Permission is hereby granted to the University of Alberta Libraries to reproduce single copies of this thesis and to lend or sell such copies for private, scholarly or scientific research purposes only. Where the thesis is converted to, or otherwise made available in digital form, the University of Alberta will advise potential users of the thesis of these terms.

The author reserves all other publication and other rights in association with the copyright in the thesis and, except as herein before provided, neither the thesis nor any substantial portion thereof may be printed or otherwise reproduced in any material form whatsoever without the author's prior written permission.

Examining Committee

David Mitlin, Chemical and Materials Engineering

Michael Brett, Electrical and Computer Engineering

Ken Cadien, Chemical and Materials Engineering

John Nychka, Chemical and Materials Engineering

Hao Zhang, Chemical and Materials Engineering

Michael Eikerling, Physics, Simon Fraser University

Many are content with their current knowledge;
This thesis is for those who choose to discover more.

Abstract

We have designed a binary metallic alloy for nanoscale resonator applications. Magnetron sputtering was used to deposit films with different stoichiometries of aluminum and molybdenum and then characterized the microstructure and physical properties of each film. A structure zone map is proposed to describe the dependence of surface and bulk structure on composition. We then fabricated proof of principle resonators from the Al-32 at.%Mo composition, selected for its optimized physical properties. An optical interferometer was used to characterize the frequency response of our resonators.

In the second half of this thesis we investigate the growth of faceted polycrystalline thin films with modeling and simulations. A new analytic model is derived for the case of orientation dependent facet growth velocity and the dependence of growth on initial grain orientations is explicitly calculated. Level set simulations were used to both confirm this analytic model and extend it to include various angular flux distributions, corresponding to different deposition methods. From these simulations, the effects of self-shadowing on polycrystalline film growth are quantitatively evaluated.

Preface

The overarching topic of this thesis is thin film material science. This work encompasses aspects of alloy design, fabrication and characterization of thin films, as well as simulation and modeling of polycrystalline thin film growth. Chapter 1 provides an overview of thin film technologies and their importance in science and engineering, and also introduces methods of thin film deposition, characterization and growth simulation. Chapter 2 describes the design of a thin film Al-Mo alloy for a specific application: metal nanoscale resonators. The fabrication and testing of these resonators is described in Chapter 3. In Chapter 4, I derive a polycrystalline thin film growth model. Chapters 5 and 6 present the results of two types of polycrystalline thin film growth simulation. Finally, Chapter 7 summarizes the work contained in this thesis and suggests future directions to extend the experiments and simulation. This thesis follows a traditional format; however Chapters 2 to 6 are based on one or more of our peer-reviewed papers. Links to these papers are provided on each chapter title page.

Acknowledgements

None of the work in my thesis could have been accomplished without the help of others. First, I would like to thank my supervisor, David Mitlin, for giving me the latitude to pursue what I was interested in, the resources I required, and the perspective of a materials scientist. I am eternally grateful for the countless times I was helped by my group; Thank you Jian Chen, Mohsen Danaie, Julian Haagsma, Chris Harrower, Chris Holt, Peter Kalisvaart, Reza Mohammadi, Brian Olsen, Kyle Sand, Babak Shalchi-Amirkhiz, Xuehai Tan and Benjamin Zahiri. In particular I want to thank Erik Lubber for teaching me that there are no bounds on the science we can learn, and the importance of rigorous discussion of our ideas.

I thank Andrew Murray, Nathan Nelson-Fitzpatrick and Lee Fischer for being great collaborators and friends. Thank you to Nemanja Danilovic for convincing me to switch into the PhD program and Timo Ewalds for showing me what a true programmer is capable of. I would also like to thank Steve Buswell, Nick Glass and Michael Brett for making my stay in the Department of Electrical and Computer Engineering much more enjoyable. I learned a lot from my colleagues at the National Center for Electron Microscopy and the Canadian Neutron Beam Centre, especially Velimir “Mimo” Radmilovic and Helmut Fritzsche. Thank you to Holly Barton for proofing much of my work and Stephanie Jonsson for reminding me of the importance of artwork and design. I also thank all of my other friends for their unerring support. Lastly, I would like to thank my family: my brother Philip for being so smart, my sister Emily for being uncompromising and my parents Elaine and Duane for giving me everything.

Contents

1	Introduction to Thin Films	1
1.1	Thin Film Technology and Materials Science	1
1.2	Structure	2
1.2.1	Single Crystal	3
1.2.2	Polycrystalline	4
1.2.3	Amorphous	5
1.2.4	Nanocrystalline	6
1.3	Deposition Techniques	6
1.3.1	Evaporation	7
1.3.2	Pulsed Laser Deposition	8
1.3.3	Sputtering	8
1.3.4	Reactive Physical Vapour Deposition	10
1.3.5	Chemical Vapour Deposition	11

CONTENTS

1.4	Characterization Techniques	12
1.4.1	X-ray Diffraction	12
1.4.2	Transmission Electron Microscopy	13
1.4.3	Scanning Electron Microscopy	14
1.4.4	Energy-Dispersive X-ray Spectroscopy	14
1.4.5	Atomic Force Microscopy	15
1.4.6	Nanoindentation	15
1.4.7	Four Point Probe	16
1.5	Simulation Techniques	16
1.5.1	Level Set Simulations	17
2	Al-Mo Alloy Design for Thin Film Applications	19
2.1	Motivation	19
2.2	Background	21
2.2.1	Aluminum–Molybdenum	21
2.2.2	Deposition and Stoichiometries	24
2.3	Results and Discussion	27
2.3.1	Microstructure	27
2.3.2	Film Surface	30
2.3.3	Physical Properties	34
2.4	Summary	38

CONTENTS

3	Metallic Nanoscale Resonators	39
3.1	Motivation	39
3.2	Experimental Methods	41
3.2.1	Resonator Fabrication	41
3.2.2	Cantilever Frequency Response	43
3.2.3	Optical Frequency Characterization	46
3.3	Results and Discussion	47
3.3.1	Frequency Measurements	47
3.4	Summary	49
4	Polycrystalline Film Growth Model	51
4.1	Motivation	51
4.2	Analytic Growth Model	53
4.2.1	Initial angular distributions	53
4.2.2	Model Derivation	54
4.3	Model Validation	58
4.3.1	2+1D Simulation of Conic Grains	58
4.3.2	Comparison of Model to Simulation	59
4.4	Analysis of Grain Growth Model	61
4.4.1	Self-Similarity of Distributions	61
4.4.2	Scaling Laws	62

CONTENTS

4.4.3	The Effect of Non-Uniform Initial Distributions	63
4.5	Summary	64
5	Polycrystalline Film Growth Simulations	66
5.1	Motivation	66
5.2	Background	68
5.2.1	The van der Drift Model	68
5.2.2	Level Set Simulation	70
5.3	Analysis of Late-Stage Growth	71
5.3.1	Geometry	71
5.3.2	Statistical Measures	72
5.4	Simulated Kinetic Wulff Shapes	74
5.4.1	Tetrahedron	74
5.4.2	Great Rhombicuboctahedron	75
5.4.3	Diamond System	75
5.5	Results and Discussion	76
5.5.1	Surface Morphology and Texture	76
5.5.2	Growth Statistics	79
5.5.3	Mean Grain Diameter Fit	81
5.5.4	Growth Statistics for Varying Wulff Geometries	82
5.5.5	Model Limitations and Generalizations	84

CONTENTS

5.6	Summary	86
6	Self-Shadowing in Polycrystalline Film Growth	87
6.1	Motivation	87
6.2	Faceted Polycrystalline Thin Films	89
6.3	Simulation Methodology	91
6.3.1	van der Drift Model	91
6.3.2	Initial conditions and grain morphology	92
6.3.3	Ballistic mass deposition and surface evolution	93
6.3.4	Diffusion	95
6.3.5	Statistical measurements	95
6.4	Results and discussion	96
6.4.1	Surface morphology and texture	96
6.4.2	Cross sections	99
6.4.3	Growth statistics	99
6.4.4	Dependence of scaling laws on self-shadowing	104
6.4.5	Model Limitations and Applicability	109
6.5	Summary	110
7	Conclusions	112
7.1	Thesis Summary	112

CONTENTS

7.1.1	Part I	112
7.1.2	Part II	114
7.2	Future Work	115
7.2.1	Part I	115
7.2.2	Part II	115
A	Statistical Derivations	117
A.1	Initial Texture Distributions	117
A.2	Thin Film Statistical Relationships	119
	References	122

List of Figures

1.1	Heightmaps of different thin film types: (A) Single crystal gold surface fabricated by Lüssem et al. (B) Polycrystalline nickel surface. (C) Amorphous Al-32 at.%Mo surface.	3
1.2	2D atomistic view of the possible microstructures of a solid thin film composed of a single element.	4
1.3	Thin film evaporator. A thermal source is shown on the left and an electron-beam source on the right.	7
1.4	Pulsed laser deposition system.	9
1.5	Magnetron sputter deposition system. A DC power supply shown on the left and an RF power supply on the right.	10
1.6	Two examples chemical vapour deposition systems. Left side shows a plasma-enhanced CVD and right side shows thermally assisted CVD.	12
1.7	A level set implementation of a phase transformation simulation.	18
2.1	Phase diagram of aluminum–molybdenum taken from data given by Saunders. Dashed lines are estimated phase boundaries. . .	22

LIST OF FIGURES

2.2 Calculated Gibbs energy of fcc, bcc and amorphous Al-Mo phases at 298 K. Crystalline phases were treated as disordered solid solutions and the Miedema approach was used for the amorphous phase. 25

2.3 SEM micrographs of sputtered Al-Mo films. 26

2.4 X-ray diffraction scans of Al-Mo thin films. Crystalline peaks and an amorphous hump are labeled. 27

2.5 Cross-sectional bright-field TEM micrographs of (A) pure Al, (B) Al-8 at.%Mo, (C) Al-32 at.%Mo and (D) Al-50 at.%Mo thin films. 29

2.6 TEM micrographs of Al-32at.%Mo: (A) representative HRTEM, (B) SAD and (C) dark-field TEM cross-section taken from innermost ring. 29

2.7 HRTEM micrograph of Al-16at.%Mo (left) and Al-50at.%Mo (right), with digital diffractograms inset. 30

2.8 Surface slopemaps of Al-Mo films taken from AFM scans. Note the differing scalebar dimensions. 31

2.9 Root-mean-square (RMS) surface roughness of Al-Mo films. 32

2.10 Height difference correlation functions of Al-Mo films. Mean correlation length is marked for each composition. 33

2.11 Structure zone map describing the surface of Al-Mo thin films. 34

2.12 Al-Mo Resistivity measurements. Best fit of Equation 2.3.8 also plotted. 35

LIST OF FIGURES

2.13	Al–Mo nanoindentation measurements. (A) Hardness and (B) elastic modulus.	37
3.1	Process flow for fabricating nanoscale Al–Mo cantilevers.	41
3.2	(A) Bank of 400 nm wide cantilevers with lengths from 1 to 8 μm fabricated from 20 nm thick Al-32 at.%Mo. (B) Close-up of 8 μm long cantilever.	42
3.3	A singly-clamped metal resonator.	43
3.4	Measured power spectrum of a cantilever fabricated from Au–Hf. Best fit of Equation 3.2.6 shown.	45
3.5	Optical interferometer setup for measuring frequency response of nanoscale devices.	46
3.6	Resonant frequencies of Al–Mo devices measured with optical interferometry.	48
3.7	Quality factors of Al–Mo devices measured with optical interferometry.	49
4.1	Initial grain orientations distributions from left to right: bi-ased towards fastest growth direction, uniform and biased away from fastest growth direction. Fastest growth direction and rings showing the direction of integration are plotted on each spherical pole figure.	53
4.2	A deletion event between two conic grains at time t in the time interval Δt . Isocontours are shown at different heights. Note that the primary axis of both cones are the same length.	55

LIST OF FIGURES

4.3	Geometry of a cross-section of the cone with tilt angle θ' in the deletion plane shown in Figure 4.2.	56
4.4	Examples of competitive conic grain growth from level set simulations at various thicknesses. Surfaces are shaded by x-direction slope and cross-sectional slices also shown. Potential deletion zones marked in red.	59
4.5	Comparison of the grain distribution at four different film thicknesses between analytic growth model and level set simulation for the cases where the initial distribution is (a) biased towards the fastest growth direction, (b) uniform and (c) biased away from the fastest growth direction.	60
4.6	(a) RMS surface roughness and (b) probability of grain survival calculated from the analytic growth model for the three cases described in Figure 4.1. Power laws are shown in both graphs as dotted lines.	64
5.1	(A) Plot of face velocity versus orientation. (B) Kinetic Wulff construction from (A). (C) Initial circular grain evolving asymptotically into equilibrium Wulff shape.	69
5.2	(A) Top view and (B) 3D view of an example film surface in late-stage growth. (C) Pyramidal crystal top. (D) Equivalent cone crystal top to (C).	72
5.3	Various kinetic Wulff shapes and their associated pyramidal crystal tops in late-stage growth. Pyramid base area is constant in these images. Arrows show fastest growth direction.	73
5.4	Surface slope-maps and $\langle 111 \rangle$ stereographic projections of all $\{111\}$ poles for tetrahedral crystals at various thicknesses.	77

LIST OF FIGURES

5.5	Surface slope-maps and $\langle 111 \rangle$ stereographic projections of all $\{111\}$ poles for great rhombicuboctahedral crystals at various thicknesses.	77
5.6	Surface slope-maps and $\langle 111 \rangle$ stereographic projections of all $\{111\}$ poles for cubic crystals at various thicknesses.	78
5.7	Probability of grain survival for different crystal geometries measured from simulation. Gray lines show asymptotic best fits.	80
5.8	Surface roughness for different crystal geometries measured from simulation. Gray lines show asymptotic best fits.	80
5.9	Mean grain diameter prefactor d_∞ as a function of N_d and the geometric crystal top ratio l/\sqrt{A} plotted from Equation 5.5.1. The locations of various kinetic Wulff shapes are also shown.	82
5.10	Prefactors of grain survival probability measured from simulations of diamond crystals. Gray line shows predictions from Equations. 5.3.2, 5.3.4 and 5.5.1. Some kinetic Wulff shapes shown above.	83
5.11	Prefactors of surface roughness measured from simulations of diamond crystals. Gray line shows predictions from Equations. 5.3.2, 5.3.7 and 5.5.1. Some kinetic Wulff shapes shown above.	83
6.1	AFM slopemaps of sputtered Al thin films at four different thicknesses. Each slopemap has side length $2 \mu\text{m}$	89
6.2	Scaling exponents of sputtered Al films measured over different length scales.	90

LIST OF FIGURES

6.3	(a) Self-shadowing of incoming flux on an example surface. Flux received at each point is decreasing from left to right. Note that the flux received by each face is the sum of all points on that face. (b) Angular distribution of rays for different deposition techniques.	93
6.4	Surface morphology and texture of cubic simulations.	97
6.5	Surface morphology and texture of cuboctahedral simulations.	97
6.6	Surface morphology and texture of rhombicuboctahedral simulations.	98
6.7	Cross-sectional slices of a) cubic and b) rhombicuboctahedral simulations with different values of N . Note that the coloring reflects the grain direction perpendicular to the substrate, and that the cubic $N = 0$ simulation was stopped early because the number of surviving grains dropped too low.	100
6.8	RMS surface roughnesses plotted against mean thickness for different crystal systems and N values.	101
6.9	Grain probability of survival calculated from cubic simulations. Solid lines are calculated from film surface and plotted against mean thickness. Dashed lines are calculated from slices and plotted against slice height. Two example power laws are shown in black.	102
6.10	Porosities measured from slices for different crystal systems and N values.	103
6.11	Scaling and probability of grain survival exponents measured in the current study. Dashed lines show the expected exponents for the case where facet growth velocities are constant.	105

LIST OF FIGURES

6.12 Double wedge sample preparation technique for cross-sectional samples created by Spiecker et al. The deposited film (a) is first dimpled hemispherically at a low angle (b). The sample is then tripod polished with a linear slope on the bottom (c). The resulting double-wedge then has electron transparent slices at various thicknesses. These thicknesses are measured optically using an interference technique. 106

6.13 Measured mean grain diameter versus grain thickness for SiC growth by LPCVD, taken from Spiecker et al. The expected power for non-self-shadowed growth of 0.4 is also shown. . . . 107

6.14 Comparison between scaling exponents measured in the current study of faceted film growth with those measured by Yanguas-Gil et al. for non-faceted film growth. 108

6.15 Measured scaling exponents of self-shadowing simulations with different N values measured over different length scales. Curves are drawn as guides for the eye. 109

A.1 Probability distribution of distances to nearest random point on a periodic 2D surface for different point densities. 121

List of Tables

2.1	Crystal structures and heats of formation of Al–Mo compounds. x is the fraction of Mo.	22
3.1	Transverse modal parameters of a singly-clamped resonator.	44
5.1	Growth parameters of the diamond system.	76

List of Symbols

Symbol	Meaning [units]	Symbol	Meaning [units]
$\langle A \rangle$	Mean grain area	m	Mass [g]
α	Roughness exponent	N	Number of mols
β	Scaling exponent	$\langle P \rangle$	Grain survival probability
$\langle d \rangle$	Mean grain diameter	π	I like pie
δ	Dilation factor	Q	Quality factor
	Thickness [m]	R	Measured resistance [Ω]
E	Young's modulus [Pa]		Deposition rate [A/s]
	Energy [J]	ρ	Resistivity [Ω m]
f	Frequency [1/s]		Molar density [mol/m ³]
ΔG	Gibbs energy [J/mol]		Angular flux distribution
H	Correlation measure	S	Structure factor
h	Thickness [m]	σ	Surface roughness [m]
ΔH	Enthalpy [J/mol]	T	Temperature [K]
I	Signal intensity [W]	t	Time [s]
J	Texture index	τ	Nucleation time [s]
k	Spring constant [N/m]		Thickness [m]
k_B	Boltzmann constant		Crossover thickness [m]
κ_T	Compressibility [m ² /N]	X	Molar fraction
L	In-plane length scale [m]	w_0	Angular frequency [rads/s]
λ_n	n th Modal parameter		

List of Abbreviations

Abbreviation	Meaning
AFM	Atomic force microscopy
BD	Ballistic deposition
CALPHAD	Calculation of phase diagrams
CVD	Chemical vapour deposition
DC	Direct current
EDXS	Energy-dispersive x-ray spectroscopy
HDCF	Height-difference correlation function
HRTEM	High resolution transmission electron microscopy
LPCVD	Low pressure chemical vapour deposition
LSM	Level set method
GB	Grain boundary
MBE	Molecular beam epitaxy
MD	Molecular dynamics
ODF	Orientation distribution function
PLD	Pulsed laser deposition
PMMA	Poly(methyl methacrylate)
RF	Radiofrequency
RMS	Root mean square
SEM	Scanning electron microscopy
STM	Scanning tunneling microscopy
SZM	Structure zone map
TEM	Transmission electron microscopy
XRD	X-ray diffraction

1

Introduction to Thin Films

1.1 Thin Film Technology and Materials Science

Thin films are an essential part of a very large number of technologies. A thin film is any material layer applied to a substrate, with thicknesses ranging from single atomic layers to hundreds of micrometers. Thin films can be fabricated in a variety of ways out of almost any solid material. Thin film technologies include semiconductor microelectronics, magnetic data storage, optical coatings to improve reflection or transmission, anti-scratch and anti-corrosion coatings, photonics, photo-voltaic cells, supported catalysts, thermal barriers

and microfluidics. All of these applications and more are currently the focus of intense scientific study.

Materials science is central to advances in thin film technologies. Examples are understanding the role of defects in semiconductor electronic properties and failure times, creating alloys with optimum magnetic properties and reducing interfacial roughness between different thin film solar cell layers. Materials science teaches us how to relate underlying microscopic structure of materials to their macroscopic properties. Thin film materials research may now encompass optimizing fabrication routes, micro- and macro-scale characterization, detailed predictive models and many forms of computer simulation. Simulation especially has become an invaluable tool for a materials scientist in the past few decades, a direct consequence of massive increases in computing power.

1.2 Structure

As in bulk materials, the microstructure of a solid thin film can be amorphous, single crystalline or polycrystalline. A mix of different phases is also possible; these are termed composite materials. Thin film examples of these three microstructures are shown in Figure 1.1. A scanning tunneling microscope (STM) heightmap of a single crystalline gold surface taken from [1] is shown in Figure 1.1A. Atomic terraces (composed of individual monolayers) are the dominant surface structure in this image. A heightmap captured with atomic force microscopy of polycrystalline nickel deposited by sputtering at 400 °C is shown in Figure 1.1B. In this micrograph, large faceted grains are visible. Finally, an AFM heightmap of co-sputtered amorphous Al-32 at.%Mo is shown in Figure 1.1C. Rounded cusps are visible, but the origin of this surface structure is the stochastic and diffusive nature of the film deposition; there is no clear microstructural boundary between them.

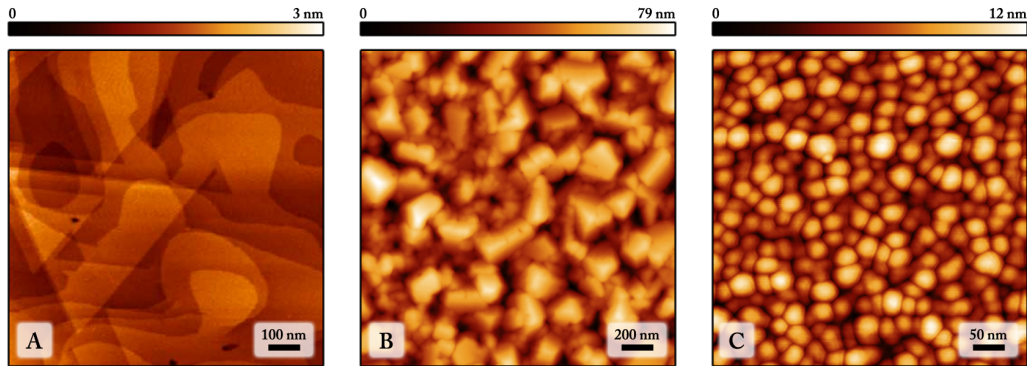


Figure 1.1: Heightmaps of different thin film types: (A) Single crystal gold surface fabricated by Lüssem et al. (B) Polycrystalline nickel surface. (C) Amorphous Al-32 at.%Mo surface.

Figure 1.2 depicts the local structure of these three microstructures atomistically from a single element. The basic characteristics of these three structures are sketched below. For the sake of simplicity, we will consider only materials composed of a single element here.

1.2.1 Single Crystal

Because thin films can be grown atom by atom, it is possible to grow pure single crystals of many materials epitaxially onto a substrate. In many cases single crystals of a material can electronically or physically outperform their polycrystalline or amorphous analog. Unfortunately fabrication of large dimension single crystals is typically quite costly. Silicon photovoltaic cells are the prototypical example of such a material used in single crystal form to improve electrical properties [2]. An example of single crystal materials created for superior mechanical properties at high temperatures are turbines fabricated from nickel super alloys [3].

As shown in Figure 1.2, the dominant feature of a single crystal thin film is its

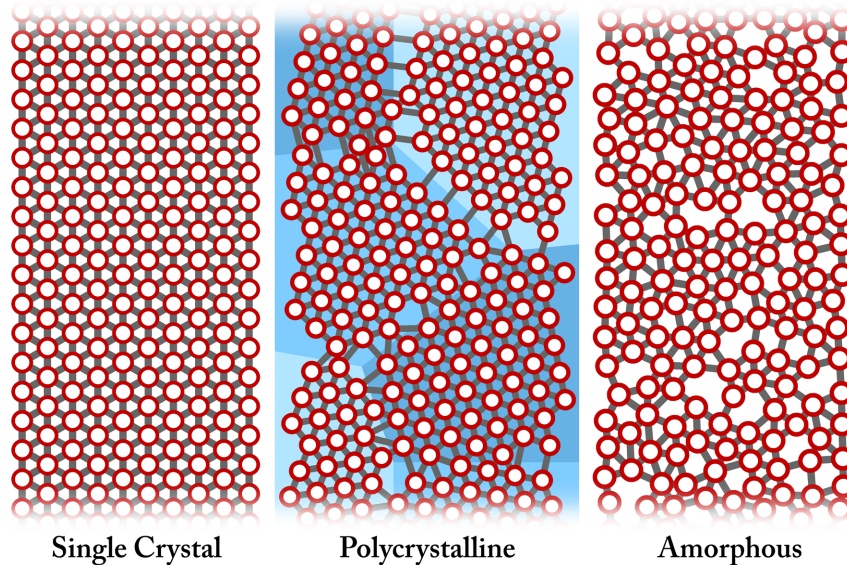


Figure 1.2: 2D atomistic view of the possible microstructures of a solid thin film composed of a single element.

extreme long-range order. Each atom belongs to the same grain and as such there are no grain boundaries present. The conductivity of such a structure is as high as possible for a given temperature, because the mean free path of the conduction electrons is as long as possible. The structure cannot be defect-free however; entropic concerns dictate that some vacancies (empty lattice sites) and self-interstitials are present in small numbers. Additionally, if the film was grown epitaxially onto a material with a different lattice parameter, strain will generate misfit dislocations near the film-substrate interface to relieve stress.

1.2.2 Polycrystalline

A polycrystalline microstructure is also plotted in Figure 1.2. The structure consists of a network of crystalline regions termed *grains*. Each grain has a unique crystallographic orientation given by its three Euler angles. Within a given grain, there is long-range order between all constituent atoms. Between

the grains are *grain boundaries* (GBs). A GB requires 5 angles for unique identification. These boundaries typically are less dense than the continuous crystalline regions and may contain relaxed atoms that do not belong to either parent grain (i.e. they fall on neither parent lattice). A GB can be low-angle or high-angle, referring to the angular misorientation of the two neighboring lattices. The cut-off between low- and high-angle boundaries is typically taken to be $\simeq 11^\circ$. The GB on the bottom-right of the polycrystalline material in Figure 1.2 could be classified as a low-angle GB.

Polycrystallinity can strongly modify the mechanical [4, 5], electrical [6, 7] and thermal [8, 9] properties of a thin film from those of its single-crystalline counterpart. Film morphology strongly depends on the deposition technique and parameters used to fabricate it. Because of the large number of possible deposition parameters, many different models have been proposed to explain various aspects of polycrystalline thin film growth [10]. The dominant surface features of many polycrystalline thin films are low-index crystalline facets. The growth rate of these facets determines the equilibrium grain shape (referred to as the kinetic Wulff shape [11]) if the diffusion rate along the low-index facets is much higher than the rate of other diffusion events [12].

1.2.3 Amorphous

The right of Figure 1.2 shows an amorphous microstructure. This structure is characterized by its complete lack of long- and medium-range order. Only the first atomic shell around any given atom is ordered, enforced by the strong repulsion of atomic cores. An amorphous microstructure can be formed in a few different ways. The first is deposition onto a cryogenically-cooled substrate. By dramatically lowering the diffusion energy available to adatoms on the deposition surface, the deposition noise can be *frozen in*. In fact, any material can be made amorphous if the cooling rate from the gas or liquid

state is fast enough. Vapour phase deposition, described in more detail below, especially lends itself to extremely high quenching rates. Alternatively, an initially crystalline or polycrystalline thin film can be *amorphized* by irradiation of electrons or ions [13].

1.2.4 Nanocrystalline

Finally, a note on so-called nanocrystalline microstructures. These consist of very fine polycrystalline microstructures with nanoscale grain dimensions. In this case, a very high fraction of atoms are either on the grain boundaries or in very close proximity. Therefore the material properties of nanocrystalline materials are heavily dominated by the structure and density of the boundaries [14]. Because of the atomic nature of thin film fabrication, nanocrystallinity is extremely common in polycrystalline thin films.

1.3 Deposition Techniques

Thin film fabrication typically involves condensing a gas phase of one material onto a substrate of another material. Some technologies do deposit thin films from a liquid phase, but the work in this thesis is limited to vapour phase deposition. Vapour phase deposition techniques fall into two main categories; physical and chemical. Physical deposition includes sputtering, evaporation and pulsed-laser deposition. An example of a chemical process is chemical vapour deposition. Additionally, some techniques such as reactive sputtering or evaporation use both physical and chemical deposition processes. These techniques are explained in more detail below.

1.3.1 Evaporation

Perhaps the simplest deposition technique is to add enough energy to a given material in a vacuum chamber for it to evaporate or sublime into a gas phase. If the total pressure in the vacuum chamber is low enough, the mean free path of all gaseous atoms will be much larger than the chamber dimensions. The gaseous flux of free atoms will therefore deposit on any surface in the chamber with line-of-sight to the source material. In this way a thin film of almost any pure element can be controllably deposited onto a substrate placed facing the source. The needed energy can be added simply by electrical resistive heating of the source material or by more exotic means such as an electron-beam. Thermal evaporation is very simple to design and run but electron-beam evaporators allow for more localized heating. Both types of evaporation sources are shown in Figure 1.3.

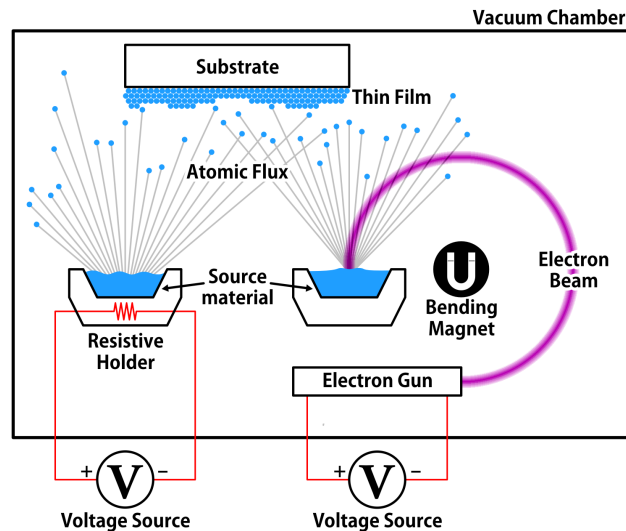


Figure 1.3: Thin film evaporator. A thermal source is shown on the left and an electron-beam source on the right.

Evaporation is best-suited to depositing pure materials at high deposition rates. Deposition of an alloy or compound with this technique is difficult,

as most materials have different melting points and vapour pressures. The simplest method to deposit multiple elements simultaneously is to have a different evaporation source for each; care must be taken however to avoid cross-contamination between sources.

1.3.2 Pulsed Laser Deposition

Another physical vapour thin film fabrication technique is pulsed laser deposition (PLD), depicted in Figure 1.4. In this technique, a high-energy laser is focused on a target inside a vacuum chamber. The focused laser spot vapourizes the material into a gaseous, ionized plume. This material can be deposited as a thin film onto a substrate placed in the path of the plume. This method is conceptually simple, but the physics of the laser-target interaction are very complex and the non-linear processes thereof can cause deposition errors such as large cluster or particulate deposition. To avoid over-heating or damaging the target, the laser beam may be rastered over the material surface and/or the material target may be continually rotated and translated.

The primary use of PLD is to deposit complex compounds stoichiometrically. Most complex materials will not be uniformly evaporated or sputtered. The plasma plume created by PLD however can be made to have virtually the same composition as the target. A large number of variables can be adjusted as well, including laser power and pulse rate, the angle of the beam with respect to the target and target rotation/translation speed.

1.3.3 Sputtering

Sputtering is the process of using ionized noble gas atoms (typically argon) to kinetically eject atoms from a target surface in a vacuum chamber, shown in Figure 1.5. Sputtering requires creation of a sustained plasma created by

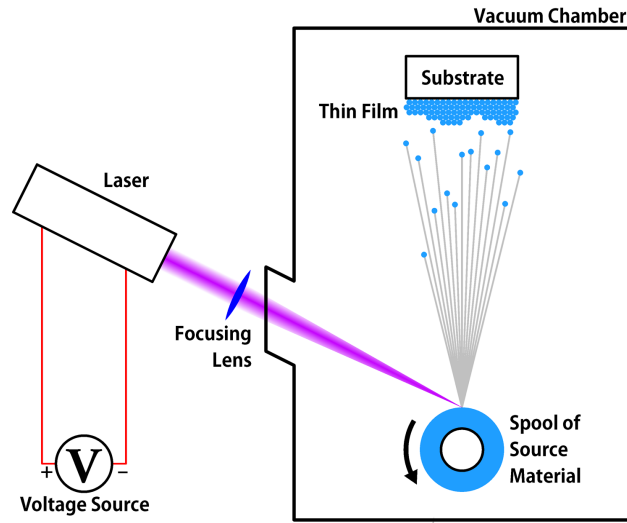


Figure 1.4: Pulsed laser deposition system.

ionizing the injected noble gas. In DC sputtering, the entire vacuum chamber and most equipment inside are grounded, save for the deposition target which is kept at a large negative potential. This accelerates the sputtering ions towards the target surface at high velocity, which in turn causes a cascade of collisions on the target surface. Some of the target atoms are ejected and travel across the deposition chamber to deposit a thin film on a substrate.

The most common form of sputtering is referred to as magnetron sputtering, where powerful magnets are mounted behind the target. The local density of magnetic field lines increases and traps electrons, which causes a much higher ionization fraction of the sputtering gas at the target surface. Deposition rates can be increased by an order of magnitude via magnetron sputtering.

DC magnetron sputtering is used to deposit highly conductive materials such as metals. To sputter dielectric materials, a radiofrequency (RF) or pulsed-DC power supply must be used. The periodic polarity reversal of the target potential prevents charge buildup and allows deposition to continue. RF sputtering can be used to deposit virtually any material, but at only at much slower rates

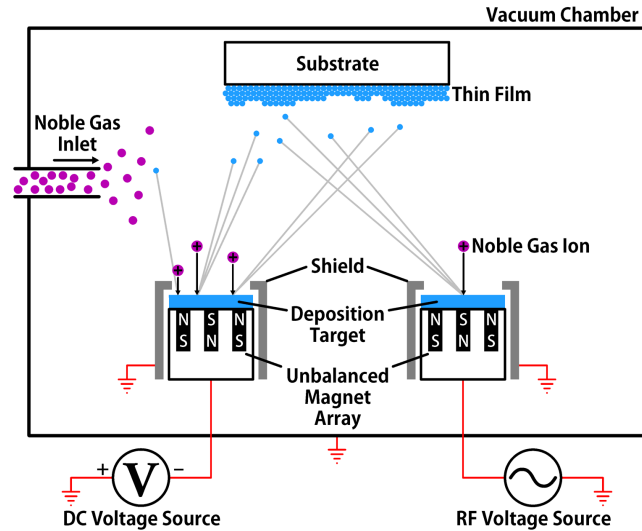


Figure 1.5: Magnetron sputter deposition system. A DC power supply shown on the left and an RF power supply on the right.

than possible with DC magnetron sputtering.

Because sputtering requires noble gas pressures in the Millitorr range, the sputtered atomic flux can be partially thermalized enroute to the substrate by collisions with the noble gas atoms. This has the effect of broadening the angular deposition of deposition atoms, making sputtering less useful for deposition of material into trenches. Another limitation of sputtering is that maximum deposition rates are generally lower than the rates possible with evaporation or PLD. This means that sputtering requires a high vacuum level to avoid contamination with oxygen and other other gases.

1.3.4 Reactive Physical Vapour Deposition

A simple modification to the above techniques is to introduce a background gas such as oxygen or nitrogen. A chemical reaction then proceeds in parallel with the physical deposition, either at the target or substrate surface. In this

way, oxides, nitrides and other compounds and be deposited from a single pure elemental target. Adjusting the partial pressure of the background gas allows for careful stoichiometric control.

Sputtering is the most common reactive physical vapour deposition technique. This deposition process must be carefully monitored however, since formation of the reactive compound on the target can decrease the sputtering rate and thus form an even thicker layer of the reactive compound. This feedback loop can harm film uniformity and dramatically lower deposition rates. More information on potential issues with reactive sputtering are given by Safi [15].

1.3.5 Chemical Vapour Deposition

A broad category of deposition techniques fall under chemical vapour deposition (CVD). The basic characteristics are reacting chemical precursors inside a chamber on a substrate, resulting in the deposition of a film. A schematic of this process in two possible configurations are shown in Figure 1.6. Many different materials can be deposited using CVD techniques, and CVD can be modified in many ways such as plasma- or microwave-enhancement, liquid injection and low pressure CVD. Figure 1.6 shows both plasma-enhanced and thermally-assisted CVD.

CVD also offers the possibility of easier scalability than physical techniques, since line-of-sight between the target and substrate is not necessarily required. Doping films of semiconducting films is also easily accomplished in CVD. For these reasons, and the extensive development CVD deposition of semiconductor film deposition, CVD is central to integrated circuit manufacture.

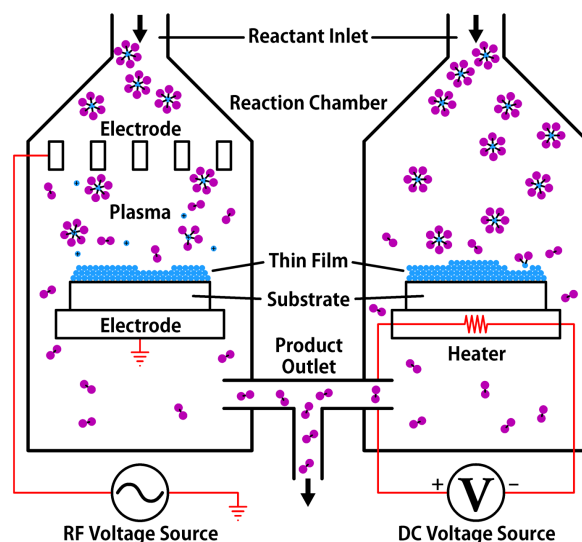


Figure 1.6: Two examples chemical vapour deposition systems. Left side shows a plasma-enhanced CVD and right side shows thermally assisted CVD.

1.4 Characterization Techniques

Numerous techniques exist to understand the microstructure, surface structure and physical properties of thin films. In this section, we outline the techniques employed in this thesis.

1.4.1 X-ray Diffraction

X-ray diffractometry (XRD) is a simple, non-destructive technique to characterize microstructures. In this technique, a beam of monochromatic light with a wavelength on the order of angstroms is focused onto a sample. These *x-rays* are scattered by the sample atom's electrons. If the sample atoms are arranged in a crystallographic lattice, the x-rays diffract in a manner described by Bragg's law or the Laue equations. This *diffraction pattern* provides fairly unique identification of the sample lattice(s) present and furthermore con-

tains information about the local lattice strain and crystalline grain size. It is also possible to use x-rays to analyze amorphous microstructures, though these studies typically require additional structural information. Another advantage of XRD is that the sample can be analyzed in air as opposed to the vacuum required for electron probe techniques.

XRD is of particular importance for characterizing thin films, since the interaction depth is on the scale of hundreds of nanometers to single-digit microns, the same thickness of many thin films. Other x-ray scattering techniques such as x-ray reflectometry or x-ray fluorescence can be performed with the same x-ray source used for diffraction. These techniques are also useful for thin film structural characterization. The reader is referred to the excellent book written by Birkholz et al. for more information [16].

1.4.2 Transmission Electron Microscopy

Currently the most powerful technique for microstructural examinations is transmission electron microscopy (TEM). In a TEM experiment, a beam of electrons is focused into a small spot onto a sample thin enough to be electron transparent. The electrons beam is high energy and nearly-monochromatic. Depending on the focal conditions, either an image of the local sample structure or a diffraction pattern carrying crystallographic information can be formed. It is these dual information channels with both inverse and regular spatial information from the same region of a given sample that makes TEM so powerful.

The disadvantages of this technique are that the sample must be placed in a high vacuum chamber, and must be extremely thin. Some samples are also prone to radiation damage. Lastly, the micrograph interpretation is not as straightforward as other techniques, since structural and topological information are often convolved. A comprehensive reference for TEM theory and

technique is the textbook written by Williams and Carter [17].

1.4.3 Scanning Electron Microscopy

Scanning electron microscopy (SEM) is used to probe the surface of a sample by rastering an electron beam at high speed, line by line. Secondary or back-scattered electrons are collected by a detector to form a micrograph of the sample surface. This technique works better on conductive surfaces. A dielectric sample may need to be coated with a thin layer of metal to improve micrograph quality. This technique typically requires the sample be placed in a vacuum, though some modern SEM setups allow imaging in environmental conditions. A review of the history of SEM can be found in an article by Smith and Oatley [18].

1.4.4 Energy-Dispersive X-ray Spectroscopy

When a sample is bombarded with electrons in either an SEM or a TEM, some electrons of the inner orbitals from the sample atoms are excited into higher orbitals, or even ejected. When a higher energy level electron drops into the hole, an x-ray with a specific energy value may be ejected. The intensity and energy values of the emitted x-rays uniquely identify the element(s) present in the sample. This characterization method is referred to as energy-dispersive x-ray spectroscopy (EDXS). The spatial resolution of EDXS is sufficient to create a compositional map of a sample, with the resolution dependent of the electron beam focal spot diameter. More information can be found in the book by Grieken and Markowicz [19].

1.4.5 Atomic Force Microscopy

Atomic force microscopy (AFM) is one member of the scanning probe microscopy (SPM) family of characterization techniques. In AFM, a cantilever with an extremely sharp protrusion (called a tip) near the unclamped end of the cantilever is brought close to a surface using piezoelectric transducers. The cantilever is designed to have a spring constant much less than the force between neighboring atoms; this allows the AFM to sense the distance from the nearest sample surface features to the tip by optically measuring the displacement of the cantilever.

This displacement is typically accomplished in one of two ways. In contact mode, the the tip physically contacts the surface. In tapping mode, the cantilever is driven at one of its transverse natural frequencies in the direction parallel to the sample surface. When the surface is close to the tip, it exerts a damping force on the resonating cantilever. The power required to correct for this minute frequency change is proportional to the distance from the tip to the sample surface. Tapping mode requires more complex electronics, but has the advantage of not contacting the surface, which could potentially wear away the sample or the tip. In both modes, the optical detection usually involves bouncing a laser off the free end of the cantilever and using a split photo-diode to detect cantilever motion. More information on AFM and its history can be found in an article written by Rugar and Hansma [20].

1.4.6 Nanoindentation

Mechanical testing of thin film samples presents unique challenges because of the small dimensions involved. Deconvolving the properties of a very thin film from that of its substrate requires unique tools. Nanoindentation provides a way to perform indentation tests on extremely small volumes. Both the

hardness and the elastic modulus can be measured by applying small forces to a Berkovich diamond tip placed on a sample surface, with a precise measurement of the distance travelled by the indenter. The methodology employed for the nanoindentation measurements in this thesis is that of Oliver and Pharr. A recent review authored by them outlines this methodology [21].

1.4.7 Four Point Probe

Since a thin film has thickness well below the spacing of the measurement probes, the resistivity ρ can be calculated as

$$\rho = \frac{\pi}{\ln 2} hR \quad (1.4.1)$$

where h is film thickness and R the measured resistance from the 4-point probe. Note that Equation 1.4.1 assumes that the film covers an infinite area; this assumption is justifiable since our measurements were made on a thin film covering a 10 cm wafer with a probe spacing of under a centimeter.

1.5 Simulation Techniques

In the past few decades computational materials science has expanded dramatically [22], paralleling the vast increase in availability of computational power. In fact virtually no areas of study in materials science do not employ some simulations. One reason is that experiments that are extremely difficult or impossible to run can often be simulated. Another is the speed and fidelity possible with modern simulation techniques outperforms that of virtually all experiments. Thin film science is no exception; many different techniques have been employed to understand a wide variety of phenomena [23]. In this section we therefore restrict discussion to only the simulation techniques used in this thesis.

The modelling and simulation studies presented in this work in Chapters 4 and 5 respectively deal with polycrystalline thin film growth. Even in nanocrystalline materials, the number of atoms present in a large ensemble of grains is still too large to simulate with molecular dynamics (MD). For example, consider a thin film of thickness of 1 μm containing cylindrical grains of aluminum 50 nm in diameter. The volume of each grain would be $1.96 \times 10^9 \text{ \AA}^3$. The atomic density of Al is 0.058 atoms / \AA^3 , giving approximately 10^8 atoms / grain. Typical modern MD simulations employ up to a million atoms over timescales of femtoseconds [24]. It is therefore impossible to use MD to simulate the growth of even one large grain, let alone the dynamics of hundreds of interacting grains. The timescales are even more intractable, since most thin film depositions require minutes if not hours.

1.5.1 Level Set Simulations

The level set method (LSM) provides a powerful means to compute complex interfacial and geometric structures. Essentially, LSM parameterizes objects in higher dimensional space than the problem and then projects these objects onto a cartesian grid. The reason this method is so powerful is that it removes the need to compute the geometric configuration explicitly.

As an example of the LSM, consider the growth and nucleation of a secondary phase in a 2D field whose interfacial velocity depends on its crystallographic orientation. If there are a very large number of nuclei, explicit computation of the overlapping nuclei may be infeasible. If each nuclei has the interfacial velocity

$$v(\theta) = 1 + \frac{\cos(4\theta)}{20} \quad (1.5.1)$$

where θ is the local orientation of a given nuclei. The interface radius of each

nuclei is therefore given by

$$r(\theta, t, \tau) = \left[1 + \frac{\cos(4\theta)}{20} \right] (t - \tau) \quad (1.5.2)$$

where τ is the nucleation time. In the LSM for this problem we consider time t as the third dimension; one dimension higher than the problem dimensionality. Figure 1.7 shows a graphical representation of how the algorithm progresses. As the nuclei move in the higher dimensional representation, the interfaces in the simulation plane expand. Since the overlapping nuclei areas are implicit, no additional calculations are needed beyond the projection and boolean comparisons. This is because the interface does not need to be explicitly mapped. Instead, a grid is overlaid onto the simulation space. Each grid point can be checked to see if it falls inside the transformed fraction using Equation 1.5.2 with respect to the origin of each nucleated grain.

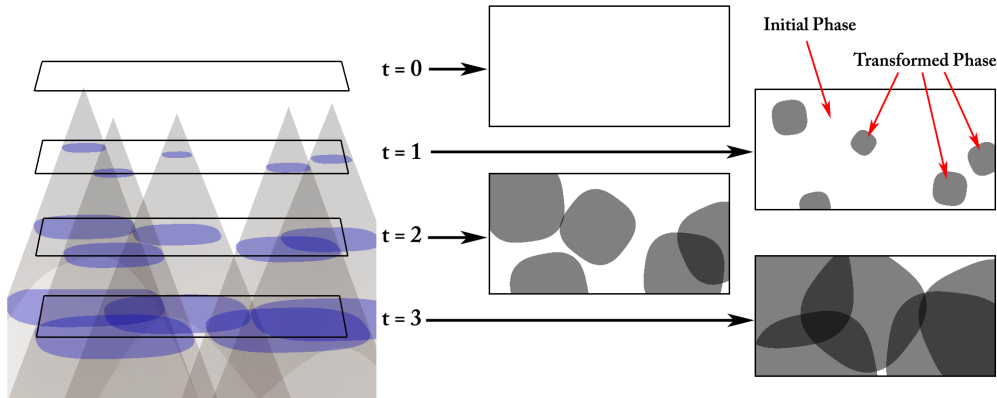


Figure 1.7: A level set implementation of a phase transformation simulation.

Calculating statistics such as fraction transformed or interfacial length are dramatically simplified when using level sets. This method is used in the simulations of Chapters 4, 5 and 6. More information on applying this method to grain growth simulations is given in [25].

2

Design of an Aluminum–Molybdenum Alloy For Nanoscale Applications ^{1 2}

2.1 Motivation

The continuing miniaturization of many different devices is a subject of intense scientific study [26, 27]. Currently, most structural components in nanoscale devices are fabricated from Silicon or a silicon-based semiconductor such as

¹Material in this chapter has been published in:

▶ Z Lee, C Ophus, LM Fischer et al. (2006) *Nanotechnology* 17: 3063-3070

▶ C Ophus, EJ Lubber, M Edelen et al. (2009) *Acta Materialia* 57: 4296-4303

²The thermodynamic modeling in this chapter was performed by M Edelen and D Lewis of the Rensselaer Polytechnic Institute.

Si_3N_4 or SiC [28]. Silicon is easy to etch, elastically stiff, very hard and has the advantages of already being integrated into most microscale fabrication technologies. However, silicon has low conductivity and reflectivity even when doped. The typical solution in applications which require conductivity or reflectivity is to coat the silicon device with a metal, though this often leads to problems with differential stress between the layers [29] or unwanted excess energy dissipation from the coated devices [30]. Silicon also has low fracture strength and poor wear resistance, which lowers reliability of moving components [31]. New materials will be needed as the scope of nanotechnology increases and many more applications become accessible [32, 33].

An alternative solution to coating semiconducting beams with a metal is to fabricate all-metal devices. Metals possess much higher conductivities and reflectivities and can possess ductile fracture modes which can prevent sudden, total failure of nanoscale devices. However, pure metals generally suffer from low strength and possibly high intrinsic stresses due to the high deposition energies [34]. Additionally, if the metal thin film is polycrystalline it may have an extremely rough surface composed of crystalline facets [25]. A potential solution to these issues is to use an metallic alloy as opposed to a pure metal film.

In this chapter we discuss the fabrication and characterization of a metallic alloy for nanoscale resonator applications. The desired material properties of this alloy are high conductivity, reflectivity and strength, as well as a microstructure that is fully dense and uniform. The alloy should be primarily composed of an element that is easy to etch chemically to facilitate fabrication of nanoscale devices from it.

2.2 Background

2.2.1 Aluminum–Molybdenum

The starting material for our study is aluminum. Aluminum is very conductive, easy to etch and like copper has been used extensively in the microelectronics industry, and so is easily integrated into existing processes. Other authors have already proven that Al can potentially replace Si as the structural material for resonators [35]. It is however very soft and when vapour deposited it forms very large grains due to its low melting point. We have chosen to alloy Al with Molybdenum, an extremely hard refractory metal. In industry, the primary use of aluminum-molybdenum alloys is wear- and corrosion-resistant coatings with high hardness and good thermal stability, especially for coating Al-based light alloys [36]. These alloys have similar wear and corrosion properties to cadmium, but without the associated toxicity [37]. The phase diagram of Al–Mo is shown in Figure 2.1. The equilibrium crystal structures of Al–Mo are listed in Table 2.1, as well as the measured heats of formation (where known). In this table, crystallographic information is taken from Saunders [38] and thermodynamic data from Shilo and Franzen [39].

From the phase diagram, we see that Al and Mo have several equilibrium intermetallics and virtually no low-temperature solubility in each other. This indicates that Al and Mo compounds have a strong negative heat of formation. Calculations by Du et al. [40] and experimental measurements by Shilo and Franzen (shown in Table 2.1) confirm this.

However, elements deposited from vapour do not necessarily form equilibrium phases. This is because *vapour phase quenching* of the atoms from a gas state to solid involves extremely high cooling rates. This massive undercooling often favours phases with lower nucleation barriers [41]. Metastable phases, especially super-saturated variations of the parent elemental phases, are commonly

CHAPTER 2: AL-MO ALLOY DESIGN FOR THIN FILM APPLICATIONS

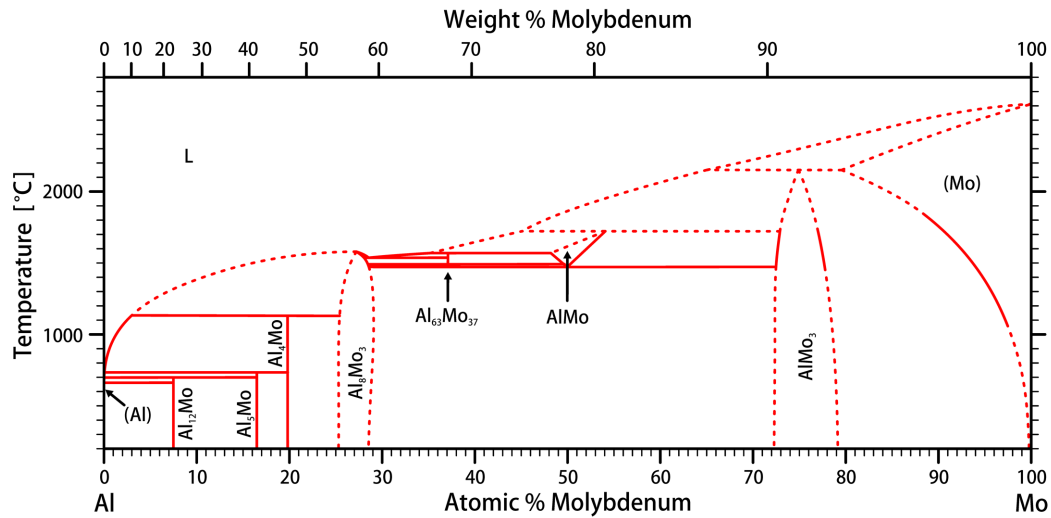


Figure 2.1: Phase diagram of aluminum–molybdenum taken from data given by Saunders. Dashed lines are estimated phase boundaries.

Table 2.1: Crystal structures and heats of formation of Al–Mo compounds. x is the fraction of Mo.

Phase	Composition at.% Mo	Spacegroup	Heat of Formation kJ/mol atoms
(Al)	0–0.06	$Fm\bar{3}m$	
Al ₁₂ Mo	7.7	$Im\bar{3}$	
Al ₅ Mo	16.7	$P6_3$	
Al ₄ Mo	20	Cm	
Al ₈ Mo ₃	31.3	$C2/m$	-39.3
Al ₆₃ Mo ₃₇	37		
AlMo	48–54	$Im\bar{3}m$	-31.3
AlMo ₃	73–78.5	$Pm\bar{3}n$	-21.4
(Mo)	79.5–100	$Im\bar{3}m$	$253(1-x)^2 - 111(1-x)$

observed.

In a system like Al–Mo we would expect vapour phase quenching to produce three possible phases. The first two are the parent Al phase (face-centred cubic) and the parent Mo phase (body-centered cubic). The third is an amorphous phase, specifically a conventional metallic glass previously described in Section 1.2.3. The equilibrium intermetallics have much more complex unit cells, and so we expect formation of their nuclei to be kinetically barred for all stoichiometries.

Perepezko has proposed one way of estimating the compositional boundaries of metastable phases produced by large undercooling, metastable extensions of the liquidus curves [41]. In this study, we have opted instead to examine the thermodynamics of the possible metastable phases. Gibbs energy calculations of the supersaturated disordered solid solutions of Al and Mo are straightforward using the Calculation of Phase Diagrams (CALPHAD) method and will not be described here [42].

To estimate the Gibbs energy of the amorphous phase, we use the semiempirical thermodynamic model developed by Miedema and colleagues [43, 44]. This model was originally developed to model transition metals, but it has successfully been extended to other alloy systems [45–47]. We follow the procedure outlined by de Tandler [45] using the Al–Mo thermodynamic models of Saunders [38]. From the classical approach, we ignore the elastic and structural contributions to the enthalpy of formation of the amorphous phase. We model the Gibbs energy of formation of the amorphous phase ΔG_A as the free energy of mixing of the pure liquid metals ΔG_L plus the atom fraction X_i weighted Gibbs energy of crystallization of the pure undercooled liquid metal $\Delta G_{i,A \rightarrow S}$. This gives

$$\Delta G_A = \Delta G_L + \sum X_i \Delta G_{i,A \rightarrow S} \quad (2.2.1)$$

where the Gibb's energy term is approximated as

$$\Delta G_{i,A \rightarrow S} \simeq \frac{\Delta H_{i,A \rightarrow S}}{T_{m,i}} (T_{m,i} - T) \quad (2.2.2)$$

where $\Delta H_{i,A \rightarrow S}$ is the enthalpy of formation, T is the deposition temperature and $T_{m,i}$ is the melting point of element i . Using Miedema's estimate of the enthalpy of formation [46], we get

$$\frac{\Delta H_{i,A \rightarrow S}}{T_{m,i}} \simeq 3.5 \frac{\text{J}}{\text{mol} \cdot \text{K}} \quad (2.2.3)$$

The calculated Gibbs energies are plotted in Figure 2.2. We can use common tangents between the curves to estimate the phase boundaries. The predicted phase from 0 to 10 at.%Mo is fcc. A two-phase fcc-amorphous region is predicted from 10-15 at.%Mo and a purely amorphous phase from 15 to 55at.%Mo. We also predict a second two-phase region consisting of bcc and amorphous structure from 55-75at.%Mo and at higher Mo concentrations a purely bcc phase. We also note that the phase boundaries are approximate. This is because the atomic layers at the deposition front may be hotter than room temperature [48] and of course the amorphous Gibbs energy calculated here is an approximation. Lastly we point out that the intermetallics omitted from Figure 2.2 are stable by 2 kJ/mol or more at 298 K, and so would be expected to form if the system were brought to equilibrium.

2.2.2 Deposition and Stoichiometries

We have chosen to fabricate Al-Mo thin films by co-sputtering from the pure base materials. This thin film deposition technique is described in more detail in Section 1.3.3. To vary the composition, the power of the Al sputtering gun was kept constant while the Mo gun rate was varied. Deposition rate varies linearly with deposition power. These rates were determined beforehand with a crystal deposition rate monitor [49]. The stoichiometry of an N component

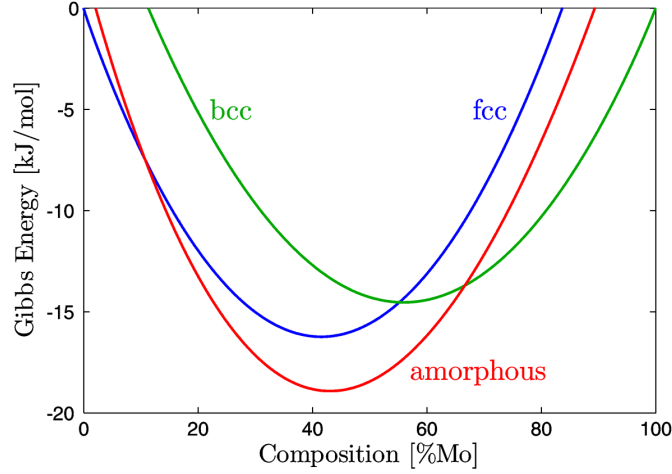


Figure 2.2: Calculated Gibbs energy of fcc, bcc and amorphous Al-Mo phases at 298 K. Crystalline phases were treated as disordered solid solutions and the Miedema approach was used for the amorphous phase.

film is given by

$$X_i = \frac{\rho_i R_i}{\sum_{i=1}^N \rho_i R_i} \quad (2.2.4)$$

where X_i , ρ_i and R_i are the atomic fraction, molar density and deposition rate respectively for component i . In this study, we focus on Al-rich compositions because of the easy integration of Al with microfabrication techniques, due to Al film etching being standardized. We have chosen to deposit films with compositions of 0, 2, 4, 8, 16, 24, 32, 50 and 100 at.%Mo. The film compositions were verified with EDAX. The Al-Mo samples intended for characterization were sputtered at thicknesses of approximately 1 μm . The film thicknesses can be estimated from the sum of the thicknesses of each film component; however, because the density of the deposited film is not known *a priori*, estimates obtained by adding crystalline constituents will typically underestimate the real film thickness. Amorphous films especially tend to have somewhat lower density and thus higher thicknesses than predicted. For this reason, film thickness

was measured after deposition with profilometry when required. Micrographs of some of the deposited Al–Mo compositions are shown in Figure 2.3.

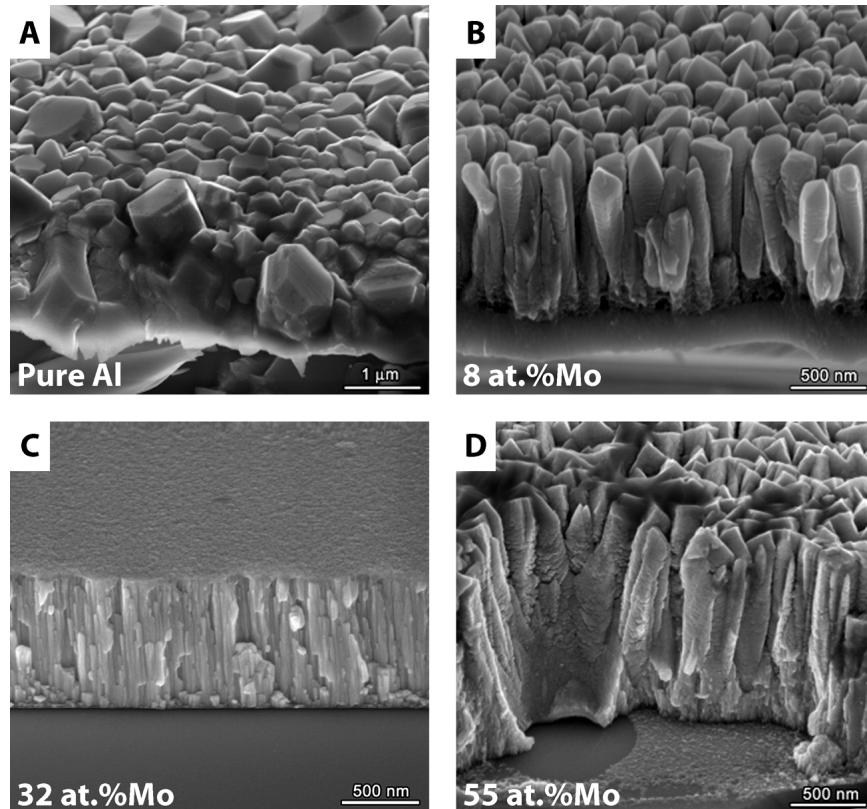


Figure 2.3: SEM micrographs of sputtered Al–Mo films.

In the pure Al films, very large grain structures can be seen. These grains have comparable lateral dimensions to the film thickness. The 8 and 50 at.%Mo compositions have a columnar structure, though with somewhat different surface grain geometries. The 32 at.%Mo film is much smoother than more uniform than the others. However a weak columnar structure can still be observed. This film also appears to be fully dense; porosity was observed in the other compositions of Figure 2.3.

2.3 Results and Discussion

2.3.1 Microstructure

The physical properties of a polycrystalline alloy strongly depend on the phase composition of the alloy. The simplest way to determine the dominant phase composition of a thin film is x-ray diffraction. Figure 2.4 shows several example $\theta/2\theta$ x-ray diffraction patterns for Al–Mo thin films. Compositions below 16at%Mo were identified as crystalline fcc, and compositions above 50at% as crystalline bcc. The dominant feature of all intermediate compositions is an amorphous hump at $\simeq 41^\circ$. Two scans, taken from film compositions of 16at.% and 50at.%Mo, contained both the amorphous hump and crystalline peaks. No other crystal peaks were identified for any composition, validating our above assumption that Al–Mo intermetallics would not form.

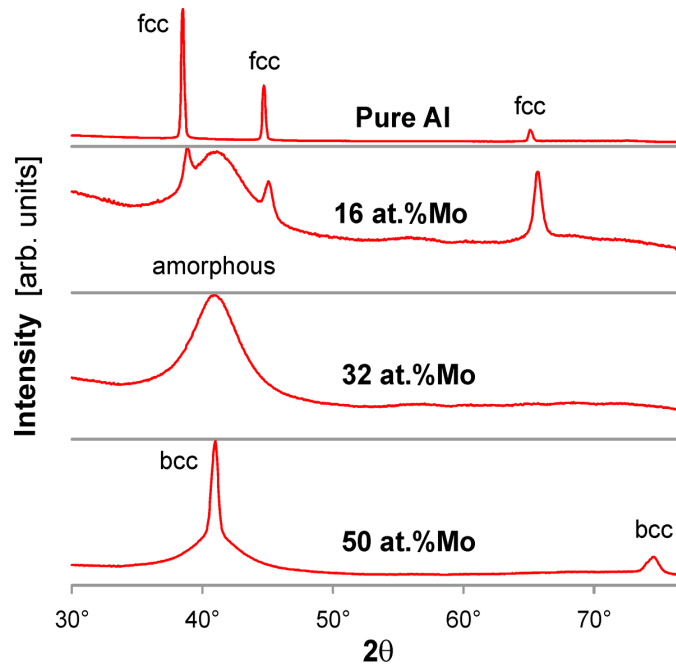


Figure 2.4: X-ray diffraction scans of Al–Mo thin films. Crystalline peaks and an amorphous hump are labeled.

These x-ray scans verify the phases predicted in Figure 2.2. Both the fcc-amorphous and bcc-amorphous two-phase regions are in reality closer to the centre of the phase diagram than predicted. This indicates that we are probably slightly over-estimating the stability of the amorphous phase in our Gibbs energy calculations. Qualitatively however, the predictions are very accurate.

We performed TEM and HRTEM studies for closer examination of the film microstructures. TEM micrograph overviews of the Al–Mo structures are plotted in Figure 2.5. These micrographs display similar trends to those seen in Figure 2.3. The pure Al film has very large grains, whereas smaller grain diameters and a strong columnar morphology are seen in the 8 and 50 at.%Mo films. By contrast, the 32 at.%Mo film is extremely uniform and smooth throughout the thickness. Weakly visible columns can also again be seen in this composition.

Figure 2.6 shows more detailed TEM micrographs and Select Area Diffraction (SAD) patterns of the Al-32at.%Mo thin film. Both amorphous and crystalline regions can be seen in both Figure 2.6(A) and (C). The SAD pattern rings, plotted in Figure 2.6(B) identified these crystalline regions as nanocrystalline bcc. However this TEM study is at odds with the above XRD scans for 32at.%Mo. The most likely reason for this is electron-beam induced crystallization. If the nucleation barrier of a crystalline phase is relatively low, the energy provided by inelastic electron collisions with the lattice can cause crystalline regions to form [50]. Interestingly, the equilibrium crystalline phases, Al_8Mo_3 and AlMo_3 , are not present; instead the crystalline phase formed by the electron beam is bcc. The simpler structure of the disordered bcc phase over the equilibrium intermetallics could explain why its nucleation barrier is lower. Formation of metastable crystalline compounds induced by an electron beam has been observed in the literature, for example in a Ge–Au amorphous alloy [51].

TEM examinations of the Al–Mo two-phase compositions agree much better with the XRD results. Figure 2.7 shows HRTEM micrographs of the 16 at.%

CHAPTER 2: AL-MO ALLOY DESIGN FOR THIN FILM APPLICATIONS

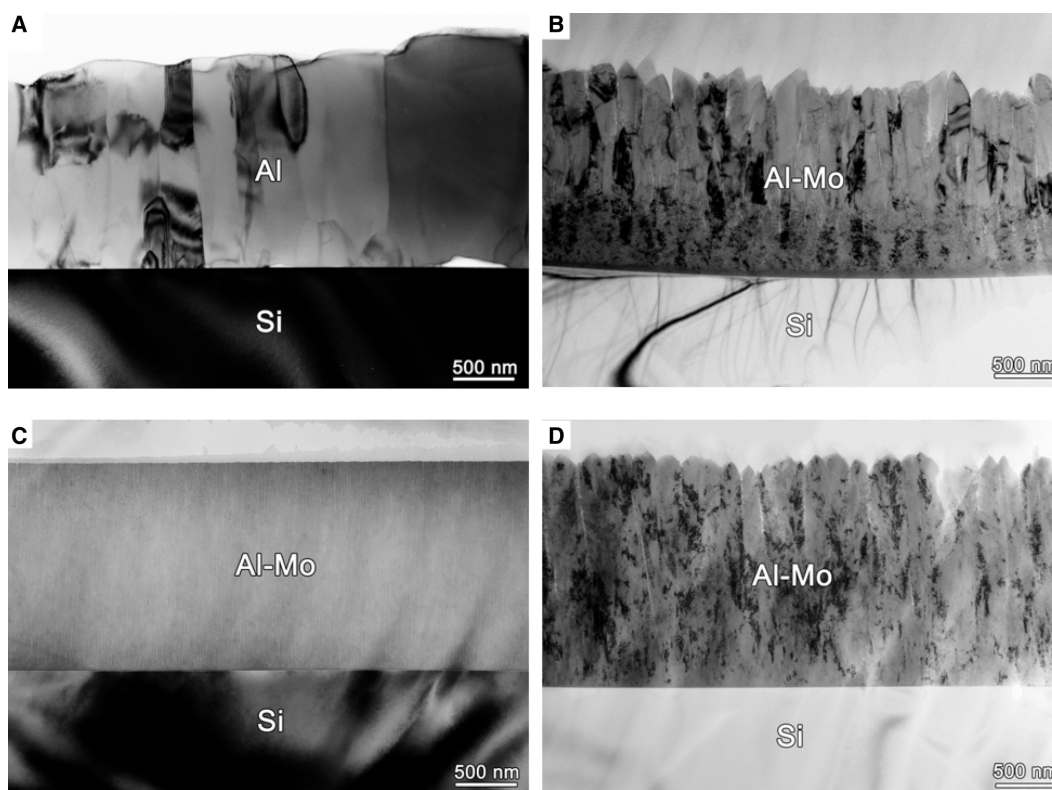


Figure 2.5: Cross-sectional bright-field TEM micrographs of (A) pure Al, (B) Al-8 at.%Mo, (C) Al-32 at.%Mo and (D) Al-50 at.%Mo thin films.

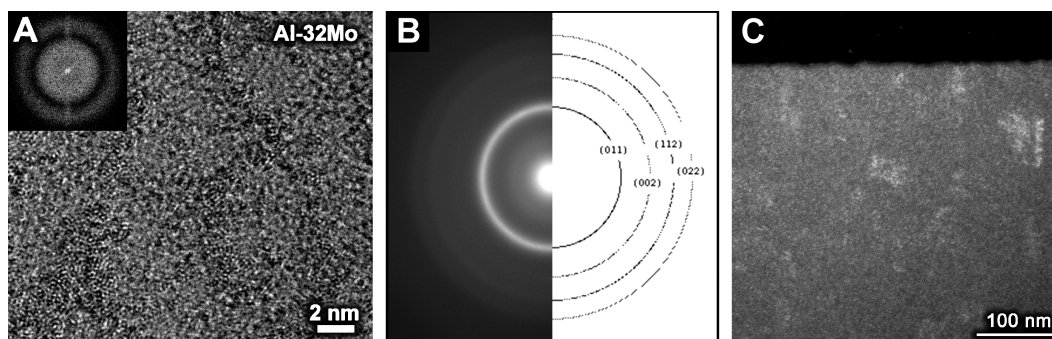


Figure 2.6: TEM micrographs of Al-32at.%Mo: (A) representative HRTEM, (B) SAD and (C) dark-field TEM cross-section taken from innermost ring.

and 50 at.%Mo films. Both film microstructures contain amorphous and crystalline regions. The crystalline regions are quite extensive, perhaps occupying more volume than the XRD scans would suggest. The energy imparted by the electron beam may allow the crystalline regions to expand into the surrounding amorphous matrix [52].

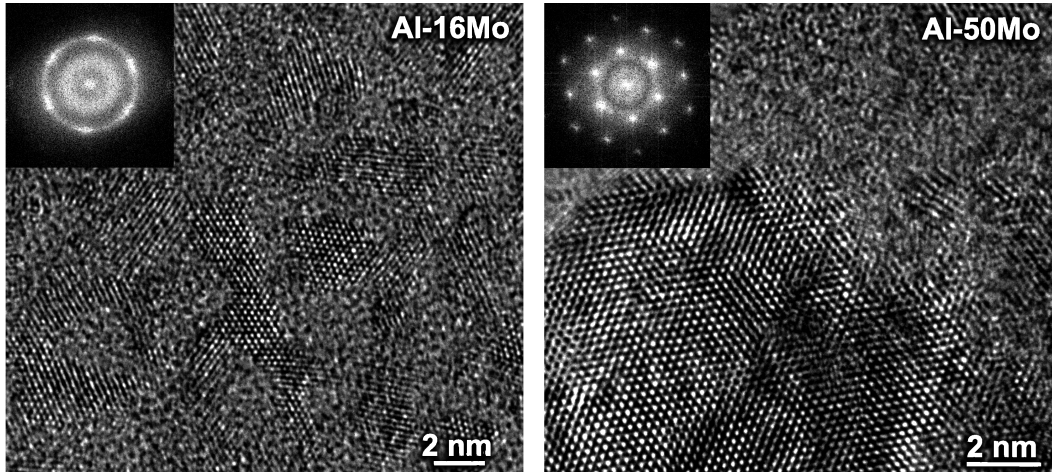


Figure 2.7: HRTEM micrograph of Al-16at.%Mo (left) and Al-50at.%Mo (right), with digital diffractograms inset.

2.3.2 Film Surface

A smooth surface is essential for structural layers of nanoscale resonators for a few reasons. The first reason is that if more layers need to be deposited on top of the resonator layer (eg. electrical wires), a smooth substrate allows subsequent layers to be continuous at lower thicknesses. Smoother surfaces also allow a very thin film to reflect more light [53] and carry more current [54]. Additionally, large grain structures relative to the device geometry can cause undesirable variations in local physical properties. Conversely, smaller grains allow for a more uniform microstructure.

The surface of Al–Mo films were characterized using atomic force microscopy

(AFM). Surface slopemaps are plotted in Figure 2.8. In these images, the angle of the surface in the x - z plane $\theta = \tan^{-1}(\partial z/\partial x)$ is mapped to a greyscale gradient. The pure Al film displays the large grains seen in Figures 2.3 and 2.5. The addition of 8 at.%Mo reduces grain diameter considerably.

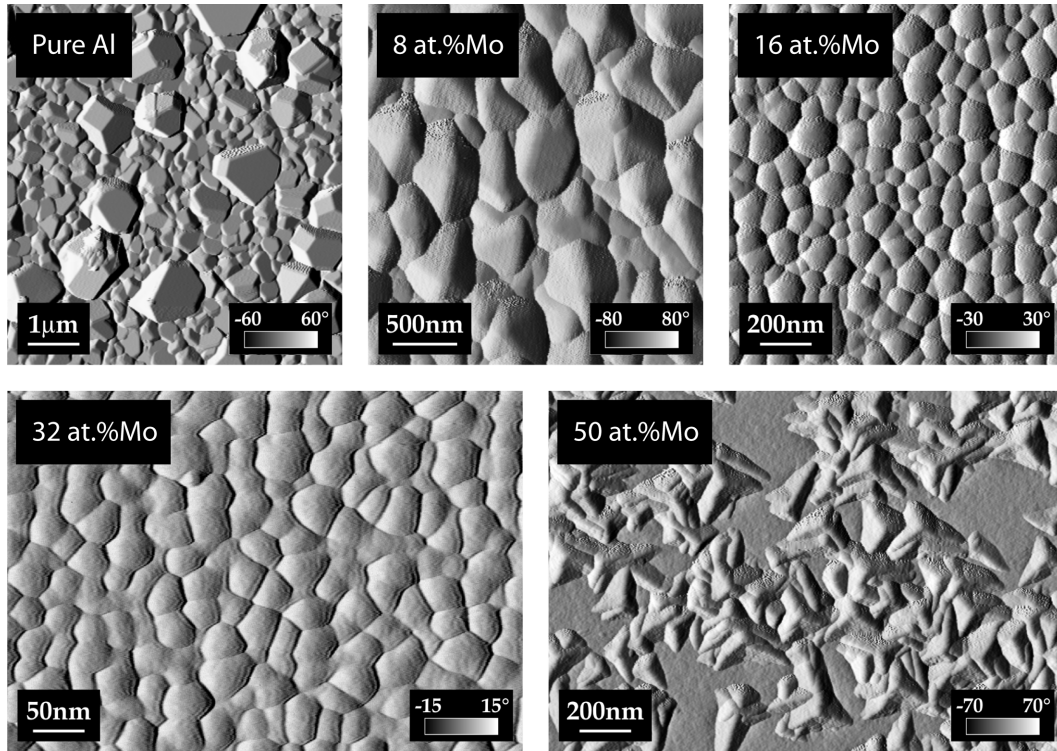


Figure 2.8: Surface slopemaps of Al–Mo films taken from AFM scans. Note the differing scalebar dimensions.

Both the 16 and 32 at.%Mo films display the rounded surface cusps typical of amorphous surfaces [55]. The most interesting surface was observed for 50 at.%Mo film. This surface has two constituents; regions with very fine and smooth amorphous cusps, and rougher regions containing large, triangular bcc grains (the structure is known from the XRD scans in Figure 2.4). In this film, the two phases present are distinctly visible on the surface, whereas only a single surface morphology was observed in the Al-16 at.%Mo film surfaces.

To quantify the structure both out-of- and in-plane, we use two statistical measures. Surface roughness measurements of the AFM height-maps were used to quantifiably compare the out-of-plane structures in Al–Mo films; these are plotted in Figure 2.9.

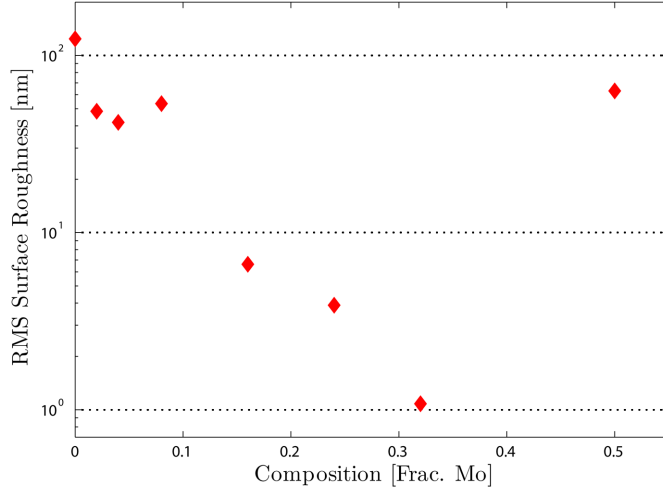


Figure 2.9: Root-mean-square (RMS) surface roughness of Al–Mo films.

The addition of Mo decreases the surface roughness dramatically, reaching a minimum at 32 at.%Mo. The cause of this decrease is two-fold: Initially, Mo refines the grain structure of the parent fcc Al matrix, leading to lower roughness. This geometric effect was shown in more detail in Sections 2.2.2 and 2.3.1, specifically Figures 2.3 and 2.5. At higher Mo concentrations, the microstructure becomes amorphous and the surface roughness decreases further. This is because the surface growth mechanisms of an amorphous film intrinsically lead to lower surface roughnesses than polycrystalline films; amorphous films do not possess the large flat facets characteristic of polycrystalline films [56]. At a composition of 50 at.%Mo, the microstructure is partially polycrystalline and as such the surface roughness once again increases considerably.

The in-plane structure of both crystalline and amorphous surfaces can be

compared by using the height-difference correlation function (HDCF) [57]

$$H(R) = \langle [h(\mathbf{r}) - h(\mathbf{r} + \mathbf{R})]^2 \rangle_{r,R} \quad (2.3.1)$$

where $H(R)$ is the correlation measure at a given distance R and $h(\mathbf{r})$ is the height of the film surface at position \mathbf{r} . Figure 2.10 shows the HDCF of the Al–Mo films shown in Figure 2.8.

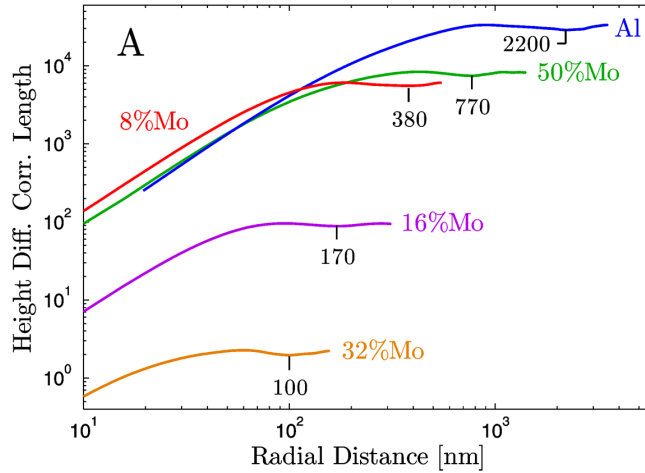


Figure 2.10: Height difference correlation functions of Al–Mo films. Mean correlation length is marked for each composition.

The mean correlation length R_c , which is defined as the first minimum of the HDCF, is a good measure for quantitatively comparing the lateral scale of the film surfaces. The three films in Figure 2.10 with wholly or partially crystalline surface structure (pure Al, 8 and 50 at.%Mo) have considerably larger mean correlation lengths than the remaining two films with amorphous surfaces. For the amorphous films, the mean correlation length decreases with increasing Mo content, reaching a minimum at the Al-32 at.%Mo stoichiometry. The asymptotic value at large distances of the HDCF provides another measure of the surface roughness; this value is $2\sigma^2$, where σ is the RMS surface roughness. Again the films with amorphous surfaces display markedly higher surface roughnesses.

To summarize the surface structure versus composition, a structure zone map (SZM) was constructed by interpolating the AFM scans in Figure 2.3.2, similar to other maps relating the surface and microstructure to pressure and temperature [58]. The Al–Mo composition SZM is shown in Figure 2.11.

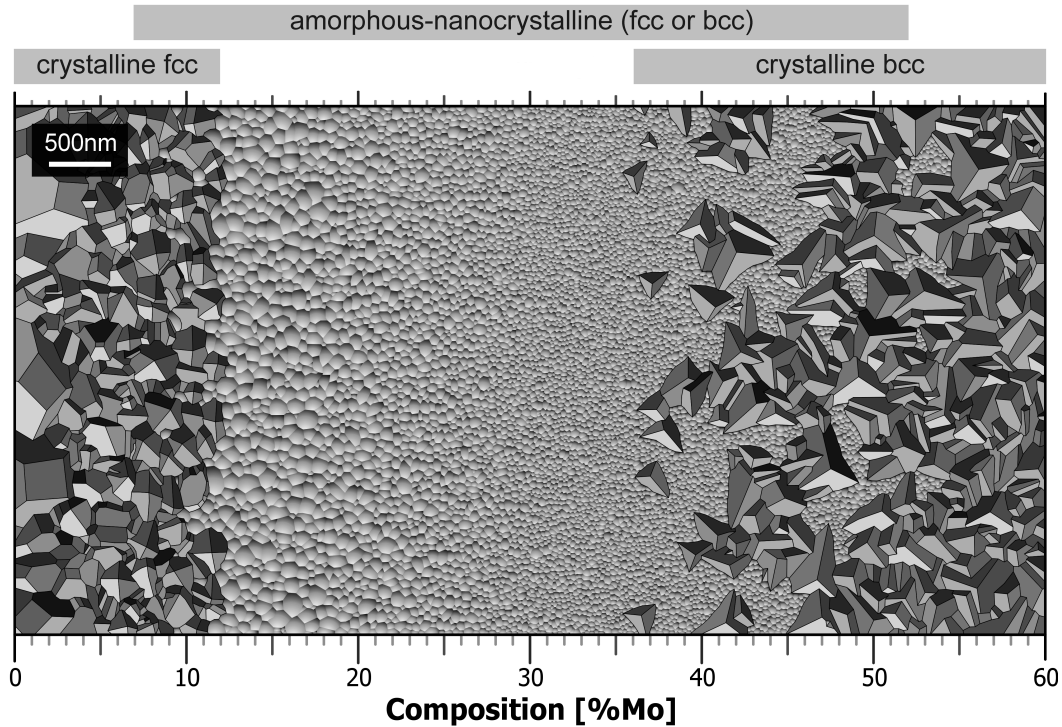


Figure 2.11: Structure zone map describing the surface of Al–Mo thin films.

2.3.3 Physical Properties

How well the Al–Mo alloy functions as a structural material for nanoscale resonators depends heavily on its physical properties. We therefore have measured the conductivity, hardness, modulus and surface roughness of all film compositions. The resistance of various Al–Mo compositions was measured using a 4-point probe, described in more detail in Section 1.4.7. The resistivities calculated from the resistance measurements are plotted in Figure 2.12.

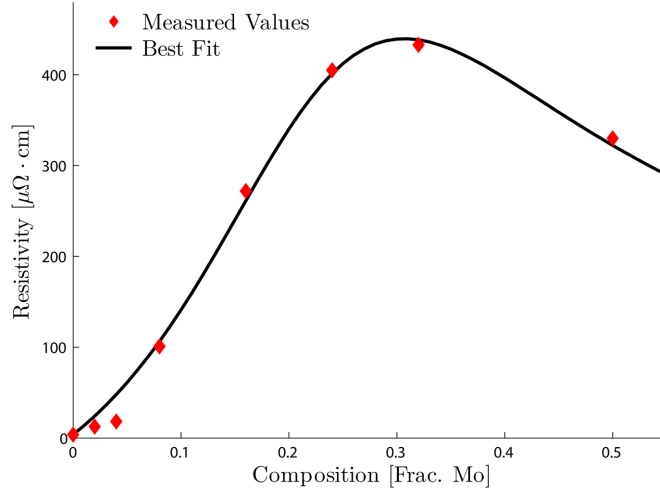


Figure 2.12: Al–Mo Resistivity measurements. Best fit of Equation 2.3.8 also plotted.

The lowest resistivities were measured for pure Al and pure Mo, with the maximum resistivity falling at 32 at.% Mo. These resistivities can be understood by considering the long-wavelength weak electron scattering approximation for a disordered binary alloy as described by Bhatia and Thornton [59]. In this model, the resistivity is given by the weighted dynamic structure factors: the mean square fluctuation in the number of particles $S_{\text{NN}}(0)$ in a volume V , mean square fluctuation in concentration $S_{\text{CC}}(0)$ and correlation between fluctuations in number density and concentration $S_{\text{NC}}(0)$. These structure factors are given by

$$S_{\text{CC}}(0) = Nk_{\text{B}}T / \left(\frac{\partial^2 G^{\text{M}}}{\partial x^2} \right)_{T,P,N} \quad (2.3.2)$$

$$S_{\text{NN}}(0) = \frac{N}{V} k_{\text{B}} T \kappa_{\text{T}} + \delta^2 S_{\text{CC}}(0) \quad (2.3.3)$$

$$S_{\text{NC}}(0) = -\delta S_{\text{CC}}(0) \quad (2.3.4)$$

where N , k_{B} , T , G^{M} and κ_{T} have their standard thermodynamic meanings.

The value δ represents the dilation factor, given by

$$\delta = \frac{\nu_{\text{Al}} - \nu_{\text{Mo}}}{(1-x)\nu_{\text{Al}} + x\nu_{\text{Mo}}} \quad (2.3.5)$$

where x represents the fraction of Mo and ν_{Al} and ν_{Mo} are the molar volumes of Al and Mo respectively. Following the method of Lubber et al. [60], we neglect the dilation factor δ because of the small difference in molar volumes (0.100 and 0.107 mols/cm³ for Al and Mo respectively), and assume that isothermal compressibility κ_{B} follows a rule of mixtures. This assumption gives

$$S_{\text{NN}}(0) = (1-x)\rho_{\text{Al}} + \rho_{\text{Mo}} \quad (2.3.6)$$

where ρ_{Al} and ρ_{Mo} are the resistivities of Al and Mo respectively. Also following [60], we use a sub-regular solution model for the Gibbs energy of mixing

$$\begin{aligned} \Delta G^{\text{M}} &= Nk_{\text{B}}T [x \log x + (1-x) \log (1-x)] \\ &+ Nx(1-x)[A + B(1-2x)] \end{aligned} \quad (2.3.7)$$

where A and B are the sub-regular solution model coefficients. Using Equations 2.3.2–2.3.7, we derive a final expression for the resistivity of Al–Mo films as a function of composition

$$\rho(x) = (1-x)\rho_{\text{Al}} + x\rho_{\text{Mo}} + \frac{\alpha x(1-x)}{1-2x(1-x)[A-3B(1-2x)]/k_{\text{B}}T} \quad (2.3.8)$$

where α is a scaling parameter. The best fit for the resistivity of Al–Mo gives $\alpha = 849 \mu\Omega \cdot \text{cm}$, $A = 0.44 k_{\text{B}}T$ and $B = -0.75 k_{\text{B}}T$. This best fit is shown in Figure 2.12 and the agreement is excellent with the experimental data. The values of A and B are physically reasonable since they are on the order of $k_{\text{B}}T$. The larger value of B than A is what causes the compositional asymmetry of the Al–Mo resistivities in Figure 2.12; for these values of A and B , the excess Gibbs energy of mixing is more negative on the Al-rich compositions.

There are several limitations of this conductivity model applied to the Al–Mo system. This model neglects long wavelength electrons. This means that the

changing mean grain diameters of the polycrystalline structure at low Mo and Al concentrations are not taken into account. Additionally, the parent phase is different between the Al and the Mo-rich sides (fcc and bcc respectively) which could also lead to a system difference in conductivity. The model used here is really only applicable in the compositional regions where either amorphous or highly-disordered solid solution is the dominant phase present.

The simplest way to measure physical strength of a thin film is nanoindentation. A higher hardness is desirable because it makes devices less vulnerable to plastic deformation. A higher elastic modulus raises the resonant frequency of a given resonator geometry, which is desirable for some applications. The results of nanoindentation experiments on Al–Mo films are plotted in Figure 2.13. Each data point is the average value of 25 separate indentations; the standard deviation in hardness is shown as error bars on the plot.

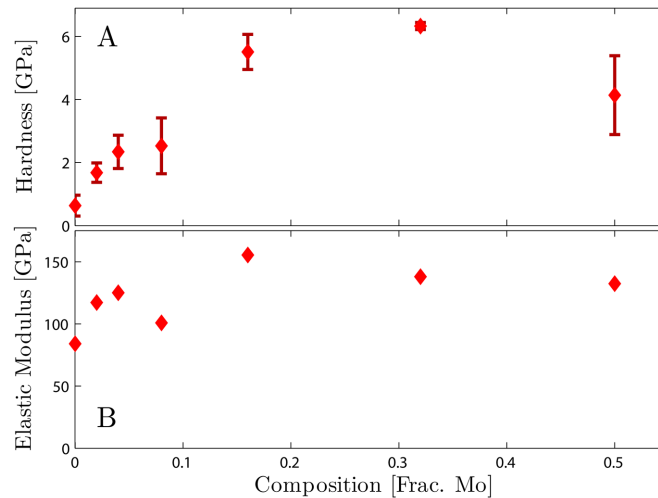


Figure 2.13: Al–Mo nanoindentation measurements. (A) Hardness and (B) elastic modulus.

The addition of Mo to Al raises both the modulus and the hardness, but interestingly this rise is not monotonic. Rather the highest hardness occurs in the 32 at.%Mo film and the highest modulus at 16 at.%Mo. The increase in

hardness is approximately an order of magnitude over pure Al at the maximum. A possible explanation for the large hardness increase is the microstructural shift from crystalline to amorphous in compositions from 16 to 50 at.%Mo.

2.4 Summary

We have now characterized the surface structure, microstructure and physical properties of Al–Mo thin films of various compositions. For our application, nanoscale metal resonators, a composition of Al-32 at.%Mo offers the best combination of the desired properties. This composition has the most uniform microstructure, the smoothest surface structure and the highest hardness. The conductivity is lowest for this composition, but still firmly in the metallic range. The conductivity and reflectivity are high enough for either electrical or optical readout from resonators without any additional surface coating. In the next chapter we describe fabrication and characterization of Al-32 at.%Mo nanoscale resonators.

3

Fabrication of Nanoscale Resonators From Metal Alloys ^{1 2}

3.1 Motivation

The promise of nanotechnology and specifically nanomachines was first explored by Richard Feynman in his famous 1958 lecture titled “There’s Plenty of Room at the Bottom” [61] and expanded upon in a 1983 follow-up called

¹Material in this chapter has been published in:

- ▶ Z Lee, C Ophus, LM Fischer et al. (2006) *Nanotechnology* 17: 3063-3070
- ▶ C Ophus, N Nelson-Fitzpatrick, Z Lee et al. (2008) *Applied Physics Letters* 92: 123108

²The Al–Mo devices presented in this chapter were jointly fabricated and tested by the author and Nathan Nelson-Fitzpatrick of the Evoy group.

“Infinitesimal Machinery” [62]. In these talks, Feynman anticipated our current technological ability to fabricate mechanical structures on the nanoscale. He also proposed several applications that would require mechanical actuation such as microvalves or micromirrors, nanospring arrays to contact various points on microelectronic circuits or even swimming microbots. These talks proved extremely foresighted; for example, nanospring arrays have recently begun to produce scientific studies and technological applications [63–65].

A current application of nanoscale mechanical devices is high-frequency mechanical switches. The reasoning for using nanoscale devices for this application is as follows. Any mechanical system vibrates with an angular frequency w_0 approximately equal to

$$w_0 = \sqrt{\frac{k^*}{m^*}} \quad (3.1.1)$$

where k^* is the effective spring constant and m^* is the effective mass of the resonator. As a device with length l is uniformly scaled down, m^* varies with l^3 , whereas k^* varies with l . This leads to dramatic increases in frequency with decreasing resonator dimensions [26]. That means that mechanical switches can achieve extraordinarily high frequencies. Furthermore, the energy loss of a mechanical resonator per cycle can potentially be far less than an equivalent electronic circuit [66].

A second current application are nanoscale sensors, including chemical, biological and other types. These devices tend to have very simple geometries, with either an electrical or optical method of monitoring the resonance frequency. The device surfaces are chemically functionalized to adsorb a particular element or specific biomarker. When mass is loaded onto the device surface, the frequency changes and detection has been achieved. Again the reasoning for using nanoscale sensors as opposed to larger devices is very simple; the relative mass sensitivity of a device depends on the device’s mass. Since m^* varies with l^3 , shrinking a resonating sensor dramatically increases the sensitivity. The smallest device masses are now on the scale of attograms, and

single molecule detection is now within reach [26].

As discussed in Section 2.1, metals are often coated onto semiconductor devices to improve conductivity or reflectivity. An alternative is to fabricate the entire device from a metal thin film [35]. This negates the problems associated with bilayer devices such as differential stress or increased energy dissipation [30]. In this chapter, we describe fabrication and testing of nanoscale metal resonators from the alloy selected in the previous chapter, Al-32 at.%Mo.

3.2 Experimental Methods

3.2.1 Resonator Fabrication

We have developed a versatile method to create nanoscale patterns from any thin material. To do this, we utilized a lift-off procedure to create the pattern as opposed to using chemical etchants, which are specific to a particular material. The fabrication procedure used in this study is laid out in Figure 3.1, and is described in more detail below.

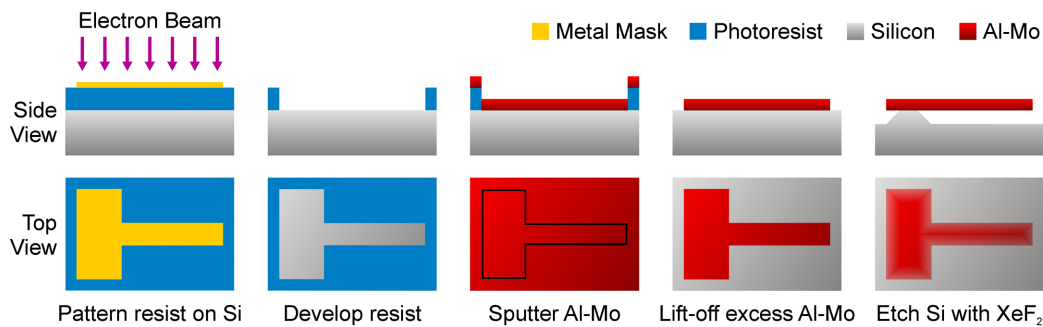


Figure 3.1: Process flow for fabricating nanoscale Al-Mo cantilevers.

Initially, a photoresist composed of poly(methyl methacrylate) (PMMA) in a solvent is spun onto a silicon wafer. A pattern writer is used to write the device

CHAPTER 3: METALLIC NANOSCALE RESONATORS

geometries into the resist using an electron beam, a process known as e-beam lithography. After a chemical development step, bare silicon is exposed in the shape of the desired devices. We then sputter a thin layer of the structural material onto the wafer. The remaining resist is then dissolved in acetone to remove unwanted material. Lastly, the silicon is etched away by exposure to XeF_2 gas in vacuum. Large pads of the structural material remain anchored to the silicon, whereas the smaller devices are undercut and fully released. SEM micrographs of the Al–Mo cantilevers are shown in Figure 3.2.

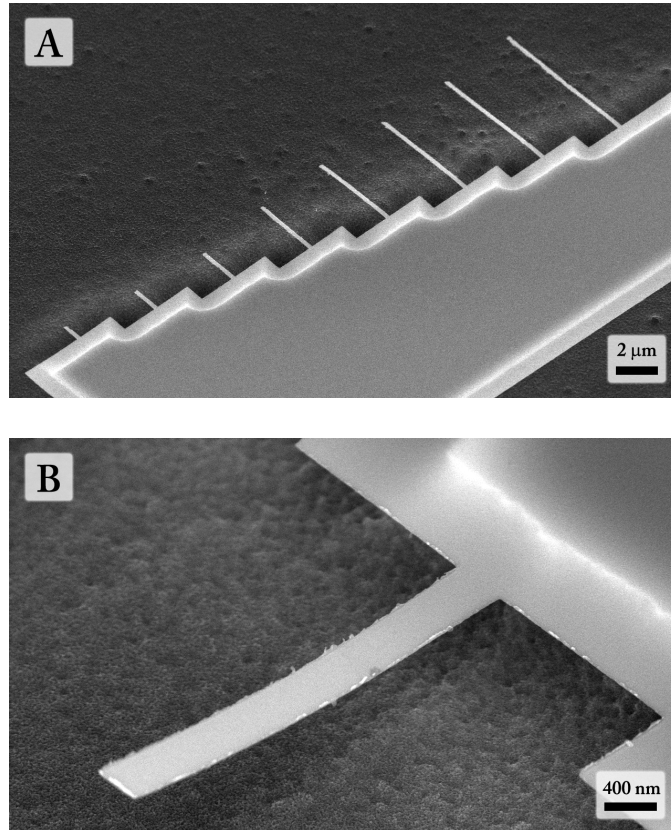


Figure 3.2: (A) Bank of 400 nm wide cantilevers with lengths from 1 to 8 μm fabricated from 20 nm thick Al-32 at.%Mo. (B) Close-up of 8 μm long cantilever.

3.2.2 Cantilever Frequency Response

The simplest geometry for a nanoscale resonator is a cantilever with a rectangular cross-section, i.e. a cuboid clamped perfectly on one edge, free to flex in the z -direction. A schematic of this device is shown in Figure 3.3.

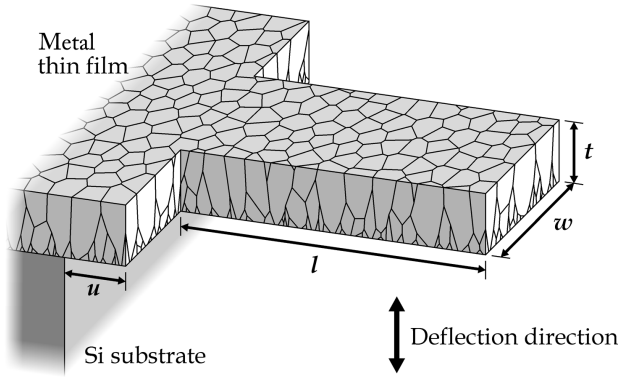


Figure 3.3: A singly-clamped metal resonator.

There are many different natural frequencies of vibration, but for simplicity we will consider only transverse modes in the direction perpendicular to the substrate. The frequency f of the n^{th} transverse mode is given by [67]

$$f_n = \frac{\lambda_n^2}{4\pi\sqrt{3}} \frac{t}{(l+u)^2} \sqrt{\frac{E}{\rho}} \quad (3.2.1)$$

where t and l are the thickness and length of the cantilever respectively, u is the device undercut (how far the device anchor extends beyond the substrate edge), and the square root of the ratio of elastic modulus E to the device density ρ is the speed of sound in the device material. Note that the resonant frequency does not depend on the cantilever width w . The term λ_n is the modal parameter of the n^{th} resonance mode given by positive solutions to the equation [67]

$$\cos(\lambda_n) \cosh(\lambda_n) = -1 \quad (3.2.2)$$

CHAPTER 3: METALLIC NANOSCALE RESONATORS

The first several solutions to Equation 3.2.2 are given in Table 3.1. Unless otherwise stated, all measurements in this study are on the fundamental (0th) transverse mode of resonance.

Table 3.1: Transverse modal parameters of a singly-clamped resonator.

n	λ_n	n	λ_n
0	1.875	3	11.000
1	4.694	4	14.137
2	7.855	5	17.279

At frequencies close to a resonant frequency, the power spectra of the displacements will have Cauchy-Lorentz distribution dependencies on frequency with the peaks falling on the resonance/centre frequencies f_0 . This distribution in the frequency domain of measured intensity I has the form

$$I(f) = \frac{I_0 \Delta f^2}{4(f - f_0)^2 + \Delta f^2} \quad (3.2.3)$$

where Δf is the the full-width-half-maximum (FWHM). If a resonator is being employed as a mass sensor, the minimum detectable mass depends linearly on the quality factor of the device, given by [30]

$$Q = 2\pi \frac{E}{\Delta E} = \frac{f_0}{\Delta f} \quad (3.2.4)$$

where E is the stored vibrational energy and. ΔE is the energy lost during one cycle of vibration. The overall quality factor depends on the quality factors of each possible energy loss mechanism in the following way

$$\frac{1}{Q} = \sum_i \frac{1}{Q_i} \quad (3.2.5)$$

where Q_i is the i^{th} mechanism of energy dissipation. Loss mechanisms that may need to be considered are clamping losses, thermoelastic dissipation, extrinsic molecular flow damping, squeeze film molecular damping, surface losses

and internal friction [68–74]. Polycrystalline metal devices may also experience energy dissipation due to grain boundary sliding or dislocation motion. As device thickness approaches zero, the dominant loss mechanisms are extrinsic molecular flow damping, squeeze film molecular damping and surface damping. We expect surface damping to be the dominant loss mechanism for metal resonators less than 100 nm thick that form a surface oxide. A lengthy discussion on these points is given in [75].

To simplify the fitting procedure in terms of the important figures of merit, we parameterize I in terms of f_0 and Q . Combining Equations 3.2.3 and 3.2.4 gives

$$I(f) = \frac{I_0}{4Q^2(1 - f/f_0)^2 + 1} \quad (3.2.6)$$

Fitting this equation directly to the power spectra measurements of the spectrum analyzer allows us to quickly assess the performance of our devices. An example measurement is shown in Figure 3.4, captured with a spectrum analyzer sweeping through different frequencies.

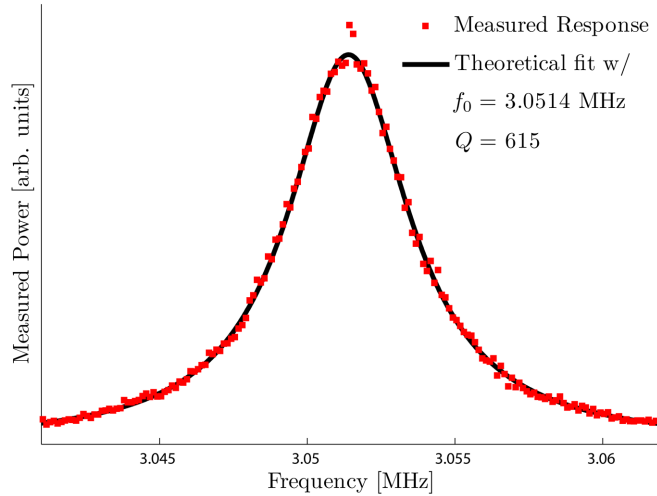


Figure 3.4: Measured power spectrum of a cantilever fabricated from Au–Hf. Best fit of Equation 3.2.6 shown.

3.2.3 Optical Frequency Characterization

There are many possible techniques that can be used to characterize the frequency response of a nanoscale device [28]. The device chip is typically resonated by attaching it to a macroscale piezoelectric resonator. For an electrical readout, the geometric or intrinsic piezoresistive effect can be used to measure the response [76]. Alternatively, capacitive readout can be used to electrically characterize the frequency response of a nanoscale resonator [77]. In this study, we have opted to use optical interferometry to measure the resonator properties of our devices. Optical interferometry has the advantages of not requiring any direct contact to the devices, such as the electrical connections required by piezoelectric sensing. It also has a very wide possible frequency range and can easily probe resonators with very small dimensions [78]. The primary disadvantage is that measurement signal depends heavily on the reflectivity of the devices being used. Our devices, however, are metallic, reflectivity is not an issue. Our measurement setup is depicted in Figure 3.5.

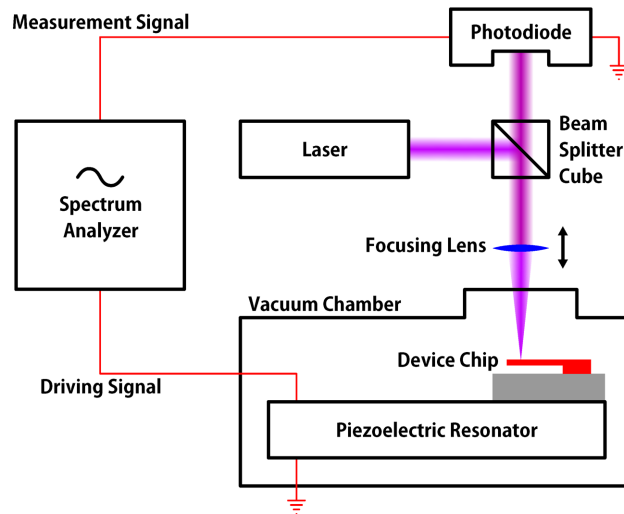


Figure 3.5: Optical interferometer setup for measuring frequency response of nanoscale devices.

In this setup, a laser is directed through a beamsplitter cube and focused onto the surface of a nanoscale resonator placed inside a vacuum chamber. There, the focused laser spot bounces off flat surfaces on the device chip. If the device moves further than the substrate, beams with two different phases are reflected. The interference of these beams modulates the optical signal, and this modulation is detected with a photodiode. The device is resonated by a macroscale piezoelectric resonator, driven by a spectrum analyzer at a given frequency. The spectrum analyzer also measures the output of the photodiode at the driving frequency. Details of this experimental setup are given in [78].

3.3 Results and Discussion

3.3.1 Frequency Measurements

We have resonated a bank of Al-32 at.%Mo cantilevers as a proof of principle for sensor applications from all-metal devices. The measured centre frequencies are plotted in Figure 3.6. The best fit of Equation 3.2.1 is also shown.

The agreement of experiment with theory is excellent for the measurements of Al-Mo device frequency responses. The best fit parameters for our data were an undercut $u = 1.2\mu\text{m}$ and a speed of sound $\sqrt{E/\rho} = 5320$ m/s. The undercut value is in good agreement with the undercut visible in Figure 3.2. The fitted speed of sound falls between those of aluminum and molybdenum which are equal to 5100 and 6190 m/s respectively. If we assume a rule of mixtures for the density of Al-32 at.%Mo, we get $\rho = 5130$ kg/m³. Plugging this value into the best fit speed of sound, we get an estimate for the elastic modulus $E = 145$ GPa. This value is very close to the modulus of 138 GPa measured by nanoindentation in Figure 2.13. The frequency response of the nanoscale Al-Mo resonators matches our expectations.

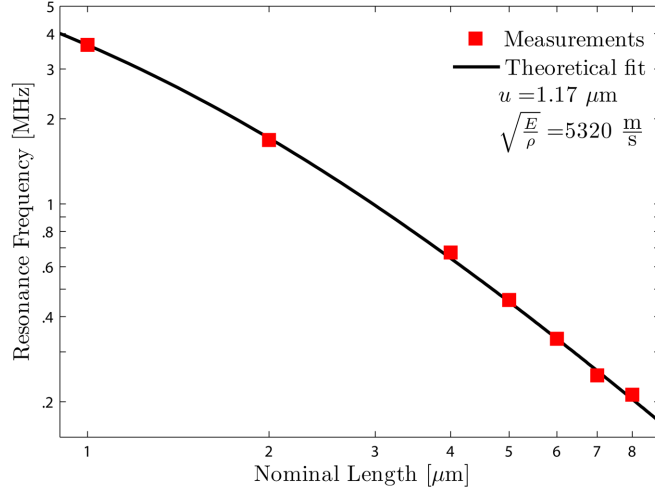


Figure 3.6: Resonant frequencies of Al–Mo devices measured with optical interferometry.

The measured quality factors of the Al–Mo devices are shown in Figure 3.7. The Q values of Al–Mo range from 50 to 500, and appear to rise with increasing frequency. The quality factors of these devices are one to two orders of magnitude lower than those of devices fabricated from semiconductor materials measured in similar experiments [68]. This means that our devices are much less sensitive to changes in mass than semiconductor devices of similar geometries.

The most likely reason for the increased energy dissipation in our devices is a surface oxide. Pure aluminum structures will naturally form an oxide on their surfaces when exposed to air with a thickness of 10 to 28 Å[79]. Since our devices are only 20 nm thick, the surface oxide on the top and bottom constitutes a considerable volume fraction of the resonator, perhaps as high as a quarter. Yasumura et al. estimate the quality factor of a nanoscale resonator with a surface layer of thickness δ as [68]

$$Q_{\text{surface}} = \frac{t}{6\delta} \frac{E}{E_2^S} \quad (3.3.1)$$

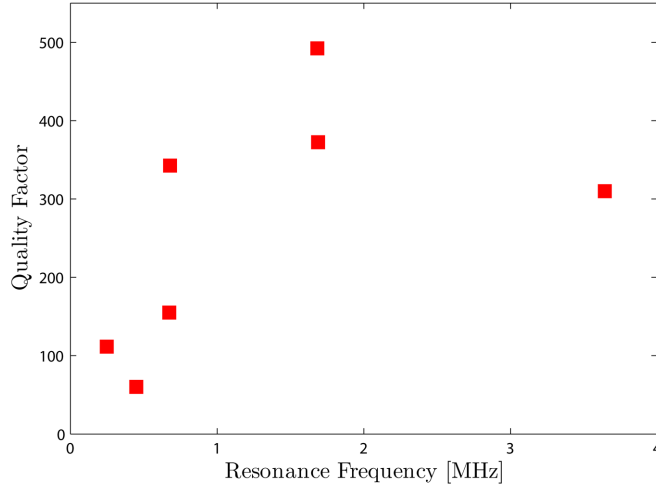


Figure 3.7: Quality factors of Al–Mo devices measured with optical interferometry.

where E is the elastic modulus of the cantilever and E_2^S is the loss modulus of the surface layer. Measurements of the elastic and loss moduli of alumina have been performed by Wolfenden [73] and Fukuhara and Yamauchi [74]. These measurements give an upper bound of 405 MPa for the loss modulus of alumina. If we assume the total device oxide thickness is 4 nm (estimated from cross-sectional HRTEM micrographs [75]), and use our measured elastic modulus of 138 GPa we can estimate $Q_{\text{surface}} \simeq 284$. This estimation is the correct order of magnitude to agree with our Q measurements. The frequency dependence of Q may parallel the frequency dependence of the loss modulus of alumina; further experiments are necessary to confirm this hypothesis.

3.4 Summary

We have fabricated Al–Mo nanoscale resonators as proof of principle for all-metal sensor applications. The measured resonance frequencies of our devices agree very well with mechanical beam theory. These devices perform ade-

CHAPTER 3: METALLIC NANOSCALE RESONATORS

quately with no additional coating layer required to boost the reflectivity of the surfaces. The surface roughness of our devices is also extremely low. The quality factors however range from 50 to 500, lower than comparable devices fabricated from semiconductor films.

4

Derivation of a Geometric Model For Polycrystalline Thin Film Growth ¹

4.1 Motivation

Polycrystalline thin films are important for a wide array of applications including optics, semiconductors, nanomechanical devices and sensors. In addition to variations in bulk material properties, the behaviour of polycrystalline materials is strongly influenced by grain morphology [10] and texture [80]. For example, grain structure can influence thin film stresses and etching [81, 82],

¹A version of this chapter has been published in:

► C Ophus, EJ Lubber and D Mitlin (2010) *Physical Review E* 81: 011601

CHAPTER 4: POLYCRYSTALLINE FILM GROWTH MODEL

sensitivity and response time of sensors [83], thermal conductivity and surface roughness [84] and semiconductor electrical properties [6, 85]. For these reasons it is critical to understand the fundamental processes that govern grain evolution during thin film growth.

Polycrystalline films typically begin as a series of unconnected grains distributed randomly over the substrate surface. The grains expand until they form a continuous film at which point competitive grain growth begins, as originally envisioned by Kolmogorov [86] and van der Drift [87]. Each grain asymptotically evolves towards a kinetic Wulff shape and those grains having more favourable orientations will eventually dominate the surface. If the Schwoebel barrier(s) of one or more low-index crystalline faces is very low, the grain will be extremely faceted and its kinetic Wulff shape will be a simple polyhedron. In the simplest form of faceted polycrystalline thin film growth, the growth velocity of a given facet depends only on its crystallographic orientation.

This type of evolution has been simulated in several recent studies [25, 88–90]. It is also now possible to carefully analyze various aspects of polycrystalline growth both after deposition [91, 92] and *in-situ* [93]. However, few analytic models are available to analyze faceted polycrystalline growth. The most widely-used model was proposed by Thijssen et al. in 1992 [94], but this model is only applicable during late-stage growth.

In this chapter, an analytic model is derived that describes the evolution of a polycrystalline thin film. Like Thijssen, we assume grains can be described geometrically by cones, a comparison elucidated in [90], and construct a model based on the evolution of the angular distribution of cones. However, unlike Thijssen’s model, my method is applicable for all times and can be used to describe a larger variety of initial angular distributions.

4.2 Analytic Growth Model

4.2.1 Initial angular distributions

A conic grain is described with four parameters: the origin in the substrate plane given by coordinates (x_0, y_0) and the primary vector of the cone given by the tilt angle from the substrate normal θ and the angle in the substrate plane ϕ . We make the mean-field-type assumption to ignore the local coordinates of all grains as well as assuming that the distribution of angles ϕ is uniform at all times. Therefore we need only consider the evolution of the angular density distribution $\rho(\theta)$. Three examples of an angular distribution are shown in Figure 4.1.

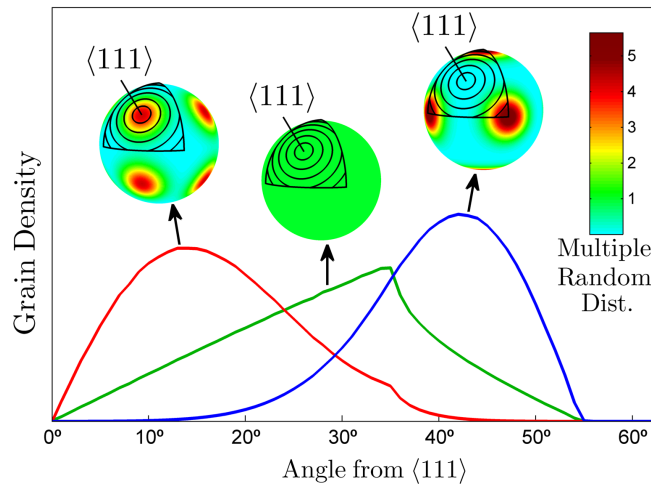


Figure 4.1: Initial grain orientations distributions from left to right: biased towards fastest growth direction, uniform and biased away from fastest growth direction. Fastest growth direction and rings showing the direction of integration are plotted on each spherical pole figure.

In a real crystal system, the *fastest growth direction* refers to the most favourable crystallographic orientation(s) of a grain. For conic grains, the fastest growth

direction is the vector from the cone origin to its apex. In this study, we arbitrarily set the fastest growth directions to the 8 $\langle 111 \rangle$ -directions; these directions are often observed experimentally in fiber texture films. The simplest initial angular distribution of grains would be a uniform distribution. However, grains will often preferentially nucleate closer to a particular orientation. If this orientation is the same as the fastest growth direction, we refer to the angular distribution as being *biased towards* the fastest growth direction. If however the two orientations are different, we call the angular distribution *biased away* from the fastest growth direction. These three cases are shown as spherical pole figures in Figure 4.1; the leftmost case is a primarily $\langle 111 \rangle$ -oriented initial texture (biased-towards), the center case is a uniform initial texture and lastly the rightmost case is a primarily $\langle 001 \rangle$ -oriented texture (biased-away). A $\langle 111 \rangle$ -direction is shown for reference on each of the plots. In all three cases, the angular grain density as a function of θ (the angle from the nearest fastest growth direction) is calculated by radially integrating around one of the $\langle 111 \rangle$ directions, the results of which are also graphed in Figure 4.1. The mathematical details of our construction of initial angular distributions is left to Appendix A.1.

4.2.2 Model Derivation

The analytic model derived here describes the evolution of the angular distribution of grains as the film surface advances. Suppose we have an ensemble of cones with apex angle α and angular density distribution $\rho(\theta, t)$. All conic grains will grow at the same velocity, and for convenience we set the distance from each cone origin to its apex to the growth time t . The advancing surface is composed of grains competing for height, with more favorably oriented grains subsuming those less favorably oriented. To describe the evolution of the surface with time, we must calculate the rate at which all cones are *deleted* by their neighbors.

First consider two cones having tilt angles $\theta' < \theta$. For convenience we will label the taller cone as cone θ' and the shorter cone as cone θ . Figure 4.2 shows a deletion event (a cone apex being subsumed by another cone) occurring between time t and $t + \Delta t$. A *deletion plane* is defined parallel to the substrate at the height of the shorter cone's apex. This is the plane in which the shorter cone's apex collides with the surface of the taller cone.

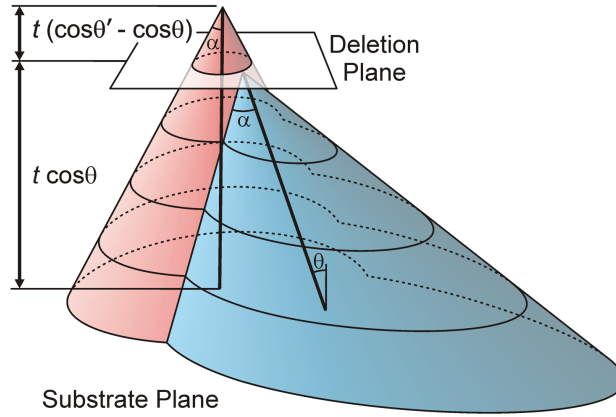


Figure 4.2: A deletion event between two conic grains at time t in the time interval Δt . Isocontours are shown at different heights. Note that the primary axis of both cones are the same length.

Geometric considerations dictate that a cone can only ever be deleted by a cone with a more favourable orientation. In order to calculate the probability of this event occurring, we analyze the geometry of the conic section formed by the intersection between the deletion plane and the taller cone. Figure 4.3 shows the geometry of the conic section in the deletion plane. Two different boundaries are shown, the boundary of cone θ' at time t before the deletion event and at time $t + \Delta t$ after the deletion event. The area between these two boundaries defines the deletion area A_{del} . The probability of cone θ' deleting cone θ in any given time interval Δt is simply the area A_{del} divided by the total possible area where the apex of cone θ can be found in.

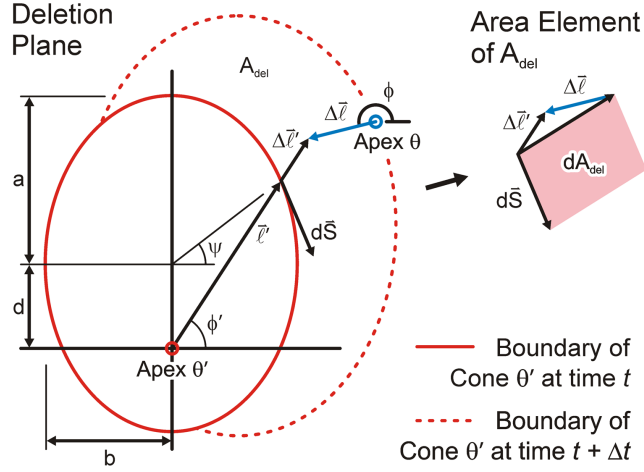


Figure 4.3: Geometry of a cross-section of the cone with tilt angle θ' in the deletion plane shown in Figure 4.2.

To calculate A_{del} , we start with the height difference between the two cone apices, $(\cos \theta' - \cos \theta) t$. The major and minor semiaxes a and b , and the distance d from the ellipse centre to the apex of cone θ' are all proportional to this height difference and are given by

$$a = \frac{\tan \alpha}{1 - \epsilon^2} (\cos \theta' - \cos \theta) t \quad (4.2.1)$$

$$b = \frac{\tan \alpha}{\sqrt{1 - \epsilon^2}} (\cos \theta' - \cos \theta) t \quad (4.2.2)$$

$$d = \frac{\tan^2 \alpha \tan \theta'}{1 - \epsilon^2} (\cos \theta' - \cos \theta) t \quad (4.2.3)$$

where $\epsilon = \sin \theta' / \cos \alpha$ is the eccentricity of the ellipse. Over one time step Δt , the boundary of cone θ' will expand and the apex of cone θ will travel relative to it. The distance $\Delta \mathbf{L}'$ traveled by the elliptic boundary and the distance $\Delta \mathbf{L}$ traveled by the apex of cone θ in the time interval Δt are given by

$$\Delta \mathbf{L}' = \Delta t \frac{\tan \alpha}{1 - \epsilon^2} (\cos \theta' - \cos \theta) [\cos \phi', \sin \phi'] \quad (4.2.4)$$

$$\Delta \mathbf{L} = \Delta t \sin(\theta) [\cos \phi, \sin \phi] \quad (4.2.5)$$

where the direction of these vectors are given by the angles ϕ' and ϕ respec-

tively. If the boundary is parametrized by $x = b \cos \psi$ and $y = d + a \sin \psi$ where $-\pi < \psi < \pi$ then the arc length segment $d\mathbf{S}$ and $\Delta\mathbf{L}'$ can be written as

$$d\mathbf{S} = d\psi [b \sin \psi', -a \cos \psi'] \quad (4.2.6)$$

$$\Delta\mathbf{L}' = \frac{\Delta t}{t} (\cos \theta' - \cos \theta) [b \cos \psi, d + a \sin \psi] \quad (4.2.7)$$

As shown in Figure 4.3 the differential deletion zone is a parallelogram having an area dA_{del} given by

$$\begin{aligned} dA_{del} = & [\sin \theta (a \cos \psi \cos \phi + b \sin \psi \sin \phi) \\ & + \frac{b}{t} (a + d \sin \psi)] \Delta t d\psi \end{aligned} \quad (4.2.8)$$

Because ψ varies from $-\pi$ to π we can introduce an arbitrary phase shift and rewrite Eq. 4.2.8 as

$$\begin{aligned} dA_{del} = & [\sin \theta \cos \phi \sqrt{a^2 \cos^2 \psi + b^2 \sin^2 \psi} \\ & + \frac{b}{t} (a + d \sin \psi)] \Delta t d\psi \end{aligned} \quad (4.2.9)$$

To find the total deletion area A_{del} we must integrate over ψ and average over all ϕ where $dA_{del} > 0$ giving

$$\begin{aligned} A_{del} = \frac{2\Delta t}{\pi} \int_{-\pi/2}^{\pi/2} \int_0^{\cos^{-1} w} & \left[\sin \theta \cos \phi \sqrt{a^2 \cos^2 \psi + b^2 \sin^2 \psi} \right. \\ & \left. + \frac{b}{t} (a + d \sin \psi) \right] d\phi d\psi \end{aligned} \quad (4.2.10)$$

where

$$w = -\frac{b(a + d \sin \psi)}{t \sin \theta \sqrt{a^2 \cos^2 \psi + b^2 \sin^2 \psi}} \quad (4.2.11)$$

Integrating in ϕ we obtain the expression

$$\begin{aligned} A_{del} = \frac{2\Delta t}{\pi} \int_{-\pi/2}^{\pi/2} & \left[\sin \theta \sqrt{1 - w^2} \sqrt{a^2 \cos^2 \psi + b^2 \sin^2 \psi} \right. \\ & \left. + \cos^{-1}(w) \frac{b}{t} (a + d \sin \psi) \right] d\psi \end{aligned} \quad (4.2.12)$$

This equation is numerically evaluated for all values of θ and θ' of interest for a given value of α . To evolve the angular density distribution $\rho(\theta, t)$ over all time, we weight the area of deletion by the angular density distribution to calculate the probability of deletion for each value of θ in the time interval Δt . The new density distribution after this time interval can be calculated by multiplying the old distribution by the survival probability, equal to one minus the probability of deletion, i.e.

$$\frac{\rho(\theta)|_{t+\Delta t}}{\rho(\theta)|_t} = 1 - \int_0^\theta A_{del}(\theta, \theta', \alpha) \rho(\theta')|_t d\theta' \quad (4.2.13)$$

Note that the upper bound of the integral is θ , reflecting the physical rule that a cone can only be deleted by a cone with a more favourable orientation (one with a lower θ value). To calculate the evolution of an angular distribution function, Eq. 4.2.12 is solved first for all θ and θ' values of interest and then that data is used to evolve the distribution using Eq. 4.2.13.

4.3 Model Validation

4.3.1 2+1D Simulation of Conic Grains

To test the analytic model given by Equations 4.2.1–4.2.3 and 4.2.11–4.2.13 we have used level set simulations of competitive conic grain growth. The conic surface of each grain is described by a four-dimensional implicit function. At each time step all surfaces are advanced and a 2+1 dimensional surface $z(x, y)$ is calculated from the union of all cones. When a cone apex is subsumed into the surface, the cone ceases to grow. An example simulation is shown in Figure 4.4 of cones with $\alpha = 30^\circ$ and a uniform distribution of tilt angles up to a cutoff of $\theta_c = 45^\circ$. More details on the simulation methodology are given in [25, 90].

The mean heights of the simulation surfaces shown in Figure 4.4 are given

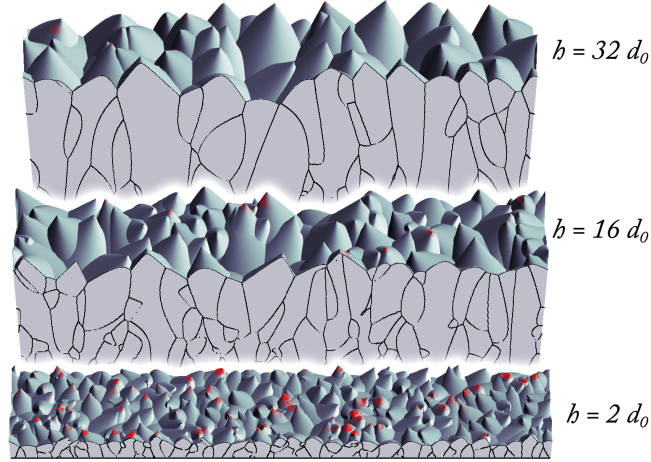


Figure 4.4: Examples of competitive conic grain growth from level set simulations at various thicknesses. Surfaces are shaded by x-direction slope and cross-sectional slices also shown. Potential deletion zones marked in red.

in units of initial grain spacing d_0 , defined as the square root of mean initial grain area A_0 for convenience. Survival probability P is measured by dividing the number of surviving grains by the number of initial grains. Figure 4.4 clearly shows that P decreases monotonically with film thickness h . Note that mean thickness is asymptoting towards time (defined as the length of the primary vector of each cone) which approximately follows the relationship $h = t - 1/2 \tan \alpha \sqrt{P}$.

4.3.2 Comparison of Model to Simulation

A comparison of grain orientation distributions between level set simulations of 10^6 cones and the analytic model, with both having $\alpha = 30^\circ$, is shown in Figure 4.5 for the three cases described in Figure 4.1. The agreement is excellent over all times, validating the analytic model.

It is important to point out that no mean-field assumptions were used in the

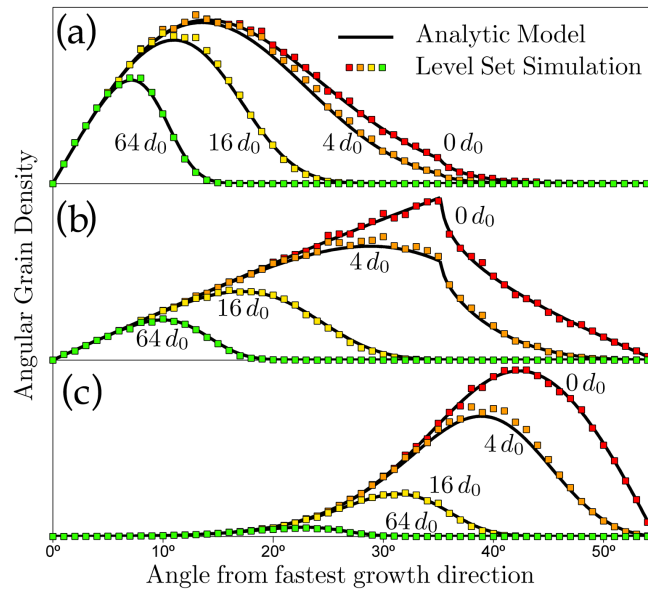


Figure 4.5: Comparison of the grain distribution at four different film thicknesses between analytic growth model and level set simulation for the cases where the initial distribution is (a) biased towards the fastest growth direction, (b) uniform and (c) biased away from the fastest growth direction.

level set simulations. Because the simulation and the model agree, our decision to neglect local grain correlations in the analytic model is validated. Even if local angular or positional correlations of grains do occur, they do not affect the global evolution of the surface in any meaningful way.

4.4 Analysis of Grain Growth Model

4.4.1 Self-Similarity of Distributions

The angular distributions shown in Figure 4.5 display remarkable self-similarity between different thicknesses. Thijssen et al. suggested that $\log(\rho(\theta, t)/\theta) \propto t^2\theta^5$ in late-stage film growth [94]. We derive an exact expression for the asymptotic angular distribution as follows. Each of the angular distributions seen in Figure 4.5 asymptotically approaches a constant slope

$$\eta = \left. \frac{\partial \rho}{\partial \theta} \right|_{\theta \rightarrow 0} \quad (4.4.1)$$

This slope is proportional to the number of grains initially oriented in the fastest growth direction. Note that this value must be estimated or measured experimentally for a given initial angular distribution. The asymptotic form of the angular distribution is given by

$$\rho(\theta, t) = \eta \theta \exp \left[-k \left(\frac{t}{\tau} \right)^2 \theta^5 \right] \quad (4.4.2)$$

where k is a scaling constant and τ is the cross-over thickness into late-stage, or self-similar behaviour. To solve for k , we note that the grain probability of survival is unity at $t = \tau$. Integrating Eq. 4.4.2 from 0 to ∞ when $t = \tau$ gives $k = \left(\eta \Gamma(\frac{2}{5})/5 \right)^{5/2}$ where Γ is the gamma function. The angular distribution at late times is therefore

$$\rho(\theta, t) = \eta \theta \exp \left[- \left(\frac{\eta \Gamma(\frac{2}{5})}{5} \right)^{5/2} \left(\frac{t}{\tau} \right)^2 \theta^5 \right] \quad (4.4.3)$$

which agrees with distributions generated by both numerical iteration of Eq. 4.2.13 and level set simulations.

4.4.2 Scaling Laws

The goal of our analytic growth model is to predict morphological statistics for this type of polycrystalline film growth. Most statistical measures in thin film growth follow power laws with thickness (or equivalently time, for constant deposition rate). Survival probability P is calculated by integrating the angular density distribution

$$P(t) = \int_0^{\pi/2} \rho(\theta, t) d\theta \quad (4.4.4)$$

Inserting Eq. 4.4.3 into Eq. 4.4.4 gives

$$P = (t/\tau)^{-4/5} \quad (4.4.5)$$

Other growth statistics such as expectation value of grain area $\langle A \rangle$ and the root-mean-square (RMS) surface roughness σ have simple relationships to the grain survival probability, the derivations of which are given in the appendix of [90]. From our model we have calculated scaling laws for $\langle A \rangle$ and σ at late-stage growth of

$$\langle A \rangle = (t/\tau)^{4/5} \quad (4.4.6)$$

$$\sigma = \frac{1}{\tan \alpha} \sqrt{\frac{1}{\pi} - \frac{1}{4}} (t/\tau)^{2/5} \quad (4.4.7)$$

Our calculated exponents match those predicted by Thijssen for late-stage growth [94]. However, our model can also predict the value of crossover thickness τ , based only on the cone angle α and the asymptotic value of the slope of the distribution at small angles η . This is achieved by expanding both sides of Eq. 4.2.13 and using the small angle approximation for all θ and θ' terms. Note that in late-stage growth only the first term in Eq. 4.2.12 needs to be

considered.

$$\begin{aligned}
 \frac{e^{-\left(\frac{\eta\Gamma(\frac{2}{5})}{5}\right)^{5/2}\left(\frac{t+\Delta t}{\tau}\right)^2\theta^5}}{e^{-\left(\frac{\eta\Gamma(\frac{2}{5})}{5}\right)^{5/2}\left(\frac{t}{\tau}\right)^2\theta^5}} &= 1 - 2\Delta t\eta \int_0^\theta a \sin \theta\theta' d\theta' \\
 1 - \left(\frac{\eta\Gamma(\frac{2}{5})}{5}\right)^{5/2} \frac{2t\Delta t}{\tau^2} \theta^5 &= 1 - t\Delta t\eta \tan \alpha \frac{\theta^5}{4} \\
 \tau = \sqrt{8} \left(\frac{\Gamma(\frac{2}{5})}{5}\right)^{5/4} \frac{\eta^{3/4}}{\sqrt{\tan \alpha}} & \quad (4.4.8)
 \end{aligned}$$

Noting that the coefficient of Eq. 4.4.8 is approximately unity gives

$$\tau = \frac{\eta^{3/4}}{\sqrt{\tan \alpha}} \quad (4.4.9)$$

Eq. 4.4.9 was confirmed by comparing its predictions to the crossover thicknesses observed in the analytic model for many values of α and η .

4.4.3 The Effect of Non-Uniform Initial Distributions

We now analyze the effect that biasing the initial growth direction towards or away from the fastest growth direction has on the growth statistics. Figure 4.6 shows RMS surface roughness and probability of grain survival versus film thickness for the three cases described above. All three cases asymptotically approach the expected power laws as $t \rightarrow \infty$. However, biasing the initial grain distribution towards the fastest growth direction delays deletion of grains, leading to longer survival times. In this case the surface is much smoother because the mean peak to peak distances are dramatically reduced. Biasing the growth direction away from the fastest growth direction has the opposite effect on both statistical measures. These effects manifest in the thickness range from roughly $1 < h < 1000 d_0$.

Interestingly, the studies performed in [91, 95] found power law exponents for roughness and grain diameter in excess of the predicted value of 0.4. This

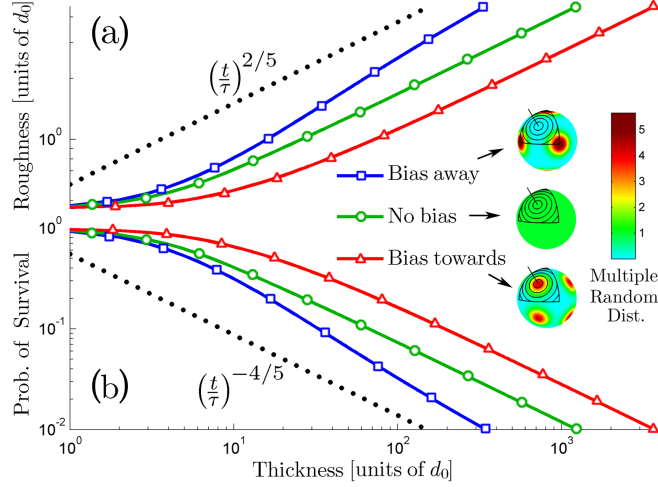


Figure 4.6: (a) RMS surface roughness and (b) probability of grain survival calculated from the analytic growth model for the three cases described in Figure 4.1. Power laws are shown in both graphs as dotted lines.

study suggests that an initial nucleation of grains with texture biased away from the fastest growth direction could be responsible for the observed power law deviations. And indeed, an initial texture bias towards $\langle 001 \rangle$ was observed in those studies compared to a fastest grain growth direction near $\langle 111 \rangle$. To confirm our explanation, careful measurements of the initial grain angular distributions will be required.

4.5 Summary

To conclude, I have derived an analytic model for polycrystalline grain growth based on conic grain geometries. This model showed excellent agreement compared to level set simulations of conic surfaces and the results can be computed in a much shorter timespan. Three initial angular grain density distributions were analyzed. When the distribution was biased towards the fastest growth direction, the probability of survival for each grain is increased and the surface

CHAPTER 4: POLYCRYSTALLINE FILM GROWTH MODEL

roughness is decreased compared to a uniform initial distribution. When the distribution is biased away from the growth direction, the opposite trends are observed. These results underscore the importance of the initial grain distribution when analyzing polycrystalline thin film growth. Finally, the cross-over thickness into late-stage growth is predicted with a simple analytic expression.

5

Computer Simulations of Polycrystalline Thin Film Growth ¹

5.1 Motivation

Thin film deposition is an important component of many fields of science and technology. The possible microstructures of a thin film are single crystal, polycrystalline and amorphous. Among these microstructures, polycrystalline show the highest deviation of physical properties amid different samples of a

¹Material in this chapter has been published in:

► C Ophus, EJ Lubber and D Mitlin (2009) *Acta Materialia* 57: 1327-1336

single composition. This is because the grain shape, size and orientation in the thin film can strongly affect hardness, surface roughness, wear and corrosion resistance, electrical conductivity and optical properties [4]. There is therefore a strong motivation to understand what deposition and material considerations influence the morphology of polycrystalline thin films.

Polycrystalline thin films can be fabricated in a variety of ways including thermal evaporation, sputtering, molecular beam epitaxy (MBE), chemical vapor deposition (CVD), pulsed laser deposition (PLD) and others. These polycrystalline films are typically characterized by a columnar morphology parallel to the growth direction, with strongly faceted grain surfaces. The simplest form of growth arises from situations where the growth velocity at any point on a grain surface depends only on the crystallographic orientation of the facet it is on. This type of growth was first described by Kolmogorov [86] and then by van der Drift [87]. Several researchers have simulated this type of thin film growth in two dimensions [11, 96–98].

One of the first three-dimensional simulations of this growth model was performed by Thijssen [99]. Thijssen et al. also derived the first statistical growth laws for the 3D case [94]. Smereka et al. refined the 3D simulations by applying a powerful level set methodology and confirmed the results of Thijssen [25]. Several more recent simulation studies of 3D grain growth and coarsening have since been published [88, 89].

In this study, we essentially follow the methods of Smereka et al. and further refine the statistics obtained by the authors mentioned above. In addition, for a given crystal system and geometry, we propose a simple equation to predict the prefactors of the late-stage growth power laws of a polycrystalline film.

5.2 Background

5.2.1 The van der Drift Model

In this model, a polycrystalline thin film begins as randomly distributed nuclei on a substrate surface. The orientation of these crystallites may be uniform, randomly distributed or preferentially weighted in certain directions. As more material is deposited each grain expands until it meets a neighbor; there a grain boundary is formed. Grain boundaries are assumed to be stationary. As growth perpendicular to the substrate continues, grains that increase in height more quickly than neighboring grains gradually subsume these neighbors. In this manner a fiber texture naturally forms around the fastest growth direction, and this texture sharpens with increasing film thickness.

The initial grain orientations are random and the growth velocity of a crystal facet depends only on its crystallographic orientation. This assumption is met when the mean free path of the gas atoms is smaller than the grain dimensions (no self-shadowing) and surface diffusion of adatoms is large enough for facets to develop, but is otherwise neglected. Note that this means these simulations are only directly applicable to films growth by chemical vapor deposition.

The crystalline facets considered for a given material can be found using the kinetic Wulff construction where the surface energy vectors are replaced with the growth velocities [25]. To make this construction, the growth velocity vectors for all face orientations are plotted from a common origin. Planes are placed perpendicular to these vectors a distance from the origin proportional to the magnitude of growth velocity. The crystal surface is the union of all plane surfaces closest to the origin. Every flat crystal facet corresponds to a minima and a cusp in the distribution of growth velocities versus facet orientation. This essentially means that the slower growing crystalline faces dominate the equilibrium growth shape. Figure 5.1 demonstrates the kinetic Wulff construc-

tion of a 2D grain and its evolution towards an equilibrium shape. Smereka et al. provide additional details on grain shape evolution [25]. In this study however, we have chosen to assume that all grains evolve to their final shape very quickly; thus all initial nuclei begin in their equilibrium shape.

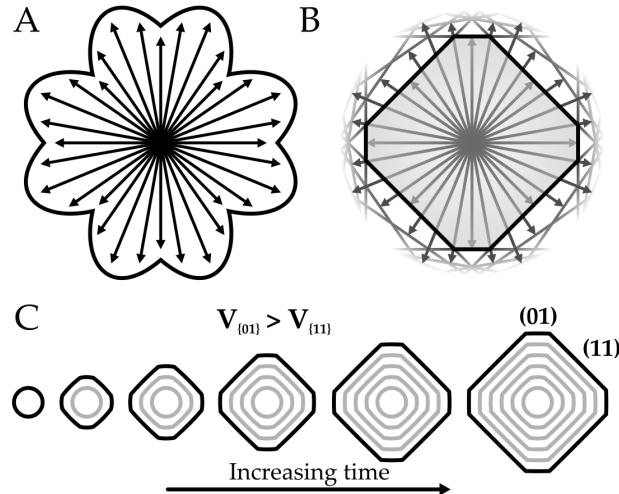


Figure 5.1: (A) Plot of face velocity versus orientation. (B) Kinetic Wulff construction from (A). (C) Initial circular grain evolving asymptotically into equilibrium Wulff shape.

When a crystal shape is composed entirely of facets, the fastest growth direction is calculated geometrically. The point on the crystal surface furthest from the origin corresponds to the fastest growth direction. If the vector from the crystal origin to this point is perpendicular to the substrate then the apex of the crystal surface in question will grow at least as fast as any other possible crystallite orientation. Note that most real crystal systems possess one or more symmetries and therefore will typically have multiple equivalent fastest growth directions. A cube made up of $\{001\}$ facets for example has 8 corners and therefore will have 8 fastest growth directions of $\langle 111 \rangle$ type.

5.2.2 Level Set Simulation

To simulate growth of a film surface we have used a level set construction. Every grain is described implicitly as the union of higher-dimensional faces. At each time step, the surface projection of each face and grain is calculated. Details on this method are given by Smereka et al. [25] Norris and Watson have pointed out the primary drawback of current implementations of this method, which is that they keep track of far more information than is required to describe the surface [89]. This is because a full 3D level set simulation calculates whether any point on a three dimensional grid is inside a grain or external to the film. To reduce the amount of information stored, we use an explicit grid in only the substrate plane axes. At each grid point, the height of the highest crystal was taken to be the surface and stored as a floating point value. Our simulations are therefore 2+1 dimensional.

The advantage of our approach is increased computational simplicity which allows more data to be collected and larger simulation domains to be used. The statistics are also computed after each growth step, allowing for snapshots of the surface or texture at any desired thickness. The disadvantage of our approach is that we cannot accurately model early stage growth or porous thin films.

We have used 2000 initial grains with up to 24 facets each and a 400x400 grid with periodic boundary conditions for this study. Films were grown to sufficient thickness to be in late stage growth, determined by the goodness of fit for statistical power laws. Each statistical curve shown is the average of 20 simulation runs (roughly equivalent to increasing the domain area by a factor of 20).

As noted above, initial grain nuclei were randomly distributed on the substrate with random orientations constructed from the three Euler angles. Each grain began in its final kinetic Wulff form. The initial nuclei were separated by

a minimum separation distance of 5 grid units to ensure that discretization artifacts do not appear before the grain occupies enough grid locations to evolve properly. Time steps were made sufficiently small so that no more than one major event (such as a grain top being subsumed) occurred per time step. Finally, all simulations presented in this study begin with the same mean grain spacing.

5.3 Analysis of Late-Stage Growth

5.3.1 Geometry

In late-stage growth, all remaining crystal tops have a fastest growth direction close to or perpendicular to the substrate. Each crystal top will be identical, save for being randomly rotated in the substrate plane. These tops have a pyramidal geometry, with three or more sides. An example of this is shown in Figures 5.2A and B, the late stage of a simulation of cubic crystals. In this figure, each surviving crystal top has 3 {001}-type faces, surrounding an apex given by a $\langle 111 \rangle$ direction of each crystal (the fastest growth direction of a cubic crystal). Each grain has a $\langle 111 \rangle$ direction very close to perpendicular to the substrate; this is why the crystal grains shown have survived.

Figure 5.2C shows a possible pyramidal geometry of a late-stage growth crystal top. This pyramid can be characterized by its aspect ratio. If we position a plane perpendicular to the fastest growth direction a height l below the apex we can compute the plane's area A . As a lateral dimension measure we will use the square root of the plane area. We therefore define the pyramid's aspect ratio as l/\sqrt{A} .

All kinetic Wulff shapes evolve into a pyramidal geometry in late-stage growth, not just cubic systems. Every given kinetic Wulff shape has a well-defined

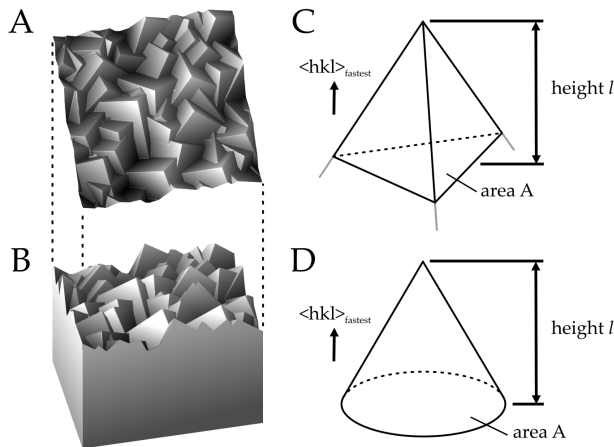


Figure 5.2: (A) Top view and (B) 3D view of an example film surface in late-stage growth. (C) Pyramidal crystal top. (D) Equivalent cone crystal top to (C).

fastest growth direction which is surrounded by 3 or more triangular faces. Figure 5.3 emphasizes this fact, showing the late-stage geometry of a wide variety of kinetic Wulff shapes. Kinetic Wulff shapes constructed from facets with low dihedral angles will have high l/\sqrt{A} aspect ratios and conversely geometries where the facets have high dihedral angles will have low l/\sqrt{A} values. In Figure 5.3 we see that as polyhedrons become more spherical (higher dihedral angles) the pyramidal aspect ratios become smaller.

5.3.2 Statistical Measures

From a practical standpoint, we are primarily interested in the overall morphological statistics of a thin film. The statistics collected in this study include mean grain area and diameter (alternatively grain boundary density), root-mean-square (RMS) surface roughness and texture versus film thickness. When grain nuclei are initially placed each grain is assigned an initial area and has an origin in the substrate plane. The initial area is defined by the

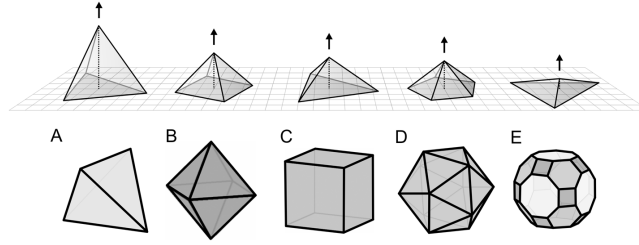


Figure 5.3: Various kinetic Wulff shapes and their associated pyramidal crystal tops in late-stage growth. Pyramid base area is constant in these images. Arrows show fastest growth direction.

convex polygon surrounding the origin which has the unique property that all points within the polygon are closer to the origin than all other crystal origins. These polygons are determined using the well known Voronoi tessellation method [100]. The mean area of all grains is denoted A_0 . The initial mean grain spacing d_0 is defined as the square root of A_0 for simplicity. All one-dimensional statistical measures are normalized by d_0 and all two dimensional statistics by A_0 . This normalization reflects the fact that the simulations do not have an absolute dimensional scale; rather all statistics are relative to the initial spatial distribution of nuclei. A_0 can also be computed in a simpler fashion by dividing the total simulation area by the number of initial nuclei.

All statistics are computed at the growth surface projected into a two-dimensional plane parallel to the substrate. The texture signal of a given grain is weighted by its area in this plane. Grain area is also considered to be the projected area as opposed to the true three-dimensional surface area of the exposed grain top.

By assuming that the pyramidal crystal tops behave similarly to cones (The analogous geometry between cone and pyramidal tops is shown in Figures 5.2C and D) and by neglecting the local environment around each grain, Thijsen predicted that the mean grain size $\langle d \rangle$ would vary with film thickness t as [99]

$$\langle d \rangle = d_\infty t^{2/5} \quad (5.3.1)$$

Where d_∞ is a constant prefactor. The prefactor term is of significant interest since it is the only metric which distinguishes the late stage growth properties of different crystal structures. The prefactor term represents the expected asymptotic value of late-stage growth statistics after factoring out the power law dependence on thickness. From this equation, the dependence of other statistical measures on thickness can be predicted including probability of grain survival $\langle P \rangle$, mean grain area $\langle A \rangle$ and RMS surface roughness σ_{RMS}

$$\langle P \rangle = P_\infty t^{-4/5} \quad (5.3.2)$$

$$\langle A \rangle = A_\infty t^{4/5} \quad (5.3.3)$$

$$\sigma_{\text{RMS}} = \sigma_\infty t^{2/5} \quad (5.3.4)$$

Where P_∞ , A_∞ and σ_∞ are the prefactors of grain survival, area and surface roughness respectively. The relationships between these prefactors and d are

$$P_\infty = d_\infty^{-2} \quad (5.3.5)$$

$$A_\infty = d_\infty^2 \quad (5.3.6)$$

$$\sigma_\infty = \sqrt{1 - \frac{\pi}{4}} \frac{l}{\sqrt{A}} d_\infty \quad (5.3.7)$$

The derivation of Equations 5.3.2–5.3.7 is given in Appendix A.2. The net result of these relationships is to predict the power law dependence of each statistical measure on thickness and the prefactors of each statistic. Furthermore, if one of the prefactors can be predicted, all of the rest can be.

5.4 Simulated Kinetic Wulff Shapes

5.4.1 Tetrahedron

The simplest regular polyhedron can be found in crystal systems that possess only $\{111\}$ facets and exhibit highly polar behavior. Silicon carbide thin films

for example can grow in this fashion [95]. If the $(\bar{1}11)$, $(1\bar{1}1)$, $(11\bar{1})$ and $(\bar{1}\bar{1}\bar{1})$ faces grow quickly enough to vanish only the $(1\bar{1}\bar{1})$, $(\bar{1}1\bar{1})$, $(\bar{1}\bar{1}1)$ and (111) faces will remain. This system will have 4 fastest growth directions perpendicular to the vanished $\{111\}$ faces, and an l/\sqrt{A} ratio of $(64/27)^{1/4} = 1.241$. Figure 5.3A shows a tetrahedral kinetic Wulff shape.

5.4.2 Great Rhombicuboctahedron

A near-spherical crystal can be constructed out of all faces of types $\{001\}$, $\{011\}$ and $\{111\}$. Saito has examined constructions of this type [101]. If all of these faces are regular polygons then the crystal is a great rhombicuboctahedron. This system has 48 equivalent fastest growth directions: all permutations of $\langle 1\ 1 + \sqrt{2}\ 1 + \sqrt{8} \rangle$. The l/\sqrt{A} ratio of this system is $2(13 + 6\sqrt{2})^{-3/4} = 0.2004$. This Wulff shape is displayed in Figure 5.3E.

5.4.3 Diamond System

The crystal system appropriate for diamond is a cubic geometry with only $\{001\}$ and $\{111\}$ facets. The resulting kinetic Wulff shapes were described by Wild et al. [11, 97] by using the ratio

$$\alpha = \sqrt{3} \frac{V_{001}}{V_{111}} \quad (5.4.1)$$

where V_{001} and V_{111} are the growth velocities of the $\{001\}$ and $\{111\}$ facets respectively. Smereka et al. performed detailed simulations on this crystal system [25]. Table 5.1 illustrates the morphology of the diamond Wulff shapes along with the fastest growth directions derived by Paritosh et al. [98] We have also computed the number of equivalent fastest growth directions N_d and the geometric ratio l/\sqrt{A} as a function of α .

Table 5.1: Growth parameters of the diamond system.

$\alpha = \sqrt{3} \frac{V_{001}}{V_{111}}$	Morphology	$\langle hkl \rangle_{\text{FASTEST}}$	N_d	l/\sqrt{A}
$\alpha \leq 1$	 Cube	$\langle 111 \rangle$	8	$(\frac{4}{27})^{1/4}$
$1 < \alpha < \frac{3}{2}$	  	$\langle \frac{3-2\alpha}{\alpha} 11 \rangle$	24	$\frac{\sqrt{2}(3\alpha-3)\sqrt{3-2\alpha}}{(6\alpha^2-12\alpha+9)^{3/4}}$
$\alpha = \frac{3}{2}$	 Cuboctahedron	$\langle 011 \rangle$	12	$2^{-5/4}$
$\frac{3}{2} < \alpha < 3$	  	$\langle 0 \frac{3-\alpha}{\alpha} 1 \rangle$	24	$\frac{(3-\alpha)\sqrt{2\alpha-3}}{(2\alpha^2-6\alpha+9)^{3/4}}$
$\alpha \geq 3$	 Octahedron	$\langle 001 \rangle$	6	$2^{-1/2}$

5.5 Results and Discussion

5.5.1 Surface Morphology and Texture

Figures 5.4 to 5.6 show the surface morphology and texture for tetrahedral, great rhombicuboctahedral and cubic kinetic Wulff shapes respectively. The cubic system is described in section 3.3 where $\alpha = 1$. The surfaces are plots of the function $\tan^{-1}(\partial z/\partial x)$, representing slope in the x-direction. The lateral dimensions are constant in all slope-maps, and the plotted thicknesses are given in terms of initial grain diameter d_0 . The left-most image in all three figures shows the initial grain nuclei distribution for the simulations. The textures are represented by stereographic projections of the predicted fastest growth direction. These projections cover the upper hemisphere of possible grain orientations with the boundary marked at 90° from the direction of the stereographic projection.

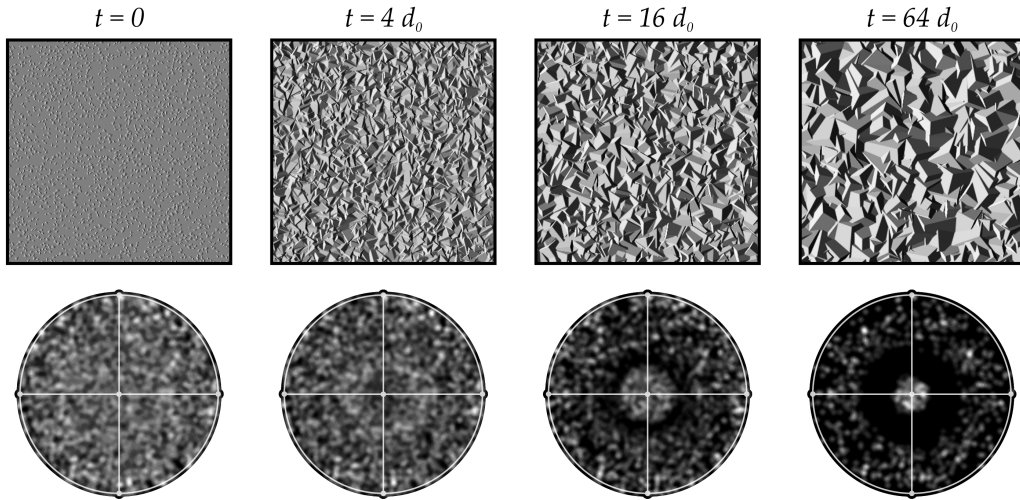


Figure 5.4: Surface slope-maps and $\langle 111 \rangle$ stereographic projections of all $\{111\}$ poles for tetrahedral crystals at various thicknesses.

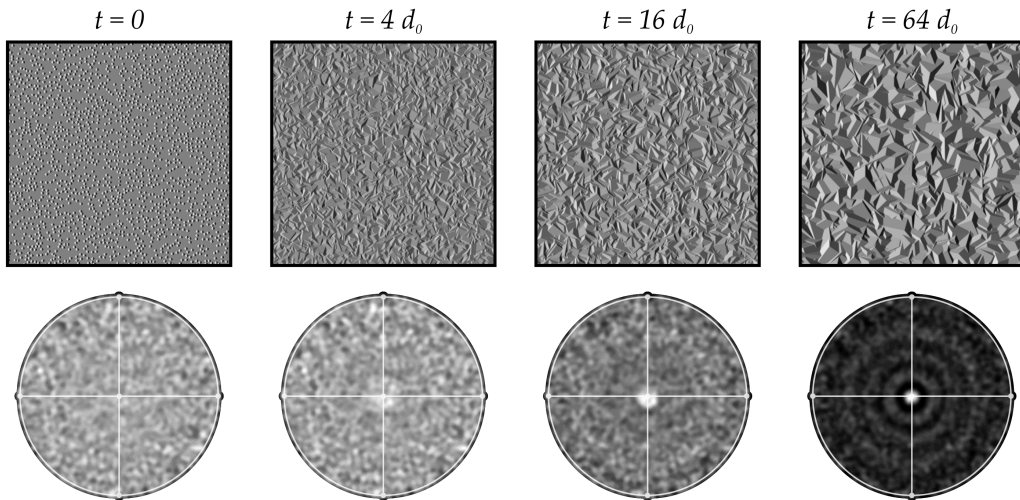


Figure 5.5: Surface slope-maps and $\langle 111 \rangle$ stereographic projections of all $\{111\}$ poles for great rhombicuboctahedral crystals at various thicknesses.

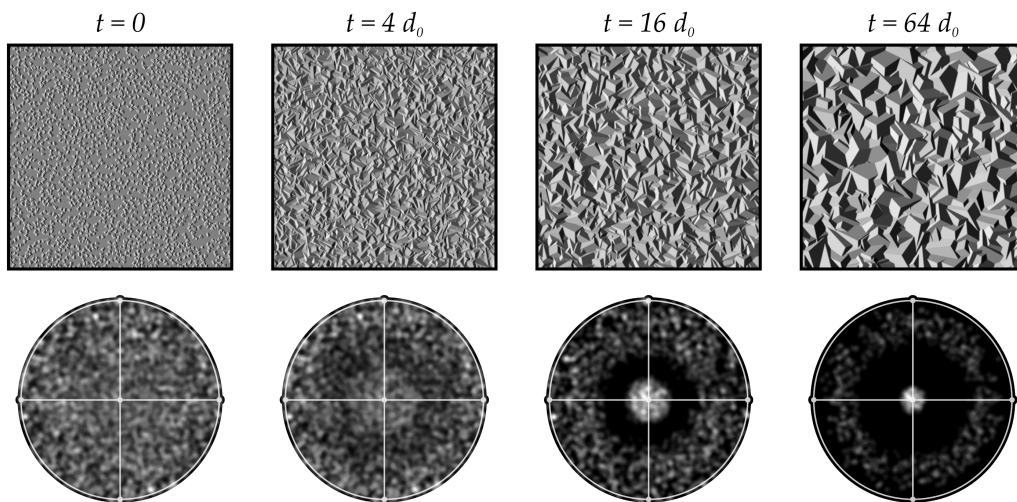


Figure 5.6: Surface slope-maps and $\langle 111 \rangle$ stereographic projections of all $\{111\}$ poles for cubic crystals at various thicknesses.

Despite significant variation in crystal geometry, the surfaces are visually similar. Each film begins as discrete nuclei, grows into a fine-grained continuous surface composed of all possible grain orientations and finally evolves into a surface of 3-sided pyramids similar to Figure 5.2A. The lateral length scales are all roughly similar for three films, suggesting that grain area or probability of grain survival depend only weakly on the given crystal's kinetic Wulff shape.

Each simulation begins with randomly oriented grains and evolves towards a fiber texture. The late-stage texture of the tetrahedral simulation shows the crystals with a $\langle 111 \rangle$ orientation dominating. Note that in Figure 5.4 all $\{111\}$ poles are plotted rather than just the polar orientations, as a real diffraction experiment cannot differentiate between a (111) and a $(\bar{1}\bar{1}\bar{1})$ diffracted spot. The simulation of great rhombicuboctahedrons evolves to a $\langle 1\ 1 + \sqrt{2}\ 1 + \sqrt{8} \rangle$ oriented film. The cubic simulation pole figures show $\langle 111 \rangle$ oriented crystals prevailing. All of these late-stage growth textures are correctly predicted in Section 5.4. Both the tetrahedral and cubic crystals have a ring of adjacent $\{111\}$ spots approximately 70° from the centre spot. Three separate rings can

be identified in the rightmost pole figure of the great rhombicuboctahedral simulation at spacings of about 25° , 50° and 75° . These ring spacings reflect the expected angles between neighboring poles.

The sharpness of the film textures is shown by the broadness of the spots and rings of the stereographic projections of Figures 5.4–5.6. A larger spot or wider ring corresponds to a wider angular distribution around the fastest growth directions and a small spot or thinner ring to a sharper texture. The sharpness of the texture appears to vary proportionally with the number of growth directions N_d of the kinetic Wulff shape.

5.5.2 Growth Statistics

The grain survival probability from the simulations of the crystal systems described above is plotted in Figure 5.7. The probabilities asymptotically approach the power law predicted by Thijssen et al. [94]. Best fit lines to these asymptotic values are shown in grey. These survival probabilities share the same dependence on thickness but have different prefactors, due to their differing geometry. The agreement between the simulation and the analytic asymptotic prefactors is excellent. The grain survival probability varies by only about a factor of 2 despite quite different kinetic Wulff geometries; therefore, probability of survival is only weakly dependent on the grain's Wulff geometry.

Figure 5.8 shows the RMS surface roughness values from simulations of the above crystal systems. Again, the statistical measure displays the expected power law behavior in late-stage film growth. Best fit asymptotic power laws are drawn on the figure in grey. RMS roughness varies by approximately an order of magnitude over these crystal systems, a much larger variance than that seen in the other statistical measures. This is due to the additional crystal top ratio l/\sqrt{A} dependence of Equation 5.3.7.

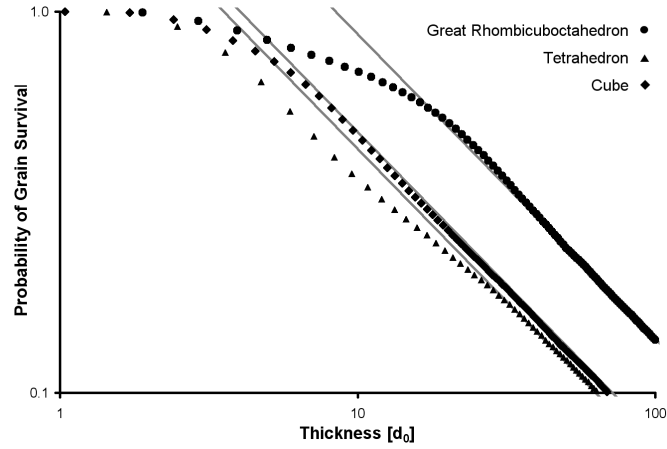


Figure 5.7: Probability of grain survival for different crystal geometries measured from simulation. Gray lines show asymptotic best fits.

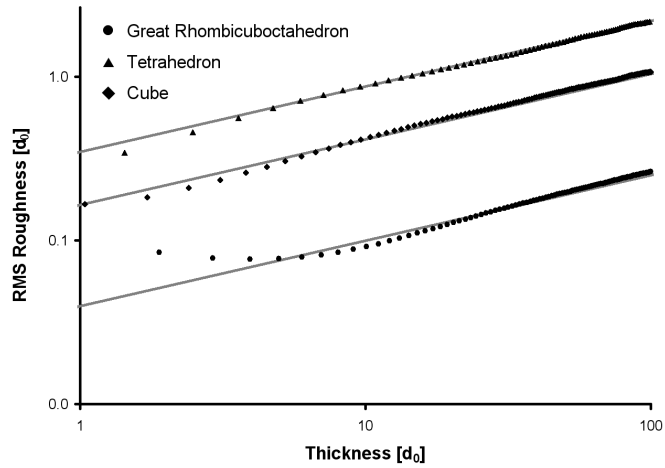


Figure 5.8: Surface roughness for different crystal geometries measured from simulation. Gray lines show asymptotic best fits.

5.5.3 Mean Grain Diameter Fit

The value of d_∞ depends primarily on the number of equivalent fastest growth directions N_d and the aspect ratio of the pyramidal crystal tops, the ratio of l/\sqrt{A} . Our simulations on the various kinetic Wulff shapes described in this study have allowed us to investigate the dependence of d_∞ on these two variables. At this time, there is no known analytic expression for the relationship of d_∞ , N_d and d_∞ . However, many different smooth functions can be fit to d_∞ . For this study we have computed the simple expression

$$d_\infty = 0.987N_d^{-0.317} \left(\frac{l}{\sqrt{A}} \right)^{-0.242} \quad (5.5.1)$$

This expression depends on the definition of mean grain diameter $\langle d \rangle$ as the square root of mean grain area $\langle A \rangle$. Modifying the normalization used or the definition of the lateral length scale will alter the numerical coefficients of Equation 5.5.1, but will not change the trends described in this study. This equation is graphically represented in Figure 5.9 along with the locations of some kinetic Wulff shapes on the d_∞ surface. From this figure we see that the largest diameter grains result from crystal systems with low aspect ratio pyramidal tops and few equivalent growth directions. Conversely the smallest diameter grains originate from crystal systems with many growth directions and high aspect ratio pyramidal tops. It should be noted however that few crystal systems exist in either of these extremes; a crystal system with many equivalent growth directions in its kinetic Wulff shape will be closer to a sphere and will therefore tend to have a low l/\sqrt{A} ratio. Another interesting point is that despite the wide variety of kinetic Wulff geometries shown in Figure 5.3, all d_∞ values fall between 0.42 and 0.61. This suggests that the mean grain diameter is not very sensitive to crystal geometry, at least for highly symmetric crystal systems.

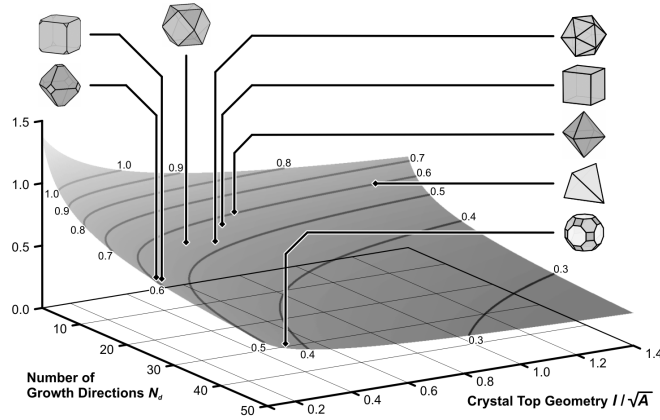


Figure 5.9: Mean grain diameter prefactor d_∞ as a function of N_d and the geometric crystal top ratio l/\sqrt{A} plotted from Equation 5.5.1. The locations of various kinetic Wulff shapes are also shown.

5.5.4 Growth Statistics for Varying Wulff Geometries

We performed simulations of the diamond crystal system to test the analytic prefactor relations described in this study. The face growth ratio α was varied from 1.0 to 3.0 in steps of 0.1. The prefactors were fit to the late-stage growth of each of these simulations, calculated from all data points at thicknesses beyond approximately 50 to 200 d_0 , depending on the time required for the film to reach power law behavior. For best fits of the prefactors P_∞ and σ_∞ the power laws were assumed to have $t^{-4/5}$ and $t^{2/5}$ dependencies respectively. The results are graphed in Figures 5.10 and 5.11, along with the analytic prefactor predictions of Equations 5.3.2 to 5.5.1. The prefactor predictions are constant for the ranges $\alpha \leq 1$, $\alpha \geq 3$ and $\alpha = 1.5$. All other values of α have a smoothly varying prefactor, tending to negative infinity as the grain shape approaches $\alpha = 1$, 1.5 or 3.

It is important to examine in more detail the locations on the graph where the analytic expression predicts a prefactor of negative infinity, corresponding to a prediction of zero RMS surface roughness. Strictly speaking, this result is

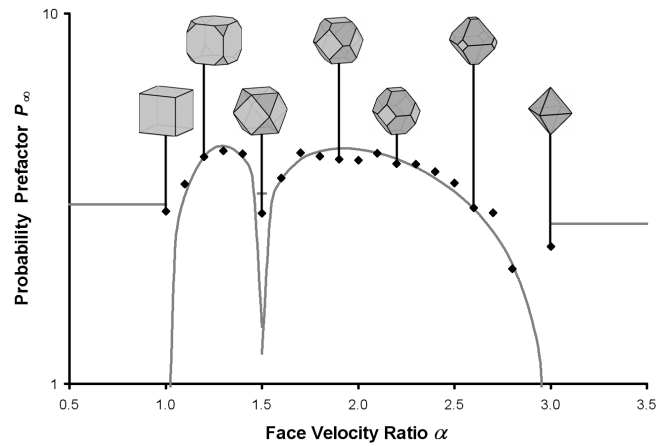


Figure 5.10: Prefactors of grain survival probability measured from simulations of diamond crystals. Gray line shows predictions from Equations. 5.3.2, 5.3.4 and 5.5.1. Some kinetic Wulff shapes shown above.

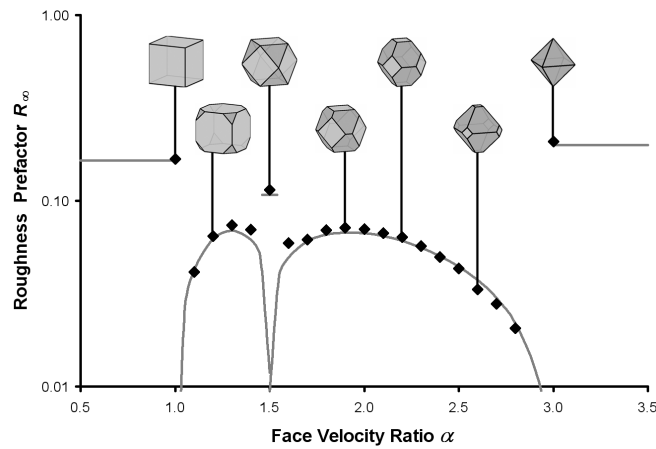


Figure 5.11: Prefactors of surface roughness measured from simulations of diamond crystals. Gray line shows predictions from Equations. 5.3.2, 5.3.7 and 5.5.1. Some kinetic Wulff shapes shown above.

correct and not an artifact. The caveat however is that the required thickness before crossover into late-stage growth increases to infinity as the geometric α ratio approaches these singularities at 1.0, 1.5 and 3.0; therefore a real film will never exhibit this behavior.

5.5.5 Model Limitations and Generalizations

We have shown using simulations that the growth statistics of a polycrystalline thin film depend smoothly on the geometry of its kinetic Wulff shape. However, to perform these simulations we have made several assumptions that should be discussed in more detail.

Firstly, the initial grain nuclei are randomly oriented and randomly distributed in space. The randomness or lack thereof in initial grain orientation depends on the material system in question. If epitaxial relationships exist between the film and substrate the grains will almost certainly be heavily biased towards certain orientations. Even films unlikely to grow epitaxially (an amorphous substrate for example) can have preferential initial nuclei orientations. However, if all possible orientations are present (though some are far less likely than others), then in late-stage growth only grains close to the fastest growth direction will survive and all remaining grains will have equivalent geometry. The numerical prefactors described in this study will become invalid, but the trends observed should remain. All other parameters being equal, geometry should still influence the growth statistics in the manner described. On the other hand, the assumption of random initial nuclei positioning is far more general. The fastest growth directions of the vast majority of grains are not exactly perpendicular to the substrate even in late-stage growth. This means that the pyramidal apices of the crystal tops move laterally in the substrate plane as the film thickness increases. By the time late-stage growth is reached, most crystal tops will have traveled laterally many multiples of initial diameter

d_0 and any initial spatial correlation between crystal tops is lost.

The growth velocity of every crystal facet was assumed to depend only upon the facet's orientation. This is the case when material flux deposited on the film surface is not dependent on direction and surface diffusion is great enough for smooth facets to develop. This model does not take into account any self-shadowing caused by neighboring grains or any long range diffusion which could favor different local grain configurations (perhaps certain grain boundary orientations permitting asymmetric diffusion). In our simulations, every grain began in its final kinetic Wulff configuration, as though it was able to evolve very quickly into this shape. This may or may not be the case for a given film deposition process. Since grains tend to evolve towards a less spherical shape, their survival probability may be initially enhanced by slow evolution towards the Wulff shape. However, as long as all surviving grains have grown very close to the equilibrium Wulff shape when they reach late-stage growth, the film will be virtually indistinguishable from a film where all initial nuclei began in the Wulff shape.

Finally we have assumed zero porosity and no re-nucleation of new grains during growth. Porosity can occur in early growth for many possible kinetic Wulff shapes, but when late-stage growth is reached the film should be fully dense, barring self-shadowing or very low surface diffusion rates. In deposition processes with enough surface diffusion to form crystalline facets, re-nucleation is very unlikely. If it did occur in late-stage growth, the new grains would be competing only with grains very close to the optimal orientation. Unless these grains also had a fastest growth direction very close to perpendicular to the substrate or were positioned on a crystal apex, they would be quickly subsumed. Equation 5.3.7 also merits more attention. Assuming that all grains at the film surface have the same pyramidal geometry (cone-like) and are close to the fastest growth orientation then the relationship between RMS surface roughness RMS and mean grain diameter $\langle d \rangle$ (the square root of mean

grain area $\langle A \rangle^{1/2}$) is in general given as

$$\sigma_{\text{RMS}} = \sqrt{1 - \frac{\pi}{4} \frac{l}{\sqrt{A}} \langle d \rangle} \quad (5.5.2)$$

This relation will depend only on the aspect ratio l/\sqrt{A} of the crystal top pyramids. This equation applies irrespective of the deposition or simulation type as long as all grains have identical pyramidal geometry, no spatial correlation in the substrate plane and random rotation about the fastest growth axis, which itself must be near-perpendicular to the substrate for all surviving grains.

5.6 Summary

Our study has again confirmed the power laws predicted by Thijsen for a variety of kinetic Wulff geometries. We have also described the dependence of asymptotic growth statistics on geometry. All other variables being equal, modifying the number of growth directions N_d and crystal top aspect ratio l/\sqrt{A} will modify a polycrystalline film's roughness σ_{RMS} and probability of survival $\langle P \rangle$ at a given thickness by

$$\sigma_{\text{RMS}} = \frac{1}{N_d^{0.32}} \left(\frac{l}{\sqrt{A}} \right)^{0.76} \quad (5.6.1)$$

$$\langle P \rangle = N_d^{0.63} \left(\frac{l}{\sqrt{A}} \right)^{0.48} \quad (5.6.2)$$

From these relations we can see that Wulff geometries with more equivalent fastest growth directions will have increased grain survival probabilities (and thus decrease mean grain area) but lower the RMS surface roughness of the film. An increasing crystal top aspect ratio l/\sqrt{A} will both roughen the surface and increase the grain survival probability. Finally, the local deviation in grain survival probabilities displays much more variance than the local deviation in surface roughness of a polycrystalline thin film.

6

Simulations of Self-Shadowing During Growth of Faceted Polycrystalline Films ¹

6.1 Motivation

Like many other types of thin film growth, polycrystalline film growth is characterized by self-affine kinetic roughening of the surface [102]. The typical model used to analyze this type of growth is the Family-Vicsek equation. This equation relates root-mean-square (RMS) surface roughness σ (sometimes called interface width) to thickness t and the in-plane system size L

¹Material in this chapter has been submitted to:

► *Acta Materialia*

[103]

$$\sigma(L, t) \propto \begin{cases} L^\alpha, & L^\alpha \ll t^\beta \\ t^\beta, & L^\alpha \gg t^\beta \end{cases} \quad (6.1.1)$$

where α is the roughness exponent and β the scaling exponent [103]. With this model, different types of film growth can be classified into *universality classes* with different values of the exponents (α, β) . An example is the growth model described by the well-known Kardar-Parisi-Zhang (KPZ) equation [104]; various authors have attempted to find the values of α and β for the KPZ equation in both analytic [105, 106] and numerical studies [107].

In many growth systems however, the scaling laws depend on the local length scale l of the measurement, a scenario described as *anomalous roughening* [108]. Various authors have introduced an additional universality class exponent to incorporate the anomalous scaling. Examples are a separate local exponent α_{loc} [109], or a new exponent for spectral roughness [110]. Even more recently, several authors have reported a measured experimental dependence of the β exponent on the local length scale l [111, 112].

Many studies have been performed to analyze the effects of differing materials, temperature and deposition rate on polycrystalline film growth [113]. However, self-shadowing has received comparatively little attention. In this work, we deposited thin films where both faceting and self-shadowing are expected to occur and measured their surface statistics. We then used simulation to understand the growth of faceted polycrystalline thin films under realistic growth conditions; specifically we incorporate self-shadowing by using a ballistic deposition model. This allows us to model various physical vapour deposition techniques such as sputtering, evaporation or low pressure chemical vapor deposition. Lastly we analyze the anomalous scaling behaviours of faceted polycrystalline film growth under these different conditions.

6.2 Faceted Polycrystalline Thin Films

The dominant surface features of many polycrystalline thin films are low-index crystalline facets. The growth rate of these facets determines the equilibrium grain shape (referred to as the kinetic Wulff shape [11]) if the diffusion rate along the low-index facets is much higher than the rate of other diffusion events [12]. The regime of interest is where the deposition temperature and therefore the adatom diffusion lengths are high enough to form facets but not high enough for kinetic roughening to occur [114, 115]. For some materials this regime occurs for room temperature deposition [116] and for others at elevated temperatures [117, 118].

To demonstrate the surface structure of this class of surfaces, we have prepared aluminum thin films of different thicknesses by magnetron sputtering at 200 W (1.7 Å/s) onto cleaned silicon wafers with a thin natural oxide. We have used atomic force microscopy to map the Al film surfaces. Figure 6.1 shows the slopemaps of some of the films. The surface slope color channels are linear combinations of the formulae $\theta_x = \tan^{-1}(\partial z/\partial x)$ and $\theta_y = \tan^{-1}(\partial z/\partial y)$.

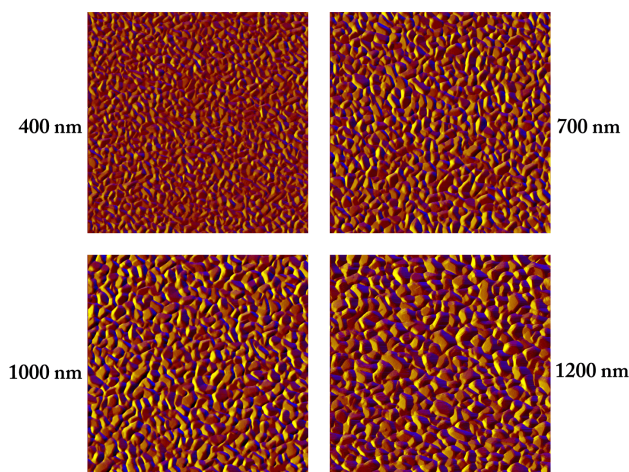


Figure 6.1: AFM slopemaps of sputtered Al thin films at four different thicknesses. Each slopemap has side length 2 μm .

From our Al films, we have measured the dependence of the scaling exponent β on local length l by calculating the RMS surface roughness from square windows with side length l . These results are plotted in Figure 6.2. A large difference between the local and global scaling exponents is clearly visible. The global value appears to be asymptoting towards $\simeq 0.82$ and the local exponent to $\simeq 0.41$, around half of the global value. Our measured disparity between the local and global exponents is even stronger than those measured by Yanguas-Gil et al. [111]. Our scaling exponents also appear to be asymptoting for small lengths as well as large lengths.

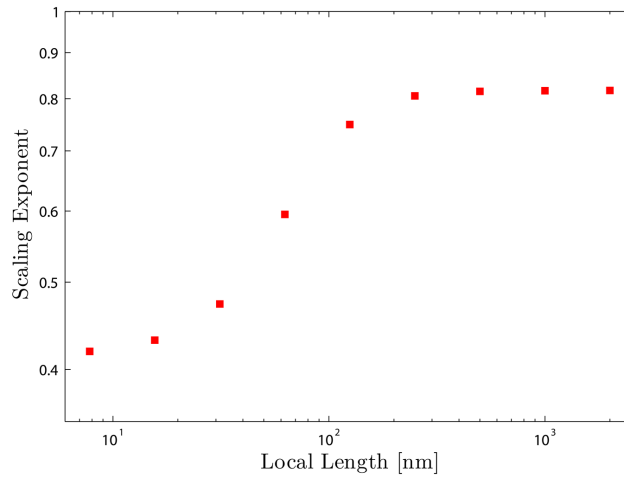


Figure 6.2: Scaling exponents of sputtered Al films measured over different length scales.

Lastly we have measured the local roughness exponent α_{loc} to be very close to 1 for all films. Since the global roughness exponent α is certainly higher than 1 for our films, their growth can be classified as a *super-rough* process [110].

6.3 Simulation Methodology

6.3.1 van der Drift Model

Previous simulations of polycrystalline grain growth have typically assumed that the growth rate of each facet is determined only by its crystallographic orientation, and is constant for all times. This simplified model was initially proposed by Kolmogorov [86] and van der Drift [87] and is usually referred to as the van der Drift model. Growth of this type is typical in interface-limited growth such as chemical vapor deposition (CVD). Thijsen et al. derived scaling laws for this model and were among the first to simulate competitive grain growth in three dimensions [94]. Smereka et al. used a level set methodology to produce the first true 3D simulations of this model [25]. In a previous study we used a similar methodology to calculate detailed growth statistics of the van der Drift model in 2+1 dimensions for chemical vapor deposition [90].

In this study, rather than assuming the growth of each facet depends on crystallographic orientation, we instead calculate facet growth velocity with a ballistic deposition model. We allow a range of angles for the deposition flux. Similar studies have also modeled different angular flux distributions [119]. Our simulations describe thin films deposited at low pressures, where the mean free path of the vapor-phase deposition atoms is much larger than the dimensions of the local film structure. In particular we examine the role of self-shadowing, an effect where taller grains produce a shadowed region where atomic flux is less likely to reach adjacent grains. We demonstrate that self-shadowing is an important effect even for atomic fluxes close to the substrate normal.

6.3.2 Initial conditions and grain morphology

In our simulations, we assume that a polycrystalline film begins as nuclei randomly scattered on the substrate surface. There is no long-range coordination between these nuclei; however, the propensity of adatoms diffuse into clusters on the substrate surface creates a minimum spacing between initial nuclei. For that reason, we use a minimum spacing when generating initial coordinates to prevent nuclei from forming with an unphysical proximity to each other. In this study we also assumed a random initial crystallographic orientation of each grain. Periodic boundary conditions were used and the ratio of initial nuclei to simulation field size was decreased until the results converged.

Each grain in the simulation is defined implicitly as a union of 4-dimensional facets. The surface is calculated at each timestep by computing the union of all grains projected onto a dynamically growing / shrinking 3D array of points in the simulation space. For more details see [25]. Rather than using a constant velocity for each facet as was done in [25] and Chapter 5, the velocity is recalculated at each timestep using the ballistic deposition model described Section 6.3.3.

Here we analyze three different grain morphologies. The first shape is cubic, constructed from $\{001\}$ facets. For the second we add $\{111\}$ facets to construct a cuboctahedron. The final shape also includes $\{011\}$ facets and is referred to as the rhombicuboctahedron. The initial distance of each facet from the grain origin is constant, to create a hemispherical initial grain nucleus. As the simulations progress, the geometry of each grain will change depending on how much flux each facet receives.

6.3.3 Ballistic mass deposition and surface evolution

We have used a ray projection method to calculate the growth velocity of each facet. Each timestep, 10^6 rays are generated above the highest point of the surface and advanced until a collision with a face is detected. The total number of collisions is taken to be the mass flux received by that face for that time step. In this way, the actual deposition flux received by each face is computed in a realistic manner. Figure 6.3(a) shows how a face is shadowed by the surrounding grains and by itself.

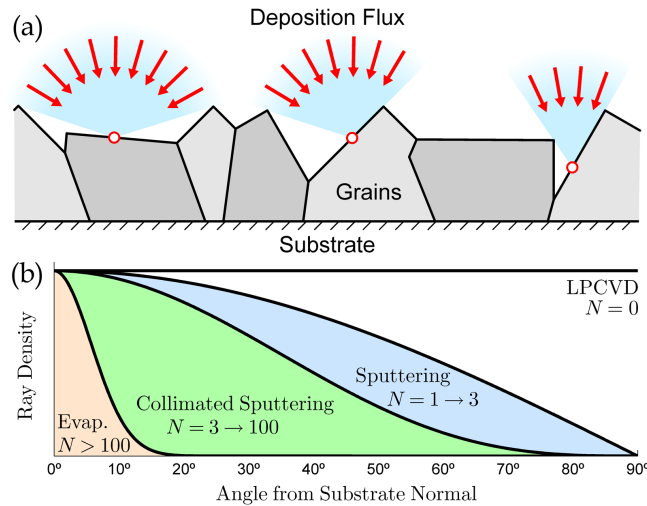


Figure 6.3: (a) Self-shadowing of incoming flux on an example surface. Flux received at each point is decreasing from left to right. Note that the flux received by each face is the sum of all points on that face. (b) Angular distribution of rays for different deposition techniques.

To simulate different physical vapour deposition methods we modify the distribution of incoming rays with respect to the angle from the substrate normal θ . In this study, we assume the angular distribution takes the form $\cos^N \theta$ where N is the “sharpness” of the texture. Fig. 6.3(b) plots different values of N . A value of $N = 0$ corresponds to a uniform distribution of ray angles, which is

the case for LPCVD. Sputtering produces distributions similar to $1 < N < 3$ [120]. Sputtering through a flux-collimating mask produces distributions given approximately by $3 < N < 100$ [121]. And finally values of $N > 100$ are considered to be representative of evaporation deposition sources. Normalizing the distribution gives

$$\rho(\theta) = (N + 1) \cos^N \theta \sin \theta \quad (6.3.1)$$

A more realistic model for the thermalization of an atomic flux can be constructed by assuming a Maxwellian distribution function for the deposition atom energies. Yanguas-Gil et al. have constructed such a model, where the angular distribution is [111]

$$\rho(\theta) = \frac{(1 + 2 \cos^2 \theta) \exp(z^2 \cos^2 \theta) [1 + \operatorname{erf}(z \cos \theta)] + \frac{2}{\sqrt{\pi}} z \cos \theta}{\exp(z^2) [1 + \operatorname{erf}(z)]} \sin \theta \quad (6.3.2)$$

where z is a normalized directional velocity. This Maxwellian model more accurately models the angular flux as a continuum. However, it can be shown that the cosine distribution given in Equation 6.3.1 is recovered from Equation 6.3.2 in the limit of large N if we set $N = 2z^2$. Additionally, both distributions reduce to $\sin \theta$ when $N = z = 0$. The cosine distribution is therefore a reasonable approximation, and has experimental confirmation [120, 121].

Every timestep, each face is moved forward at a rate proportional to the number of rays received divided by its exposed area. To ensure that each face occupies enough grid points to accurately sample the incoming flux and allow for an accurate measurement of exposed area, we advance all faces uniformly for the first ten timesteps, forming a nearly-hemispherical initial grain nucleus. Note that after ten timesteps, the fraction of the substrate covered by grains is still small; this ensures that these non-shadowed growth steps do not affect the film growth or morphology. Ballistic deposition is used for all remaining timesteps. Face area is measured from total occupied grid points, scaled by the direction-dependent grid density. Lastly, to avoid discretization errors global

growth speed is scaled down such that no face advances more than a few grid points at each timestep.

6.3.4 Diffusion

Diffusion enters into the simulation in two ways. The first effect of diffusion is caused by our assumption that each facet grows outwards perfectly perpendicularly. This means that each deposited mass unit is free to diffuse over the facet and that it will do so in a manner that keeps the face aligned along the same crystallographic direction at all times. This is a justifiable assumption, as faceted polycrystalline thin films tend to grow in a stepwise fashion [122]. We also assume that deposition flux is not shared between adjacent faces, equivalent to an infinite 3D Ehrlich-Schwoebel barrier existing between all crystal faces [122].

The second effect of diffusion is in early stages of film growth. Before the film is continuous, a large number of rays impact the substrate. For statistical purposes, we have fixed the initial distribution of grain nuclei. We therefore allow the mass units generated by substrate collisions to go on a random walk, with the mass being added to the first face encountered. This more closely approximates true thin film growth and avoids normalization issues before the film is continuous. This diffusion model is deliberately simple since we are primarily interested in the late-stage growth of faceted films; in the early stages of growth, the faceting assumption likely breaks down. Diffusion will be treated more comprehensively in future studies.

6.3.5 Statistical measurements

For convenience, we define the initial grain spacing d_0 as the square root of the initial grain area A_0 . If this value is initially normalized to 1, then

the instantaneous mean grain area A projected into the substrate plane can be calculated by dividing the substrate area by the number of grains still present at the film surface. The mean survival probability P of a grain at any thickness is then simply $1/A$. All other one-dimensional statistics such as mean film thickness h and RMS surface roughness σ are given in units of d_0 . Film porosity is calculated as the unfilled fraction of simulation slices at different thicknesses. Mean grain area, diameter and probability can also be calculated from slices.

6.4 Results and discussion

6.4.1 Surface morphology and texture

Figures 6.4–6.6 show the surface morphology and texture of the cubic, octahedral and cuboctahedral crystal systems respectively. The surfaces at four different thicknesses and three different N values for the angular ray distribution are shown. The plotted surfaces are slopemaps, i.e. tinted and shaded locally with the function $\partial z/\partial x$. Texture is encoded into the color of each grain as the local crystallographic vector normal to the substrate. Identical initial conditions were used for each crystal system, making the surfaces almost indistinguishable at $h = 1/4d_0$.

The most visible trend on the film surfaces is the large difference in grain size / number of surviving grains with different N values of the angular flux distribution. This is the primary effect of self-shadowing; smaller N values mean that many more rays are incident at high angles from the substrate normal. These high-angle rays can only reach the tallest grains, as these grains shadow the shorter grains. This asymmetry in flux received allows the tallest grains to grow taller still, which leads to a feedback loop where grains

CHAPTER 6: SELF-SHADOWING IN POLYCRYSTALLINE FILM GROWTH

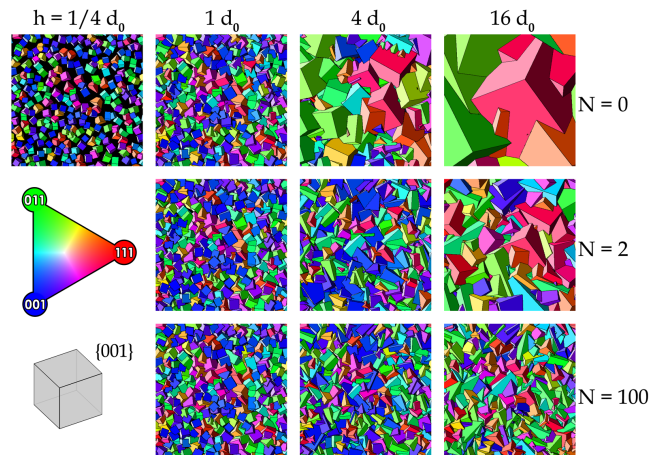


Figure 6.4: Surface morphology and texture of cubic simulations.

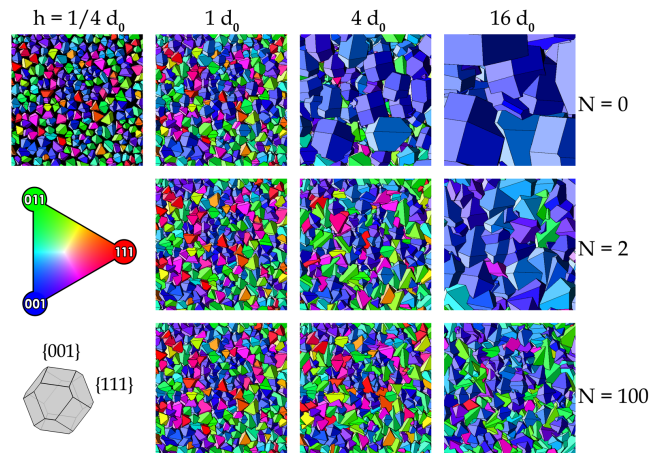


Figure 6.5: Surface morphology and texture of cuboctahedral simulations.

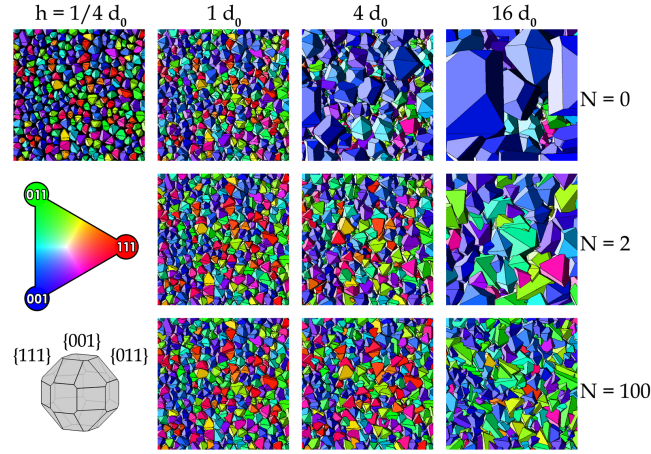


Figure 6.6: Surface morphology and texture of rhombicuboctahedral simulations.

with low heights are quickly subsumed. By contrast, when N is large most ray angles are close to the substrate normal and are therefore equally likely to reach any grain, regardless of height. The surface of these films is much smoother with many more grains present at equivalent thicknesses compared to the low N simulations.

In Figure 6.4 the texture evolves from a random distribution to a combination of $\langle 011 \rangle$ - and $\langle 111 \rangle$ -oriented grains. Figures 6.5 and 6.6 both evolve towards a primarily $\langle 001 \rangle$ -oriented texture. The faster growth directions appear to be independent of the value of N , though the surface evolves more quickly to its final texture for lower N values. The grains that eventually dominate the surfaces are fairly uniform in their orientation, but these *fastest growth directions* are not the same as those predicted in previous grain growth simulation studies [25, 90]. In those studies, the growth velocity of each facet depended only on crystallographic orientation. The fastest growth directions were therefore given by the points on the kinetic Wulff shape furthest from the grain origin. For our grain geometries, this rule would predict fastest growth directions of $\langle 1, 1, 1 \rangle$, $\langle 0, \sqrt{3} - 1, 1 \rangle$ and $\langle \sqrt{3} - \sqrt{2}, \sqrt{2} - 1, 1 \rangle$ for cubic, cuboctahedral and

rhombicuboctahedral grain respectively. Some of the grains in the cubic simulation have the predicted orientations, but all other tested shapes do not. The reasons for this deviation are currently unknown, but it is unlikely that assumptions of the previous simulations analytic models apply if self-shadowing occurs during growth. Further study is needed to understand what factors contribute to the asymptotic texture in self-shadowed thin films.

6.4.2 Cross sections

Another view of the grain morphology and texture evolution is shown in Figure 6.7 as film cross-sections. Figure 6.7 shows the same texture trends as Figs. 6.4–6.6. In all cases, the grain diameters increase with film thickness and lower N values lead to higher grain diameters at a given thickness. Surface roughness also increases with lower N values for both grain types. Besides the late-stage texture, the primary difference between the two grain shapes is that the rhombicuboctahedral simulation of $N = 0$ is highly porous and the $N = 2$ simulation shows small amounts of porosity near the substrate. The cubic grains by contrast show no porosity at all. This is because there are not enough facets present on the kinetic Wulff shape to form the large vertical canyons seen in the rhombicuboctahedral simulations. In reality even cubic grains could eventually form pores, but only in the limit where grains are large enough that incoming flux cannot diffuse to the lower portions of the facet; thus when the assumption that all grains are perfectly faceted breaks down.

6.4.3 Growth statistics

The RMS surface roughness of various simulations is shown in Figure 6.8. For all grain geometries, a lower N value corresponds to a rougher film surface. $N = 0$ in particular produces extremely rough surfaces, due to the low num-

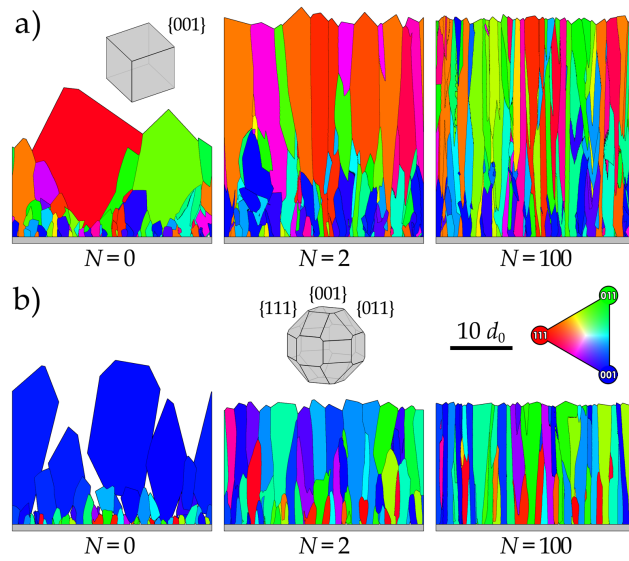


Figure 6.7: Cross-sectional slices of a) cubic and b) rhombicuboctahedral simulations with different values of N . Note that the coloring reflects the grain direction perpendicular to the substrate, and that the cubic $N = 0$ simulation was stopped early because the number of surviving grains dropped too low.

ber of surviving grains at the film surface. A small number of large grains will increase the interface width (distance from highest to lowest point on surface) of the film; this also increases the RMS surface roughness. Higher RMS roughnesses were observed for grain geometries with more facets for all N values. A slight minima is visible in some of the simulation roughnesses just above $d_0 = 1$. This feature corresponds to the initial nuclei (with a spacing of $1 d_0$) zipping up to form a contiguous surface. The simulated surfaces that had difficulty closing the surface did not exhibit this minima, an example of which is shown in 6.7b. Lastly, most surface roughnesses begin to exhibit power law behaviour in late-stage growth.

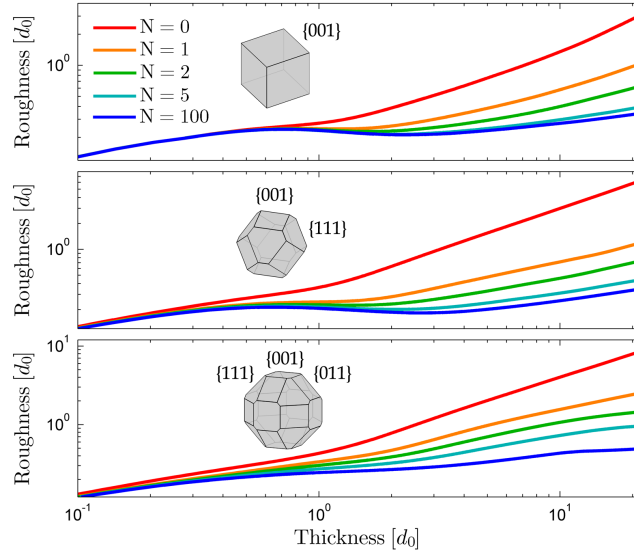


Figure 6.8: RMS surface roughnesses plotted against mean thickness for different crystal systems and N values.

The probability of grain survival can be calculated in two ways; either by counting the grains on the surface at each timestep (corresponding to some mean film thickness), or by counting the grains in slices taken from different heights. This second method has been used experimentally to analyze SiC films [91]. The grain survival probability calculated both ways is plotted in Figure 6.9 for the cubic simulations. Initially all grains are present, but at

some crossover thickness τ grains with less favourable orientation and local organization begin to be subsumed by more favourable grains. As seen in Figure 6.7, grain survival probability decreases with decreasing values of N . All simulations appear to be asymptoting towards power laws, though lower N values exhibit this behaviour at lower thicknesses. Lastly, measuring probability of survival from slices always gives a lower value at a given thickness than measuring at the film surface, with the discrepancy between the two increasing for lower N values.

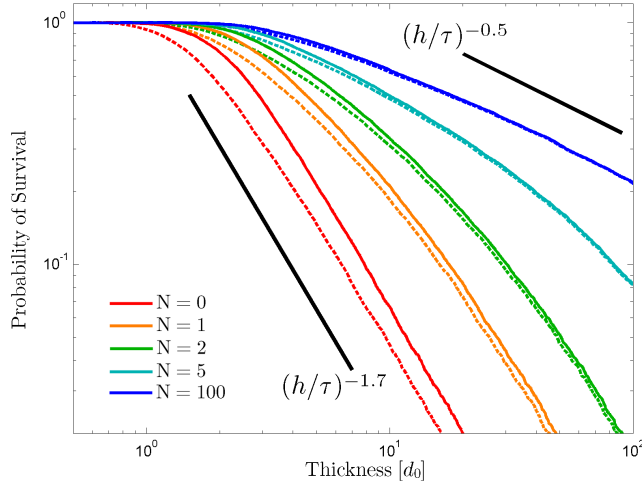


Figure 6.9: Grain probability of survival calculated from cubic simulations. Solid lines are calculated from film surface and plotted against mean thickness. Dashed lines are calculated from slices and plotted against slice height. Two example power laws are shown in black.

Figure 6.10 shows the porosities of the three crystal systems over different thicknesses for 5 different N values. All systems show some initial porosity at the substrate which then initially decreases with increasing film thickness. For all cubic simulations, cuboctahedral simulations with $N \geq 1$ and rhombicuboctahedral simulations with $N \geq 5$ the porosity drops to virtually zero. The porosity of the remaining simulations begins to increase and eventually nearly levels off. The rhombicuboctahedral simulations with $N = 1$ and 2

eventually begin to drop towards zero as well.

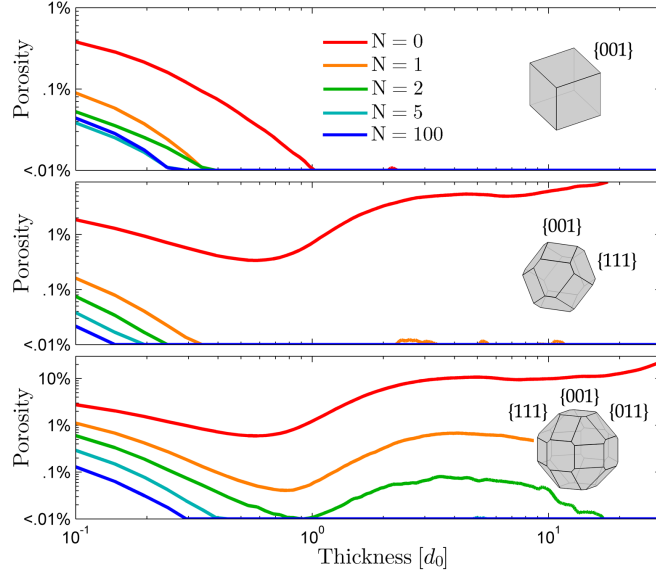


Figure 6.10: Porosities measured from slices for different crystal systems and N values.

Referring to Figure 6.7(a) we can see the reason porosity of the cubic simulations drops to zero; there are no limiting facets that allow for near-vertical grain boundaries that cause the deep trenches visible in 6.7(b). Only crystal systems with a high enough number of facets and ray distributions with low N values can asymptotically approach a constant, non-zero porosity. An example of experimental evidence for this phenomena is given by Dollet et al. [123] The AlN films in that study appear highly porous, and the authors identify a hexagonal set of 13 crystal facets, very comparable to our simulations of cuboctahedral grains with 14 facets. By contrast, reactively sputtered AlN was found to contain only a small volume percentage of voids [124] and pulsed laser deposited (PLD) AlN at low pressures had no detectable voids [125] (PLD has N values falling approximately from 2 to 20 placing its angular flux distribution between that of sputtering and evaporation [126]). Interestingly, Figure 18 in [125] shows deep trenches forming between grains as the

pressure of NH_3 inside the chamber is increased. This also agrees with our results because increasing gas pressure will cause the incoming atomic flux to thermalize, leading to larger N values of the angular distribution of incoming atoms.

6.4.4 Dependence of scaling laws on self-shadowing

Late-stage power laws of the type observed in Figures 6.8 and 6.9 have been predicted and observed for an extremely diverse array of thin film materials and microstructures. As discussed above, most morphological statistics of a self-affine surfaces asymptotically approach a scale-invariant function given by

$$G = \left(\frac{t}{\tau}\right)^d \quad (6.4.1)$$

where G is any statistical measure and d is a scaling exponent. For polycrystalline films where the growth velocity is constant, Thijsen et al. predicted a scaling exponent β for RMS surface roughness of $\frac{2}{5}$ and an exponent of $-\frac{4}{5}$ for grain survival probability. Another derivation of these exponents and a geometric formula for calculating τ is given in Chapter 4, again assuming constant rate of expansion for all facets.

In the current study, a wide range of exponents have been observed. These are plotted in Figure 6.11. For graphical clarity, the data is spaced by the mean flux angle given by

$$\langle\theta\rangle = (N+1) \int_0^{\pi/2} \theta \sin\theta \cos^N\theta d\theta \quad (6.4.2)$$

$$= \frac{\sqrt{\pi} \Gamma(\frac{1}{2}N+1)}{2 \Gamma(\frac{1}{2}N+\frac{3}{2})} \quad (6.4.3)$$

As N increases, our measured scaling exponent β decreases and the grain survival probability exponent increases. Interestingly, the scaling exponent asymptotically approaches 0.4; the value predicted for constant facet growth

velocities. The survival probabilities by contrast cross the predicted value of -0.8 and approach approximately -0.5 with increasing N . Karabacak et al. have observed the scaling exponent β asymptoting towards 0.4 as surface diffusion increases for sputtering experiments and simulations [115]. At low diffusion rates they measured increased β values as the deposition noise began to dominate film growth; our results demonstrate that highly shadowed deposition fluxes can also lead to increased values of β .

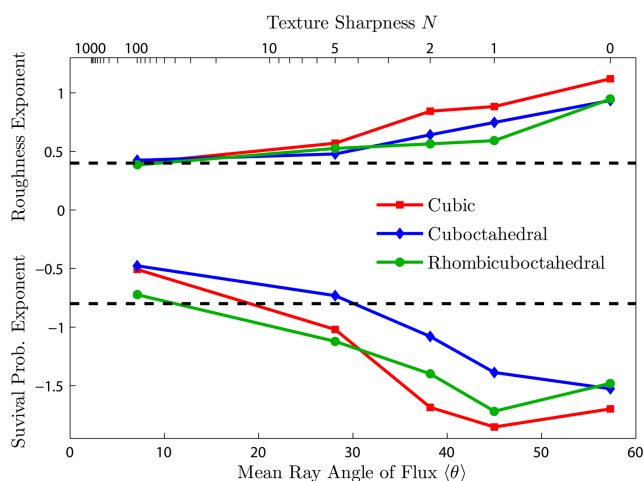


Figure 6.11: Scaling and probability of grain survival exponents measured in the current study. Dashed lines show the expected exponents for the case where facet growth velocities are constant.

Radmilovic et al. have measured the scaling exponent of the mean grain diameter of β -SiC films as 0.51 using cross-sectional transmission electron microscopy (TEM) studies [95]. A more exact measurement using an improved planar wedge TEM technique by Spiecker et al. yielded an exponent of 0.68 for the same type of SiC films [91]. This technique is described in Figure 6.12 and the measured data of Spiecker et al. is reproduced in Figure 6.13. The second value is much higher than the expected exponent of 0.4 expected for faceted films [127]. This result is consistent with our simulated measurements given the high amount of self-shadowing expected for LPCVD film growth.

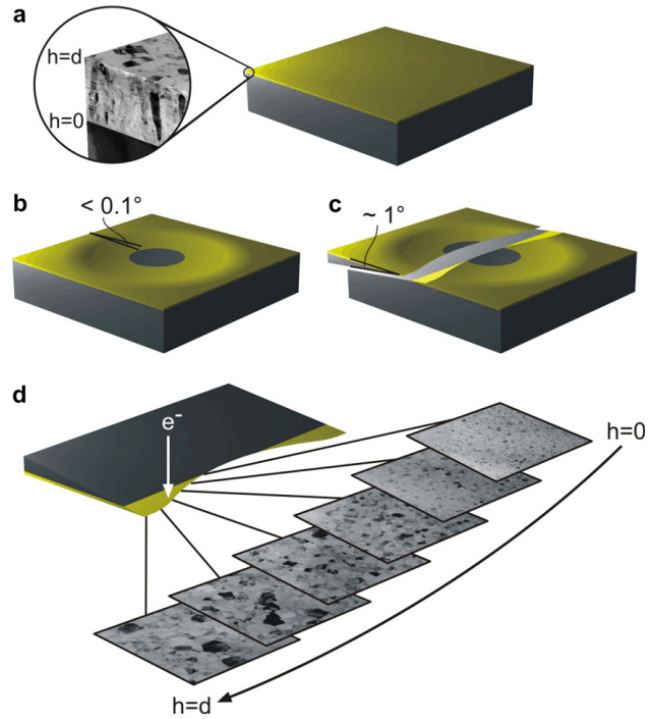


Figure 6.12: Double wedge sample preparation technique for cross-sectional samples created by Spiecker et al. The deposited film (a) is first dimpled hemispherically at a low angle (b). The sample is then tripod polished with a linear slope on the bottom (c). The resulting double-wedge then has electron transparent slices at various thicknesses. These thicknesses are measured optically using an interference technique.

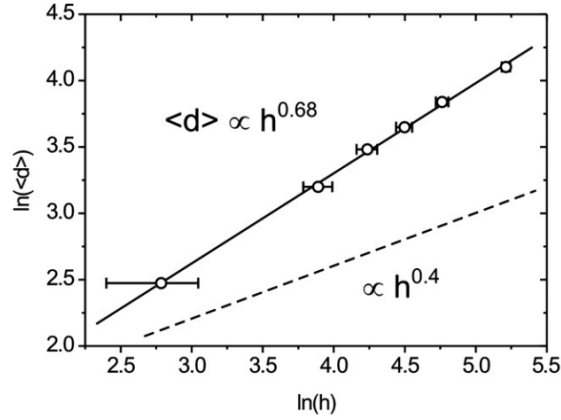


Figure 6.13: Measured mean grain diameter versus grain thickness for SiC growth by LPCVD, taken from Spiecker et al. The expected power for non-self-shadowed growth of 0.4 is also shown.

Yang et al. have measured anomalously high values for sputtered Cu films in the temperature regime where their films are columnar with well-defined boundaries [118]. For these films, they measured β values of $\simeq 0.36 - 0.65$. Fu and Shen have measured a global β of 0.56 for sputter deposited Al films [112]. Both of these studies are consistent with our simulations in the range of $2 < N < 5$. However, the range of values measured by Yang et al. as the temperature was varied could be due to the surface diffusion increasing beyond that of true faceted growth, or possibly a change in the kinetic Wulff shape of the Cu grains.

These results are also qualitatively very similar to those obtained by Yanguas-Gil et al. in their simulations of self-shadowed thin film growth without faceting. A comparison of our measured β values with their measured values (taken from [111]) is shown in Figure 6.14, using the relation $N = 2z^2$.

To understand why self-shadowing leads to higher magnitude power-law statistics, we must consider the distribution of grain heights present at a film surface. If N is very high, all grains receive approximately the same amount of flux per

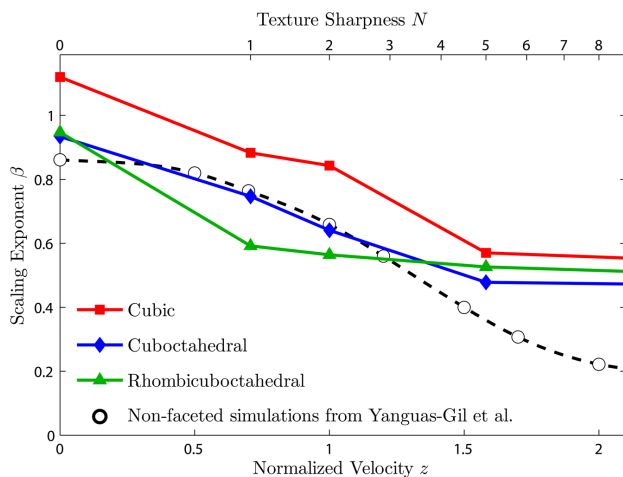


Figure 6.14: Comparison between scaling exponents measured in the current study of faceted film growth with those measured by Yanguas-Gil et al. for non-faceted film growth.

area. All grains therefore grow upwards at almost the same velocity. Shorter grains are swallowed when they collide with taller grains; this occurs because of the lateral movement of all grains, i.e. the component of grain movement perpendicular to the substrate normal (due to grain tilt, the stochastic nature of the incoming flux and the random surrounding environment). However, as N decreases more self-shadowing events occur. A feedback loop develops, where taller grains receive considerably more flux than shorter grains, increasing the separation of grain heights. The runaway growth of the best-positioned and tallest grains leads to them quickly dominating the surface, which is clearly demonstrated in Figure 6.7. This type of film typically suffers from high levels of porosity and high surface roughness, two properties undesirable for most thin film applications.

Finally, we return to the dependence of the scaling exponent on the local length scale. The measured β values from the simulations are plotted in Figure 6.15 for several N values. The trends are similar for all N values, with nearly the

same β values at low l for each of them. These low l values are somewhat lower than comparable measurements of the Al films in Figure 6.2. The most likely reason for this discrepancy is that the film surfaces in Figure 6.1 are not perfectly faceted. The rounded edges may be the actual film surface, or some of the local structure could have been smoothed out by the AFM tip used to capture the heightmap. Another possibility is that the films were not yet in true late-stage growth at the thicknesses used. At large length scales, the measured β values and simulations agree for $1 < N < 3$, which is the amount of self-shadowing expected for sputtering.

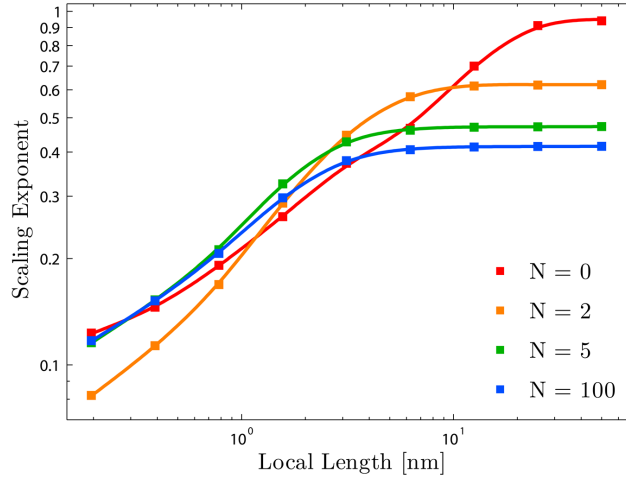


Figure 6.15: Measured scaling exponents of self-shadowing simulations with different N values measured over different length scales. Curves are drawn as guides for the eye.

6.4.5 Model Limitations and Applicability

The model proposed in this study is not universal, due the enormous complexity of competing factors during film growth. The material deposited changes the results only in specifying which facets form and which do not. For example, cubic fcc materials such as Au typically form $\{001\}$ - and $\{111\}$ -type

facets [128], whereas a hexagonal material such as aluminum nitride can form $\{0001\}$ -, $\{10\bar{1}1\}$ - and $\{10\bar{1}0\}$ -type facets [123]. Other effects not accounted for include how temperature and deposition rate modify a polycrystalline film's morphology by changing the kinetic energy of adatoms on the film surface. In this study, we have used a simple diffusion model where we assume adatom diffusion is high enough to form flat facets, but too low for material exchange between facets. Therefore the model is only valid in the regime of temperatures and deposition rates which are consistent with our assumptions. Our results do explain the dependence of both local and global scaling laws on kinetic Wulff shape and the degree of self-shadowing of the atomic flux; however they should only be applied quantitatively to films that are close to ideally faceted where the facets present are known.

6.5 Summary

We have simulated faceted polycrystalline thin film growth with ballistically deposited atomic flux, where the sharpness of the angular flux distribution is estimated by a cosine distribution to the N^{th} power. These simulations correspond to deposition techniques including low pressure chemical vapor deposition ($N = 0$), sputtering ($1 < N < 3$), pulsed laser deposition ($2 < N < 20$) and evaporation ($N > 100$). We have assumed a constant initial grain nuclei spacing and a uniform initial angular distribution, and have demonstrated the morphology dependence on N for several grain geometries.

As the incoming atom angles move further from the substrate normal (decreasing N), there is a greater chance of grains on the surface of a thin film preventing flux from colliding with other grains. This self-shadowing strongly modifies the film surface. A higher number of shadowing events causes favourably oriented grains to more quickly subsume their neighbors and grow to large sizes. This means that at a given thickness, grain survival probability is lower and

RMS surface roughness is higher. Large amounts of self-shadowing can also cause porosity throughout the film thickness, if enough different low-index crystallographic facets are present to allow formation of vertical channels in the film surface.

The film textures in our simulations are different than those found in simulations without ballistic deposition. These textures are mostly independent of the N value, but do depend on which crystallographic facets are present. In late-stage growth, cubic geometries produced a mix of $\langle 111 \rangle$ and $\langle 110 \rangle$ texture. Octahedral and cuboctahedral geometries evolved towards a $\langle 100 \rangle$ fiber texture. These textures are different from those predicted by previous simulations where grain facet velocity depended only on their crystallographic orientation.

Lastly we have measured the scaling exponents for grain survival probability and RMS surface roughness. The global scaling exponent β asymptotically approaches a value of 0.4 for high N values, a value predicted by analytic models of polycrystalline grain growth such as [94] or the one in Chapter 4. The scaling exponent increased beyond 0.4 as $N \rightarrow 0$. The probability of survival exponent increased from approximately -1.7 at $N = 0$ to approximately -0.5 for large values of N . These measured exponents did not match the exponents predicted by the analytic models of -0.8 . However, the simulations with $N = 2$ had a global scaling exponent very similar to those of the sputtered Al films. The qualitative behaviour of the scaling exponent as the length scale was decreased was similar, though with lower values measured in simulation than experiment. New analytic models will need to be developed to further understanding of the role of self-shadowing in polycrystalline thin film growth.

7

Conclusions

7.1 Thesis Summary

7.1.1 Part I

In the first half of this thesis, Chapters 2 and 3, we designed a binary metallic alloy for nanoscale resonator applications. The alloy design requirements were:

- ▶ Simple to deposit and easy to etch chemically.
- ▶ Smooth surface and uniform microstructure.
- ▶ High conductivity and reflectivity.
- ▶ Low differential stress.

CHAPTER 7: CONCLUSIONS

We selected aluminum as the majority phase because it is already widely used in the microfabrication industry and possesses a simple chemical etch. We used co-sputtering to create alloy thin films of aluminum and molybdenum. Molybdenum is a refractory metal with a strong negative heat of mixing with aluminum. Because sputtering is a vapour deposition technique (extremely high cooling rates from the gas to the solid phase), none of the Al-Mo equilibrium intermetallics formed for any composition. Instead, the three phases formed (and predicted thermodynamically) were:

- ▶ A disordered FCC solid solution from 0 to 16 at.%Mo.
- ▶ A metallic glass from 12 to 55 at.%Mo.
- ▶ A disordered BCC solid solution from 45 to 100 at.%Mo.

Note that in the overlapping composition regimes, a two-phase structure was observed. By using SEM, TEM and AFM we fully characterize the various microstructures and surface structures of different Al-Mo compositions. Nanoin-dentation was used to investigate the hardness and modulus of our films and four point probe measurements were taken to assess the conductivity. From these results we selected Al-32 at.%Mo as the optimum composition because of its smooth surface, uniform microstructure, high hardness and acceptable conductivity.

We then fabricated proof of principle resonators from thin films of Al-32 at.%Mo. The resonant properties of these devices were characterized with an optical interferometer. The devices were flat enough for optical readout, demonstrating that the differential stress of the deposition was at a tolerable level. The frequency responses of these resonators agreed with mechanical vibration theory and the quality factors were measured to fall between 50 and 500. These quality factors are far higher than possible with electronic circuitry but still lower than devices of similar dimensions fabricated from semiconducting films. However, because our devices are completely metal-

lic, they have much higher reflectivity and conductivity than is possible with uncoated semiconductor devices.

7.1.2 Part II

In the second half of this thesis, Chapters 4 and 5, we derived an analytic growth model for competitive growth of faceted polycrystalline thin films and then used simulations to confirm our model's accuracy. The assumptions used to derive this model made it applicable primarily to chemical vapor deposition. The simulations were then extended with a ballistic deposition model in Chapter 6 to allow us to simulate faceted polycrystalline films deposited by techniques such as sputtering, evaporation, low pressure chemical vapor deposition and pulsed laser deposition.

The mechanisms of competitive grain growth and the morphological statistics of the analytic model and the simulations were analyzed in detail. In particular the relationship between grain geometry and the angular deposition flux distribution with statistics such as RMS surface roughness, grain diameter and probability of grain survival were explored. For chemical vapour growth, we gave an explicit equation for the crossover thickness into late-stage growth. The ballistic deposition simulations produced surfaces very similar to the polycrystalline compositions of Al–Mo in Chapter 2. In the AFM slopemaps of Figure 2.8 and the structure zone map of Figure 2.11 surfaces created by competitive grain growth are evident at high and low Mo concentrations. The simulations provide a partial explanation for many of the morphological features observed.

The model and simulations used an extremely simple diffusion model. Nucleation was also neglected in favour of late-stage growth. All film morphological statistics depend on the initial mean grain spacing, which we used as an initial condition rather than analyzing directly. However, by narrowing our focus we were able to analyze self-shadowing in great detail and show how it plays a

dominant role in shaping the structure of faceted polycrystalline films.

7.2 Future Work

7.2.1 Part I

The next logical step in our studies on Al–Mo would be to produce actual devices from our optimized alloy. Some applications require high levels of conductivity and reflectivity, the primary advantage of using a metal rather than a semiconductor. An example is a resonator that needs to operate over a wide temperature range. A two-layer device such as a metal-coated semiconductor is subject to curling due to different thermal expansion coefficients of the layers.

The same design route used for Al–Mo can also be used to design other alloys for similar applications. The characteriation techniques employed in this work are a good general framework to optimize any deposition paramter including temperature, pressure, deposition rate or composition.

7.2.2 Part II

The simulations of this thesis can be extended in several ways. The biggest gains could probably be realized by including diffusion in the simulations. By comprehensively treating adatom diffusion over facet surfaces and mass exchange between adjacent facets, the usefulness of the simulations would increase dramatically. Variables such as temperature could then be varied in conjunction with the simulation input parameters already included. A better model could also be used for the angular deposition flux, that better accounted for the local environment above the polycrystalline film surface. Resputtering

CHAPTER 7: CONCLUSIONS

of the film surface could also be included. A more fundamental change would be to allow new facets to form based on the local diffusional environment on a grain surface. Pores and trenches on the film surface especially would benefit from a more comprehensive geometric grain model.

In addition to methodology improvements, these simulations should also be applied to analysis of real growth systems. Techniques such as double-wedge TEM sample preparation or focused ion beam slicing of a thin film allow for a detailed analysis of almost any polycrystalline thin film. The measured statistics and grain geometries could then be compared directly to those generated by the model. This would allow for quantitative analysis of the effects included in the simulations such as self-shadowing and would identify areas where we have oversimplified the growth model or made unjustifiable assumptions.

A

Appendix: Statistical Derivations

A.1 Initial Texture Distributions

In Chapter 4 the orientation distribution functions (ODF) $g(\theta, \phi)$, were constructed using the following equation

$$g(\theta, \phi) = \frac{2N + 1}{4\pi \left(\sum_{i=1}^P w_i \right)} \sum_{i=1}^P w_i |\hat{\mathbf{u}}_i \cdot \hat{\mathbf{r}}(\theta, \phi)|^{2N} \quad (\text{A.1.1})$$

where $\hat{\mathbf{u}}_i$ is a unit vector in the direction of the i^{th} pole, $\hat{\mathbf{r}}(\theta, \phi)$ is the unit position vector in spherical coordinates, w_i is the relative weighting of the i^{th} pole, P is the total number of poles and N determines the degree of texturing. Note that this expression assumes an equal weighting of each pole and its

APPENDIX A: STATISTICAL DERIVATIONS

antiparallel direction; therefore there is no need to specify both $\hat{\mathbf{u}}_i$ and $-\hat{\mathbf{u}}_i$ for any given i . The $\langle 111 \rangle$ -oriented ODF is constructed using all four $\langle 111 \rangle$ directions ($\hat{\mathbf{u}}_i$) with equal weighting (w_i) and $N=8$. The $\langle 001 \rangle$ oriented ODF is constructed using all three $\langle 001 \rangle$ directions with equal weighting and $N=8$. The uniform ODF is constructed using a single pole with $N=0$.

The N parameter is used to control the sharpness of the texture. When $N=0$ the distribution has random texture, as N is increased the texture becomes progressively sharper. The N parameter can be directly related to more commonly used metrics to describe the degree of texture, such as the texture index J ,

$$J = 4\pi \sum_{l=0}^{\infty} \sum_{m=-l}^{m=l} |Q_l^m|^2 \quad (\text{A.1.2})$$

where Q_l^m are the Fourier coefficients of the spherical harmonic expansion of the ODF. For a uniform texture distribution $J=1$ and as the texture sharpens J takes on larger values. Applying Parseval's theorem, the texture factor can be expressed equivalently as

$$J = 4\pi \int_0^{2\pi} \int_0^{\pi} g^2(\theta, \phi) \sin \theta \, d\theta \, d\phi \quad (\text{A.1.3})$$

Using equations [A.1.1](#) and [A.1.3](#) an exact expression for the texture index can be derived for an ODF consisting of $\langle 001 \rangle$ poles, given by

$$J = \left(1 + \frac{4N^2}{4N+1}\right) \frac{\sum_{ij} w_i w_j \left[\delta_{ij} + (1 - \delta_{ij}) \frac{2\Gamma^2(N+1/2)}{\sqrt{\pi}\Gamma(2N+1/2)} \right]}{(\sum w_i)^2} \quad (\text{A.1.4})$$

As N is increased beyond unity the second term within the brackets exponentially approaches zero, giving the following relation

$$J \simeq (N+1) \frac{\sum w_i^2}{(\sum w_i)^2} \quad (\text{A.1.5})$$

Moreover, it can be shown that equation [A.1.5](#) is valid for any number of poles pointing in arbitrary directions provided that N is sufficiently large.

A.2 Thin Film Statistical Relationships

The connection between different statistical measurements is explicitly explained in this appendix. The expectation value for grain diameter at a given thickness in the limit where all surviving grains have a fastest growth direction close to perpendicular to the substrate and the same pyramidal geometry (late-stage growth) is

$$\langle d \rangle = \left(\frac{t}{\tau} \right)^{2/5} \quad (\text{A.2.1})$$

We have defined grain diameter as the square root of grain area projected into the substrate plane. From this definition the expectation value of grain area is

$$\langle A \rangle = \left(\frac{t}{\tau} \right)^{4/5} \quad (\text{A.2.2})$$

Note that with this definition of mean grain diameter, the average diameter is found from the area-weighted distribution of diameters. Because we have normalized all grain areas by A_0 , every grain begins with an area of one. The probability of grain survival is therefore just the inverse of Equation [A.2.2](#)

$$P = \left(\frac{t}{\tau} \right)^{-4/5} \quad (\text{A.2.3})$$

The above derivations are straight-forward because in late stage growth each can be computed with a mean-field approach; more precisely by neglecting the local environment of each grain. However, in the calculation of RMS roughness of the film surface the local spatial configuration of the grains cannot be neglected; for a faceted surface, the greater the distance between a grain and its neighbor, the greater the contribution to surface roughness. Thus the prefactor term for a surface roughness scaling law must contain a correction term to account for the local spatial correlation of the grains.

To derive the RMS roughness correction factor we again use Thijssen's assumptions of cone-shaped grains. During growth, all grains asymptote towards the

APPENDIX A: STATISTICAL DERIVATIONS

same orientation where the fastest growth direction is perpendicular to the substrate. All surviving cone tops in late-stage growth will have the same surface slope m , and the tops will be uniformly and randomly distributed with density ρ . Assuming all cone peaks are at the same height, the height of the surface at any point $\vec{r}(x, y)$ is

$$h(\vec{r}) = m |\vec{r} - \vec{r}_{c,\min}| \quad (\text{A.2.4})$$

Where $\vec{r}_{c,\min}$ is the position of the cone vertex closest to point \vec{r} . Given the probability distribution $f(r, \rho)$ that a point is located a distance r from the nearest cone vertex the RMS roughness σ squared is

$$\begin{aligned} \sigma^2 &= \frac{\iint_A [h(\vec{r}) - \langle h \rangle]^2 dA}{\iint_A dA} \\ &= m^2 \int_0^\infty [rf(r, \rho) - \langle r \rangle]^2 \\ &= m^2 [\langle r^2 \rangle - \langle r \rangle^2] \end{aligned} \quad (\text{A.2.5})$$

Where $\langle r^2 \rangle$ and $\langle r \rangle$ denote expectation values. The required probability distribution can be constructed as follows. In a uniform distribution of N random points (or cone top vertices) of density ρ , the probability P that an arbitrarily placed disk of radius r contains k points is binomially distributed

$$P_k(r) = \left[\frac{N!}{k!(N-k)!} \right] \left[\frac{\pi r^2 \rho}{N} \right]^k \left[1 - \frac{\pi r^2 \rho}{N} \right]^{N-k} \quad (\text{A.2.6})$$

Noting that the probability that such a disk contains at least one or more points is the sum of probabilities that at a point is located at a distance x , where $x \leq r$, we arrive an expression for the probability distribution $f(r, \rho)$

$$\begin{aligned} \int_0^r f(r, \rho) dx &= \sum_{k=1}^\infty P_k(r) \\ &= 1 - P_0(r) \end{aligned} \quad (\text{A.2.7})$$

APPENDIX A: STATISTICAL DERIVATIONS

In the limit of a large number of points

$$\lim_{N \rightarrow \infty} P_0(r) = \exp(-\pi r^2 \rho) \quad (\text{A.2.8})$$

Upon differentiation a final expression for the desired probability distribution is obtained

$$f(r, \rho) = 2\pi r \rho \exp(-\pi r^2 \rho) \quad (\text{A.2.9})$$

It is worth noting that this distribution is identical to the distribution of nearest neighbor spacing of a Poisson distribution of points [129], since they are equivalent problems in the limit of large N . To check the validity of this expression we generated a random distribution of points in a periodic 2D field. We then overlaid a square grid and computed at each grid location the distance to the nearest random point. The resulting probability distribution of distance to the nearest point is shown in Figure A.1 for several point densities (relative to the density of the grid), with the theoretical expression from Equation A.2.9 superimposed. We see that the fit is exceptional and there are no fitting parameters as the density is exactly measured from the simulation of random points.

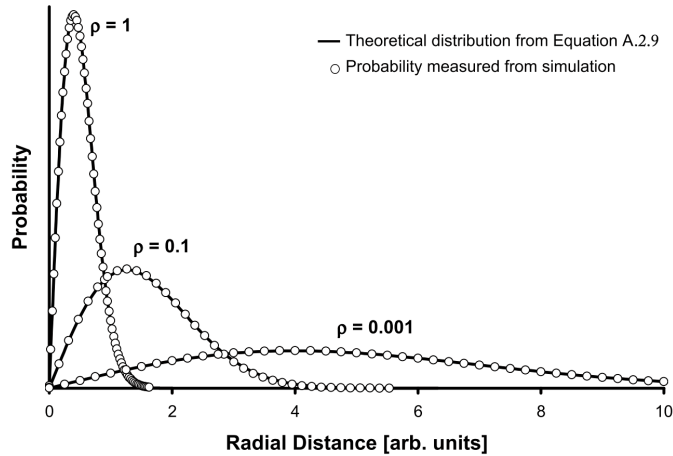


Figure A.1: Probability distribution of distances to nearest random point on a periodic 2D surface for different point densities.

APPENDIX A: STATISTICAL DERIVATIONS

Computing the first and second moment of Equation A.2.9, an expression for the RMS roughness of a random distribution of cone-shaped grains is obtained

$$\begin{aligned}\langle r \rangle &= \frac{1}{2\sqrt{\rho}} \\ \langle r^2 \rangle &= \frac{1}{\pi\rho} \\ \sigma &= \sqrt{\frac{1}{\pi} - \frac{1}{4}\frac{m}{\sqrt{\rho}}}\end{aligned}\tag{A.2.10}$$

Finally, we note that the slope m of an equivalent cone surface (shown in Figure 5.3) can be computed from the same geometric relationship described above for pyramid crystal tops as

$$m = \sqrt{\pi} \frac{l}{\sqrt{A}}\tag{A.2.11}$$

Combining Equations A.2.10 and A.2.11 and assuming that density ρ is equal to the probability of cone top survival P given by Equation A.2.3 yields the expression for RMS roughness

$$\sigma = \sqrt{1 - \frac{\pi}{4} \frac{l}{\sqrt{A}} \left(\frac{t}{\tau}\right)^{2/5}}\tag{A.2.12}$$

Now we convert from the τ prefactor notation used here and in Chapters 4 and 6 to the prefactor notation of Chapter 5. The relationships between the prefactors of Equations 5.3.1–5.3.4 and τ are

$$d_\infty = \tau^{-2/5}\tag{A.2.13}$$

$$P_\infty = \tau^{4/5}\tag{A.2.14}$$

$$A_\infty = \tau^{-4/5}\tag{A.2.15}$$

$$\sigma_\infty = \sqrt{1 - \frac{\pi}{4} \frac{l}{\sqrt{A}}} \tau^{-2/5}\tag{A.2.16}$$

References

- [1] B Lüssem, S Karthäuser, H Haselier, and R Waser. The origin of faceting of ultraflat gold films epitaxially grown on mica. *Applied Surface Science*, 249 (1-4):197–202, 2005. URL [dx.doi.org/10.1016/j.apsusc.2004.11.082](https://doi.org/10.1016/j.apsusc.2004.11.082).
- [2] A Goetzberger, J Luther, and G Willeke. Solar cells: past, present, future. *Solar energy materials and solar cells*, 74(1):1–11, 2002. URL [dx.doi.org/10.1016/S0927-0248\(02\)00042-9](https://doi.org/10.1016/S0927-0248(02)00042-9).
- [3] P Caron and T Khan. Evolution of Ni-based superalloys for single crystal gas turbine blade applications. *Aerospace Science and Technology*, 3(8):513–523, 1999. URL [dx.doi.org/10.1016/S1270-9638\(99\)00108-X](https://doi.org/10.1016/S1270-9638(99)00108-X).
- [4] E Arzt. Overview no. 130 - Size effects in materials due to microstructural and dimensional constraints: A comparative review. *Acta Materialia*, 46(16): 5611–5626, 1998. URL [dx.doi.org/10.1016/S1359-6454\(98\)00231-6](https://doi.org/10.1016/S1359-6454(98)00231-6).
- [5] H Kim, Y Xuan, PD Ye, R Narayanan, and AH King. Anomalous triple junction surface pits in nanocrystalline zirconia thin films and their relationship to triple junction energy. *Acta Materialia*, 57(12):3662 – 3670, 2009. URL [dx.doi.org/10.1016/j.actamat.2009.04.032](https://doi.org/10.1016/j.actamat.2009.04.032).
- [6] F Greuter and G Blatter. Electrical properties of grain boundaries in polycrystalline compound semiconductors. *Semiconductor Science and Technology*, 5 (2):111–137, 1990. URL [dx.doi.org/10.1088/0268-1242/5/2/001](https://doi.org/10.1088/0268-1242/5/2/001).
- [7] MA Khan, TP Comyn, and AJ Bell. Growth and characterization of tetragonal bismuth ferrite–lead titanate thin films. *Acta Materialia*, 56(9):2110–2118, 2008. URL [dx.doi.org/10.1016/j.actamat.2008.01.008](https://doi.org/10.1016/j.actamat.2008.01.008).

REFERENCES

- [8] KE Goodson and YS Ju. Heat conduction in novel electronic films. *Annual Review of Materials Science*, 29:261–293, 1999. URL [dx.doi.org/10.1146/annurev.matsci.29.1.261](https://doi.org/10.1146/annurev.matsci.29.1.261).
- [9] S Uma, AD McConnell, M Asheghi, K Kurabayashi, and KE Goodson. Temperature-dependent thermal conductivity of undoped polycrystalline silicon layers. *International Journal of Thermophysics*, 22(2):605–616, 2001. URL [dx.doi.org/10.1023/A:1010791302387](https://doi.org/10.1023/A:1010791302387).
- [10] I Petrov, PB Barna, L Hultman, and JE Green. Microstructural evolution during film growth. *Journal of Vacuum Science & Technology A*, 21:S117–S128, 2003. URL [dx.doi.org/10.1116/1.1601610](https://doi.org/10.1116/1.1601610).
- [11] C Wild, N Herres, and P Koidl. Texture Formation in Polycrystalline Diamond Films. *Journal of Applied Physics*, 68(3):973–978, 1990. URL [dx.doi.org/10.1063/1.346663](https://doi.org/10.1063/1.346663).
- [12] H Huang, GH Gilmer, and T Diaz de la Rubia. An atomistic simulator for thin film deposition in three dimensions. *Journal of Applied Physics*, 84(7):3636–3649, 1998. URL [dx.doi.org/10.1063/1.368539](https://doi.org/10.1063/1.368539).
- [13] N.Q. Lam, P.R. Okamoto, and M. Li. Disorder-induced amorphization. *Journal of Nuclear Materials*, 251:89–97, 1997. URL [dx.doi.org/10.1016/S0022-3115\(97\)00257-2](https://doi.org/10.1016/S0022-3115(97)00257-2).
- [14] H Van Swygenhoven, D Farkas, and A Caro. Grain-boundary structures in polycrystalline metals at the nanoscale. *Physical Review B*, 62(2):831–838, 2000. URL [dx.doi.org/10.1103/PhysRevB.62.831](https://doi.org/10.1103/PhysRevB.62.831).
- [15] I Safi. Recent aspects concerning dc reactive magnetron sputtering of thin films: a review. *Surface & Coatings Technology*, 127(2-3):203–218, 2000. URL [dx.doi.org/10.1116/1.574104](https://doi.org/10.1116/1.574104).
- [16] M Birkholz, PF Fewster, and C Genzel. *Thin film analysis by x-ray scattering*. Wiley-VCH, 2006. URL www.amazon.ca/gp/search?index=books&keywords=3527310525.

REFERENCES

- [17] DB Williams and CB Carter. *Transmission electron microscopy: a textbook for materials science*. Springer Verlag, 2009. URL www.amazon.com/Transmission-Electron-Microscopy-Textbook-Materials/dp/030645324X.
- [18] KCA Smith and CW Oatley. The scanning electron microscope and its fields of application. *British Journal of Applied Physics*, 6:391–399, 1955. URL dx.doi.org/10.1088/0508-3443/6/11/304.
- [19] RE Van Grieken and AA Markowicz. *Handbook of x-ray spectrometry: methods and techniques*. Marcel Dekker, New York, NY, 1993. URL www.amazon.com/Handbook-X-Ray-Spectrometry-Techniques-Spectroscopy/dp/0824784839.
- [20] D Rugar and P Hansma. Atomic force microscopy. *Physics Today*, 43(10):23–30, 1990. URL dx.doi.org/10.1063/1.881238.
- [21] WC Oliver and HM Pharr. Measurement of hardness and elastic modulus by instrumented indentation: advances in understanding and refinements to methodology. *Journal of Materials Research*, 19(3), 2004. URL dx.doi.org/10.1557/JMR.2004.0002.
- [22] WK Liu, EG Karpov, S Zhang, and HS Park. An introduction to computational nanomechanics and materials. *Computer Methods in Applied Mechanics and Engineering*, 193(17-20):1529–1578, 2004. URL dx.doi.org/10.1016/j.cma.2003.12.008.
- [23] TE Karakasidis and CA Charitidis. Multiscale modeling in nanomaterials science. *Materials Science & Engineering C*, 27(5-8):1082–1089, 2007. URL dx.doi.org/10.1016/j.msec.2006.06.029.
- [24] PM Derlet and SL Dudarev. Million-atom molecular dynamics simulations of magnetic iron. *Progress in Materials Science*, 52(2-3):299–318, 2007. URL dx.doi.org/10.1016/j.pmatsci.2006.10.011.
- [25] P Smereka, X Li, G Russo, and DJ Srolovitz. Simulation of faceted film

REFERENCES

- growth in three dimensions: microstructure, morphology and texture. *Acta Materialia*, 53(4):1191 – 1204, 2005. URL [dx.doi.org/10.1016/j.actamat.2004.11.013](https://doi.org/10.1016/j.actamat.2004.11.013).
- [26] M Roukes. Nanoelectromechanical systems face the future. *Phys. World*, 14: 25–31, 2001. URL physicsworld.com/cws/article/print/293.
- [27] AHM Meyer. Publications and patents in nanotechnology An overview of previous studies and the state of the art. *Scientometrics*, 58(3), 2003. URL [dx.doi.org/10.1023/B:SCIE.0000006877.45467.a7](https://doi.org/10.1023/B:SCIE.0000006877.45467.a7).
- [28] KL Ekinici and ML Roukes. Nanoelectromechanical systems. *Review of Scientific Instruments*, 76:061101, 2005. URL [dx.doi.org/10.1063/1.1927327](https://doi.org/10.1063/1.1927327).
- [29] JS Pulskamp, A Wickenden, R Polcawich, B Piekarski, M Dubey, and G Smith. Mitigation of residual film stress deformation in multilayer microelectromechanical systems cantilever devices. *Journal of Vacuum Science & Technology B: Microelectronics and Nanometer Structures*, 21:2482, 2003. URL [dx.doi.org/10.1116/1.1615982](https://doi.org/10.1116/1.1615982).
- [30] R Sandberg, K Mølhave, A Boisen, and W Svendsen. Effect of gold coating on the Q-factor of a resonant cantilever. *Journal of Micromechanics and Microengineering*, 15:2249–2253, 2005. URL [dx.doi.org/10.1088/0960-1317/15/12/006](https://doi.org/10.1088/0960-1317/15/12/006).
- [31] CL Muhlstein, EA Stach, and RO Ritchie. A reaction-layer mechanism for the delayed failure of micron-scale polycrystalline silicon structural films subjected to high-cycle fatigue loading. *Acta materialia*, 50(14):3579–3595, 2002. URL [dx.doi.org/10.1016/S1359-6454\(02\)00158-1](https://doi.org/10.1016/S1359-6454(02)00158-1).
- [32] R Langer and DA Tirrell. Designing materials for biology and medicine. *Nature*, 428(6982):487–492, 2004. URL [dx.doi.org/10.1038/nature02388](https://doi.org/10.1038/nature02388).
- [33] AS Arico, P Bruce, B Scrosati, JM Tarascon, and W Van Schalkwijk. Nanostructured materials for advanced energy conversion and storage devices. *Nature Materials*, 4(5):366–377, 2005. URL [dx.doi.org/10.1038/nmat1368](https://doi.org/10.1038/nmat1368).

REFERENCES

- [34] DW Hoffman and JA Thornton. The compressive stress transition in Al, V, Zr, Nb and W metal films sputtered at low working pressures. *Thin Solid Films*, 45(2):387–396, 1977. URL [dx.doi.org/10.1016/0040-6090\(77\)90276-0](https://doi.org/10.1016/0040-6090(77)90276-0).
- [35] ZJ Davis and A Boisen. Aluminum nanocantilevers for high sensitivity mass sensors. *Applied Physics Letters*, 87:013102, 2005. URL [dx.doi.org/10.1063/1.1984092](https://doi.org/10.1063/1.1984092).
- [36] A Almeida, F Carvalho, PA Carvalho, and R Vilar. Laser developed Al–Mo surface alloys: Microstructure, mechanical and wear behaviour. *Surface & Coatings Technology*, 200(16-17):4782–4790, 2006. URL [dx.doi.org/10.1016/j.surfcoat.2005.04.045](https://doi.org/10.1016/j.surfcoat.2005.04.045).
- [37] M Bielawski. Development of unbalanced magnetron sputtered Al–Mo coatings for cadmium replacement. *Surface & Coatings Technology*, 179(1):10–17, 2004. URL [dx.doi.org/10.1016/S0257-8972\(03\)00796-5](https://doi.org/10.1016/S0257-8972(03)00796-5).
- [38] N Saunders. The Al–Mo system (aluminum-molybdenum). *Journal of Phase Equilibria and Diffusion*, 18(4):370–378, 1997. URL [dx.doi.org/10.1007/s11669-997-0063-1](https://doi.org/10.1007/s11669-997-0063-1).
- [39] I Shilo and HE Franzen. High temperature thermodynamic study of the Mo-rich regions of the Mo–Al system. *Journal of the Electrochemical Society*, 129:2613–2617, 1982. URL [dx.doi.org/10.1149/1.2123630](https://doi.org/10.1149/1.2123630).
- [40] Z Du, C Guo, C Li, and W Zhang. Thermodynamic Description of the Al–Mo and Al–Fe–Mo Systems. *Journal of Phase Equilibria and Diffusion*, 30(5):487–501, 2009. URL [dx.doi.org/10.1007/s11669-009-9564-4](https://doi.org/10.1007/s11669-009-9564-4).
- [41] JH Perepezko. Nucleation controlled phase selection during solidification. *Materials Science & Engineering A*, 413:389–397, 2005. URL [dx.doi.org/10.1016/j.msea.2005.08.155](https://doi.org/10.1016/j.msea.2005.08.155).
- [42] N Saunders and AP Miodownik. Calphad (calculation of phase diagrams): a comprehensive guide. 1, 1998. URL books.google.ca/books?id=CrdoHUZ4_5QC&dq.

REFERENCES

- [43] R Coehoorn, GJ Van der Kolk, JJ Van den Broek, T Minemura, and AR Miedema. Thermodynamics of the stability of amorphous alloys of two transition metals. *Journal of the less-common metals*, 140:307–316, 1988. URL [dx.doi.org/10.1016/0022-5088\(88\)90391-8](https://doi.org/10.1016/0022-5088(88)90391-8).
- [44] GJ Van der Kolk, AR Miedema, and AK Niessen. On the composition range of amorphous binary transition metal alloys. *Journal of the Less Common Metals*, 145:1–17, 1988. URL [dx.doi.org/10.1016/0022-5088\(88\)90257-3](https://doi.org/10.1016/0022-5088(88)90257-3).
- [45] RH de Tandler, JA Kovacs, and JA Alonso. Theoretical calculation of the amorphous alloy range of the Mg–Cu system. *Journal of Materials Science*, 27(18):4935–4939, 1992. URL [dx.doi.org/10.1007/BF01105256](https://doi.org/10.1007/BF01105256).
- [46] PI Loeff, AW Weeber, and AR Miedema. Diagrams of formation enthalpies of amorphous alloys in comparison with the crystalline solid solution. *Journal of the less-common metals*, 140:299–305, 1988. URL [dx.doi.org/10.1016/0022-5088\(88\)90390-6](https://doi.org/10.1016/0022-5088(88)90390-6).
- [47] RH de Tandler, MR Soriano, ME Pepe, JA Kovacs, EE Vicente, and JA Alonso. Calculation of metastable free-energy diagrams and glass formation in the Mg–Cu–Y alloy and its boundary binaries using the Miedema model. *Intermetallics*, 14(3):297–307, 2006. URL [dx.doi.org/doi:10.1016/j.intermet.2005.06.008](https://doi.org/10.1016/j.intermet.2005.06.008).
- [48] LR Shaginyan, NV Britun, JG Han, and VR Shaginyan. Anomalously high surface temperature induced by condensation of atoms. *JETP letters*, 83(3):113–117, 2006. URL [dx.doi.org/10.1134/S0021364006030076](https://doi.org/10.1134/S0021364006030076).
- [49] E Benes, M Gröschl, W Burger, and M Schmid. Sensors based on piezoelectric resonators. *Sensors & Actuators: A. Physical*, 48(1):1–21, 1995. URL [dx.doi.org/10.1016/0924-4247\(95\)00846-2](https://doi.org/10.1016/0924-4247(95)00846-2).
- [50] I Jencic, MW Bench, IM Robertson, and MA Kirk. Electron-beam-induced crystallization of isolated amorphous regions in Si, Ge, GaP, and GaAs. *Journal of Applied Physics*, 78:974, 1995. URL [dx.doi.org/10.1063/1.360764](https://doi.org/10.1063/1.360764).

REFERENCES

- [51] L Ba, Y Qin, and Z Wu. Electron beam induced crystallization of a Ge–Au amorphous film. *Journal of Applied Physics*, 80:6170, 1996. URL [dx.doi.org/10.1063/1.363691](https://doi.org/10.1063/1.363691).
- [52] A Meldrum, LA Boatner, and RC Ewing. Electron-irradiation-induced nucleation and growth in amorphous LaPO₄, ScPO₄, and zircon. *Journal of Materials Research*, 12(7):1816–1827, 1997. URL [dx.doi.org/10.1557/JMR.1997.0250](https://doi.org/10.1557/JMR.1997.0250).
- [53] AV Tikhonravov, MK Trubetskov, AA Tikhonravov, and A Duparre. Effects of interface roughness on the spectral properties of thin films and multilayers. *Applied optics*, 42(25):5140–5148, 2003. URL [dx.doi.org/10.1364/AO.42.005140](https://doi.org/10.1364/AO.42.005140).
- [54] G Fishman and D Calecki. Surface-induced resistivity of ultrathin metallic films: A limit law. *Physical Review Letters*, 62(11):1302–1305, 1989. URL [dx.doi.org/10.1103/PhysRevLett.62.1302](https://doi.org/10.1103/PhysRevLett.62.1302).
- [55] F Elsholz E, Schöll, C Scharfenorth, G Seewald, HJ Eichler, and A Rosenfeld. Roughness evolution in thin-film growth of SiO and NbO. *Journal of Applied Physics*, 98:103516, 2005. URL [dx.doi.org/10.1063/1.2130521](https://doi.org/10.1063/1.2130521).
- [56] GH Gilmer, H Huang, and C Roland. Thin film deposition: fundamentals and modeling. *Computational Materials Science*, 12(4):354, 1998. URL [dx.doi.org/10.1016/S0927-0256\(98\)00022-6](https://doi.org/10.1016/S0927-0256(98)00022-6).
- [57] C Streng, K Samwer, and SG Mayr. Surface smoothing and pattern formation in the transient region of compositionally modulated amorphous metallic alloy films: Experiment versus theory. *Physical Review B*, 73(10):104107, 2006. URL [dx.doi.org/10.1103/PhysRevB.73.104107](https://doi.org/10.1103/PhysRevB.73.104107).
- [58] JA Thornton. The microstructure of sputter-deposited coatings. *Journal of Vacuum Science & Technology A: Vacuum, Surfaces, and Films*, 4:3059, 1986. URL [dx.doi.org/10.1116/1.573628](https://doi.org/10.1116/1.573628).
- [59] AB Bhatia and DE Thornton. Structural aspects of the electrical resistivity

REFERENCES

- of binary alloys. *Physical Review B*, 2(8):3004–3012, 1970. URL [dx.doi.org/10.1103/PhysRevB.2.3004](https://doi.org/10.1103/PhysRevB.2.3004).
- [60] E Lubber, R Mohammadi, C Ophus, Z Lee, N Nelson-Fitzpatrick K, Westra, S Evoy, U Dahmen, V Radmilovic, and D Mitlin. Tailoring the microstructure and surface morphology of metal thin films for nano-electromechanical systems applications. *Nanotechnology*, 19:125705, 2008. URL [dx.doi.org/10.1088/0957-4484/19/12/125705](https://doi.org/10.1088/0957-4484/19/12/125705).
- [61] RP Feynman. There’s plenty of room at the bottom. In *The annual meeting of the American Physical Society at the California Institute of Technology (Caltech, December 29th 1959)*. First published in *Caltech’s Engineering and Science*, 1960. URL www.zyvex.com/nanotech/feynman.html.
- [62] RP Feynman. Infinitesimal machinery. *Journal of Microelectromechanical Systems*, 2(1), 1993. URL [dx.doi.org/10.1109/84.232589](https://doi.org/10.1109/84.232589).
- [63] DK Fork, CL Chua, P Kim, and et al. Nano-spring arrays for high-density interconnect. 4176:226, 2000. URL [dx.doi.org/10.1117/12.395634](https://doi.org/10.1117/12.395634).
- [64] T Hantschel, L Wong, CL Chua, and DK Fork. Fabrication of highly conductive stressed-metal springs and their use as sliding-contact interconnects. *Microelectronic Engineering*, 67:690–695, 2003. URL [dx.doi.org/10.1016/S0167-9317\(03\)00174-6](https://doi.org/10.1016/S0167-9317(03)00174-6).
- [65] CH Huang, C Tsou, and TH Lai. High density out-of-plane microprobe array. *CoRR*, abs/0805.0911, 2008. URL <http://arxiv.org/abs/0805.0911>.
- [66] XL Feng, CJ White, A Hajimiri, and ML Roukes. A self-sustaining ultrahigh-frequency nanoelectromechanical oscillator. *Nature Nanotechnology*, 3(6):342–346, 2008. URL [dx.doi.org/10.1038/nnano.2008.125Letter](https://doi.org/10.1038/nnano.2008.125Letter).
- [67] R Sandberg, W Svendsen, K Mølhave, and A Boisen. Temperature and pressure dependence of resonance in multi-layer microcantilevers. *Journal of Micromechanics and Microengineering*, 15(8):1454–1458, 2005. URL [dx.doi.org/10.1088/0960-1317/15/8/011](https://doi.org/10.1088/0960-1317/15/8/011).

REFERENCES

- [68] KY Yasumura, TD Stowe, EM Chow, T Pfafman, TW Kenny, BC Stipe, and D Rugar. Quality factors in micron-and submicron-thick cantilevers. *Journal of microelectromechanical systems*, 9(1):117–125, 2000. URL [dx.doi.org/10.1109/84.825786](https://doi.org/10.1109/84.825786).
- [69] TV Roszhart. The effect of thermoelastic internal friction on the Q of micro-machined silicon resonators. *IEEE Solid-State Sensor and Actuator Workshop, 4th Technical Digest*, pages 13–16, 1990. URL [dx.doi.org/10.1109/SOLSEN.1990.109810](https://doi.org/10.1109/SOLSEN.1990.109810).
- [70] RB Bhiladvala and ZJ Wang. Effect of fluids on the Q factor and resonance frequency of oscillating micrometer and nanometer scale beams. *Physical Review E*, 69(3):36307, 2004. URL [dx.doi.org/10.1103/PhysRevE.69.036307](https://doi.org/10.1103/PhysRevE.69.036307).
- [71] M Bao, H Yang, H Yin, and Y Sun. Energy transfer model for squeeze-film air damping in low vacuum. *Journal of Micromechanics and Microengineering*, 12:341–346, 2002. URL [dx.doi.org/10.1088/0960-1317/12/3/322](https://doi.org/10.1088/0960-1317/12/3/322).
- [72] J Yang, T Ono, and M Esashi. Energy dissipation in submicrometer thick single-crystal silicon cantilevers. *Journal of Microelectromechanical Systems*, 11(6):775–783, 2002. URL [dx.doi.org/10.1109/JMEMS.2002.805208](https://doi.org/10.1109/JMEMS.2002.805208).
- [73] A Wolfenden. Measurement and analysis of elastic and anelastic properties of alumina and silicon carbide. *Journal of Materials Science*, 32(9):2275–2282, 1997. URL [dx.doi.org/10.1023/A:1018524200517](https://doi.org/10.1023/A:1018524200517).
- [74] M Fukuhara and I Yamauchi. Temperature dependence of the elastic moduli, dilational and shear internal frictions and acoustic wave velocity for alumina,(Y) TZP and β^{\prime} -sialon ceramics. *Journal of Materials Science*, 28(17):4681–4688, 1993. URL [dx.doi.org/10.1007/BF00414258](https://doi.org/10.1007/BF00414258).
- [75] C Ophus, NN Fitzpatrick, Z Lee, E Lubber, C Harrower, K Westra, U Dahmen, V Radmilovic, S Evoy, and D Mitlin. Resonance properties and microstructure of ultracompliant metallic nanoelectromechanical systems resonators synthesized from Al–32 at.% Mo amorphous-nanocrystalline metallic

REFERENCES

- composites. *Applied Physics Letters*, 92:123108, 2008. URL [dx.doi.org/10.1063/1.2841849](https://doi.org/10.1063/1.2841849).
- [76] I Bargatin, EB Myers, J Arlett, B Gudlewski, and ML Roukes. Sensitive detection of nanomechanical motion using piezoresistive signal downmixing. *Applied Physics Letters*, 86:133109, 2005. URL [dx.doi.org/10.1063/1.1896103](https://doi.org/10.1063/1.1896103).
- [77] PA Truitt, JB Hertzberg, CC Huang, KL Ekinici, and KC Schwab. Efficient and sensitive capacitive readout of nanomechanical resonator arrays. *Nano Lett*, 7(1):120–126, 2007. URL [dx.doi.org/10.1021/nl062278g](https://doi.org/10.1021/nl062278g).
- [78] DW Carr, S Evoy, L Sekaric, HG Craighead, and JM Parpia. Measurement of mechanical resonance and losses in nanometer scale silicon wires. *Applied Physics Letters*, 75:920, 1999. URL [dx.doi.org/10.1063/1.124554](https://doi.org/10.1063/1.124554).
- [79] MS Hunter and P Fowle. Natural and thermally formed oxide films on aluminum. *Journal of the Electrochemical Society*, 103:482, 1956. URL [dx.doi.org/10.1149/1.2430389](https://doi.org/10.1149/1.2430389).
- [80] HR Wenk and P Van Houtte. Texture and anisotropy. *Reports on Progress in Physics*, 67(8):1367–1428, 2004. URL [dx.doi.org/10.1088/0034-4885/67/8/R02](https://doi.org/10.1088/0034-4885/67/8/R02).
- [81] V Cimalla, J Pezoldt, and O Ambacher. Group III nitride and SiC based MEMS and NEMS: materials properties, technology and applications. *Journal of Physics D: Applied Physics*, 40:6386–6434, 2007. URL [dx.doi.org/10.1088/0022-3727/40/20/S19](https://doi.org/10.1088/0022-3727/40/20/S19).
- [82] J Leib, R Monig, and CV Thompson. Direct evidence for effects of grain structure on reversible compressive deposition stresses in polycrystalline gold films. *Physical Review Letters*, 102(25):256101, 2009. URL [dx.doi.org/10.1103/PhysRevLett.102.256101](https://doi.org/10.1103/PhysRevLett.102.256101).
- [83] G Korotcenkov. The role of morphology and crystallographic structure of metal oxides in response of conductometric-type gas sensors. *Materials Science and Engineering: R: Reports*, 61(1-6):1 – 39, 2008. URL [dx.doi.org/10.1016/j.mser.2008.05.001](https://doi.org/10.1016/j.mser.2008.05.001).

REFERENCES

- [1016/j.mser.2008.02.001](#).
- [84] D Das and RN Singh. A review of nucleation, growth and low temperature synthesis of diamond thin films. *International Materials Reviews*, 52(1):29–64, 2007. URL [dx.doi.org/10.1179/174328007X160245](#).
- [85] Y Yan, R Noufi, and MM Al-Jassim. Grain-boundary physics in polycrystalline CuInSe_2 revisited: Experiment and theory. *Physical Review Letters*, 96(20):205501, 2006. URL [dx.doi.org/10.1103/PhysRevLett.96.205501](#).
- [86] AN Kolmogorov. On the statistical theory of the crystallization of metals. *Bulletin of the Academy of Sciences of the USSR, Physical Series*, 1:355–359, 1937. URL [scholar.google.ca/scholar?q=statistical+crystallization&as_yhi=1937](#).
- [87] A van der Drift. Evolutionary selection, a principle governing growth orientation in vapour-deposited layers. *Phillips Res Rep*, 22(3):267–288, 1967. URL [scholar.google.ca/scholar?q=evolutionary+selection&as_yhi=1967](#).
- [88] O Nilsen, OB Karlsen, A Kjekshus, and H Fjellvg. Simulation of growth dynamics for nearly epitaxial films. *Journal of Crystal Growth*, 308(2):366 – 375, 2007. URL [dx.doi.org/10.1016/j.jcrysgro.2007.08.001](#).
- [89] SA Norris and SJ Watson. Geometric simulation and surface statistics of coarsening faceted surfaces. *Acta Materialia*, 55(19):6444 – 6452, 2007. ISSN 1359-6454. URL [dx.doi.org/10.1016/j.actamat.2007.08.014](#).
- [90] C Ophus, EJ Lubber, and D Mitlin. Simulations of faceted polycrystalline thin films: Asymptotic analysis. *Acta Materialia*, 57(5):1327 – 1336, 2009. ISSN 1359-6454. URL [dx.doi.org/10.1016/j.actamat.2008.11.014](#).
- [91] E Spiecker, V Radmilovic, and U Dahmen. Quantitative TEM analysis of 3-D grain structure in CVD-grown SiC films using double-wedge geometry. *Acta Materialia*, 55(10):3521–3530, 2007. URL [dx.doi.org/10.1016/j.actamat.2007.01.051](#).

REFERENCES

- [92] C Lim, J Lee, and J Hanna. Nucleation and growth of poly-si films deposited directly on glass substrate in reactive thermal-chemical vapour deposition. *Thin Solid Films*, 517(8):2627 – 2632, 2009. ISSN 0040-6090. URL [dx.doi.org/10.1016/j.tsf.2008.10.061](https://doi.org/10.1016/j.tsf.2008.10.061).
- [93] MJ Rost. In situ real-time observation of thin film deposition: Roughening, zeno effect, grain boundary crossing barrier, and steering. *Physical Review Letters*, 99(26):266101, 2007. URL [dx.doi.org/10.1103/PhysRevLett.99.266101](https://doi.org/10.1103/PhysRevLett.99.266101).
- [94] JM Thijsen, HJF Knops, and AJ Dammers. Dynamic scaling in polycrystalline growth. *Physical Review B*, 45(15):8650–8656, 1992. URL [dx.doi.org/10.1103/PhysRevB.45.8650](https://doi.org/10.1103/PhysRevB.45.8650).
- [95] V Radmilovic, U Dahmen, D Gao, CR Stoldt, C Carraro, and R Maboudian. Formation of $\langle 111 \rangle$ fiber texture in β -SiC films deposited on Si(100) substrates. *Diamond and Related Materials*, 16(1):74 – 80, 2007. URL [dx.doi.org/10.1016/j.diamond.2006.03.017](https://doi.org/10.1016/j.diamond.2006.03.017).
- [96] AJ Dammers and S Radelaar. 2-dimensional computer modeling of polycrystalline growth. *Textures and Microstructures*, 14: 757–62, 1991. URL <http://scholar.google.ca/scholar?hl=en&q=2-Dimensional+polycrystalline+growth>.
- [97] C Wild, P Koidl, W Muller-Sebert, H Walcher, R Kohl, and N Herres. Chemical vapor deposition and characterization of smooth $\{100\}$ -faceted diamond films. *Diamond and Related Materials*, 2(2-4):158–68, 1993. URL [dx.doi.org/10.1016/0925-9635\(93\)90047-6](https://doi.org/10.1016/0925-9635(93)90047-6).
- [98] F Paritosh, DJ Srolovitz, CC Battaile, X Li, and JE Butler. Simulation of faceted film growth in two-dimension: microstructure morphology, and texture. *Acta Materialia*, 47(7):2269–2281, 1999. URL [dx.doi.org/10.1016/S1359-6454\(99\)00086-5](https://doi.org/10.1016/S1359-6454(99)00086-5).
- [99] JM Thijsen. Simulations of polycrystalline growth in 2+1 dimensions. *Physi-*

REFERENCES

- cal Review B*, 51(3):1985–1988, 1995. URL [dx.doi.org/10.1103/PhysRevB.51.1985](https://doi.org/10.1103/PhysRevB.51.1985).
- [100] S Kumar and SK Kurtz. Properties of a two-dimensional Poisson-Voronoi tessellation: a Monte-Carlo study. *Materials characterization*, 31(1):55–68, 1993. URL [dx.doi.org/10.1016/1044-5803\(93\)90045-W](https://doi.org/10.1016/1044-5803(93)90045-W).
- [101] Y Saito. Wulff polyhedra derived from Morse potentials and crystal habits of BCC and FCC metal particles. *Journal of Crystal Growth*, 53(2):273–279, 1981. URL [dx.doi.org/10.1016/0022-0248\(81\)90074-9](https://doi.org/10.1016/0022-0248(81)90074-9).
- [102] M Kotrla. Growth of rough surfaces. *Czechoslovak Journal of Physics*, 42(5):449–477, 1992. URL [dx.doi.org/10.1007/BF01605217](https://doi.org/10.1007/BF01605217).
- [103] F Family and T Vicsek. Dynamic scaling of growing interfaces. *Journal of Physics A: Mathematical and General*, 18:L75–L81, 1985. URL [dx.doi.org/10.1103/PhysRevLett.56.889](https://doi.org/10.1103/PhysRevLett.56.889).
- [104] M Kardar, G Parisi, and YC Zhang. Dynamic scaling of growing interfaces. *Physical Review Letters*, 56(9):889–892, 1986. URL [dx.doi.org/10.1103/PhysRevLett.56.889](https://doi.org/10.1103/PhysRevLett.56.889).
- [105] M Lässig. Quantized scaling of growing surfaces. *Physical Review Letters*, 80(11):2366–2369, 1998. URL [dx.doi.org/10.1103/PhysRevLett.80.2366](https://doi.org/10.1103/PhysRevLett.80.2366).
- [106] HC Fogedby. Localized growth modes, dynamic textures, and upper critical dimension for the Kardar-Parisi-Zhang Equation in the weak-noise limit. *Physical Review Letters*, 94(19):195702–195702, 2005. URL [dx.doi.org/10.1103/PhysRevLett.94.195702](https://doi.org/10.1103/PhysRevLett.94.195702).
- [107] VG Miranda and FDA Aarão Reis. Numerical study of the kardar-parisi-zhang equation. *Physical Review E*, 77(3):31134–31134, 2008. URL [dx.doi.org/10.1103/PhysRevE.77.031134](https://doi.org/10.1103/PhysRevE.77.031134).
- [108] AE Lita and JE Sanchez. Effects of grain growth on dynamic surface scaling during the deposition of al polycrystalline thin films. *Physical Review B*, 61

REFERENCES

- (11):7692–7699, 2000. URL [dx.doi.org/10.1103/PhysRevB.61.7692](https://doi.org/10.1103/PhysRevB.61.7692).
- [109] JM Lopez and J Schmittbuhl. Anomalous scaling of fracture surfaces. *Physical Review E*, 57(6):6405–6408, 1998. URL [dx.doi.org/10.1103/PhysRevE.57.6405](https://doi.org/10.1103/PhysRevE.57.6405).
- [110] JJ Ramasco, JM López, and MA Rodríguez. Generic dynamic scaling in kinetic roughening. *Physical Review Letters*, 84(10):2199–2202, 2000. URL [dx.doi.org/10.1103/PhysRevLett.84.2199](https://doi.org/10.1103/PhysRevLett.84.2199).
- [111] A Yanguas-Gil, J Cotrino, A Barranco, and AR González-Elipe. Influence of the angular distribution function of incident particles on the microstructure and anomalous scaling behavior of thin films. *Physical Review Letters*, 96(23):236101–236101, 2006. URL [dx.doi.org/10.1103/PhysRevLett.96.236101](https://doi.org/10.1103/PhysRevLett.96.236101).
- [112] T Fu and YG Shen. Surface growth and anomalous scaling of sputter-deposited al films. *Physica B: Condensed Matter*, 403(13-16):2306–2311, 2008. URL [dx.doi.org/10.1016/j.physb.2007.12.010](https://doi.org/10.1016/j.physb.2007.12.010).
- [113] CV Thompson. Structure evolution during processing of polycrystalline films. *Annual Reviews of Material Science*, 30(1):159–190, 2000. URL [dx.doi.org/10.1146/annurev.matsci.30.1.159](https://doi.org/10.1146/annurev.matsci.30.1.159).
- [114] YT Pei, KP Shaha, CQ Chen, R van der Hulst, AA Turkin, DI Vainshtein, and JTM De Hosson. Growth of nanocomposite films: From dynamic roughening to dynamic smoothening. *Acta Materialia*, 57(17):5156–5164, 2009. URL [dx.doi.org/10.1016/j.actamat.2009.07.017](https://doi.org/10.1016/j.actamat.2009.07.017).
- [115] T Karabacak, YP Zhao, GC Wang, and TM Lu. Growth-front roughening in amorphous silicon films by sputtering. *Physical Review B*, 64(8):85323–85323, 2001. URL [dx.doi.org/10.1103/PhysRevB.64.085323](https://doi.org/10.1103/PhysRevB.64.085323).
- [116] C Ophus, EJ Lubber, M Edelen, and et al. Simulations of faceted polycrystalline thin films: Asymptotic analysis. *Acta Materialia*, 57(14):4296–4303, 2009. URL [dx.doi.org/doi:10.1016/j.actamat.2008.11.014](https://doi.org/10.1016/j.actamat.2008.11.014).

REFERENCES

- [117] J Xu, T Shao, and G Jin. Effect of processing conditions on microstructure and electrical characteristics of Ni thin films. *Vac*, 84(4):478–482, 2009. URL [dx.doi.org/10.1016/j.vacuum.2009.10.012](https://doi.org/10.1016/j.vacuum.2009.10.012).
- [118] JJ Yang, B Liu, Y Wang, and KW Xu. Homologous temperature dependence of global surface scaling behaviors of polycrystalline copper films. *Applied Physics Letters*, 95:194104–194104, 2009. URL [dx.doi.org/10.1063/1.3263151](https://doi.org/10.1063/1.3263151).
- [119] T Smy, D Vick, MJ Brett, SK Dew, AT Wu, JC Sit, and KD Harris. Three-dimensional simulation of film microstructure produced by glancing angle deposition. *Journal of Vacuum Science & Technology A: Vacuum, Surfaces, and Films*, 18:2507, 2000. URL [dx.doi.org/10.1116/1.1286394](https://doi.org/10.1116/1.1286394).
- [120] SD Ekpe, LW Bezuidenhout, and SK Dew. Deposition rate model of magnetron sputtered particles. *Thin Solid Films*, 474(1-2):330 – 336, 2005. URL [dx.doi.org/10.1016/j.tsf.2004.09.007](https://doi.org/10.1016/j.tsf.2004.09.007).
- [121] GM Turner, SM Rossnagel, and JJ Cuomo. Directionality of sputtered Cu atoms in a hollow cathode enhanced planar magnetron. *Journal of Vacuum Science and Technology A: Vacuum, Surfaces, and Films*, 11(5):2796–2801, 1993. doi: [dx.doi.org/10.1116/1.578643](https://doi.org/10.1116/1.578643).
- [122] SJ Liu, EG Wang, CH Woo, and H Huang. Three-dimensional Schwoebel-Ehrlich barrier. *Journal of Computer-Aided Materials Design*, 7(3):195–201, 2001. URL [dx.doi.org/10.1023/A:1011832828818](https://doi.org/10.1023/A:1011832828818).
- [123] A Dollet, Y Casaux, G Chaix, and C Dupuy. Chemical vapour deposition of polycrystalline AlN films from AlC_{13} – NH_3 mixtures: II - analysis and modelling of transport phenomena. *Thin Solid Films*, 406(1-2):1–16, 2002. URL [dx.doi.org/10.1016/S0040-6090\(01\)01792-8](https://doi.org/10.1016/S0040-6090(01)01792-8).
- [124] A. Mahmood, R. Machorro, S. Muhl, J. Heiras, FF Castillon, MH Farias, and E. Andrade. Optical and surface analysis of DC-reactive sputtered AlN films. *Diamond & Related Materials*, 12(8):1315–1321, 2003. URL [dx.doi.org/10.1016/S0925-3407\(03\)00111-1](https://doi.org/10.1016/S0925-3407(03)00111-1).

REFERENCES

1016/S0925-9635(03)00076-1.

- [125] SS Hullavarad, RD Vispute, B Nagaraj, VN Kulkarni, S Dhar, T Venkatesan, KA Jones, M Derenge, T Zheleva, and MH Ervin. Advances in pulsed-laser-deposited ain thin films for high-temperature capping, device passivation, and piezoelectric-based rf mems/nems resonator applications. *Journal of Electronic Materials*, 35(4):777–794, 2006. URL [dx.doi.org/10.1007/s11664-006-0138-5](https://doi.org/10.1007/s11664-006-0138-5).
- [126] PR Willmott and JR Huber. Pulsed laser vaporization and deposition. *Reviews of Modern Physics*, 72(1):315–328, 2000. URL [dx.doi.org/10.1103/RevModPhys.72.315](https://doi.org/10.1103/RevModPhys.72.315).
- [127] C Ophus, EJ Lubber, and D Mitlin. Analytic description of competitive grain growth. *Physical Review E*, 81(1):11601, 2010. URL [dx.doi.org/10.1103/PhysRevE.81.011601](https://doi.org/10.1103/PhysRevE.81.011601).
- [128] DL Everitt, WJW Miller, NL Abbott, and XD Zhu. Evolution of a preferred orientation of polycrystalline grains in obliquely deposited gold films on an amorphous substrate. *Physical Review B*, 62(8):4833–4836, 2000. URL [dx.doi.org/10.1103/PhysRevB.62.R4833](https://doi.org/10.1103/PhysRevB.62.R4833).
- [129] MB Santos. On the distribution of the nearest neighbor. *American Journal of Physics*, 54(12):12, 1986. URL [dx.doi.org/10.1119/1.14731](https://doi.org/10.1119/1.14731).